

UNIVERSIDAD DE SONORA

DIVISIÓN DE CIENCIAS EXACTAS Y NATURALES

DEPARTAMENTO DE INVESTIGACIÓN EN FÍSICA

ADSORCIÓN DE MOLÉCULAS PEQUEÑAS SOBRE CÚMULOS
METÁLICOS SUBNANOMÉTRICOS, LIBRES Y EN SOPORTE

TESIS

Que para obtener el título de
DOCTOR EN CIENCIAS (FÍSICA)

Presenta

Luis Eduardo Gálvez González

Director

Dr. Lauro Oliver Paz Borbón

Co-director

Dr. Alvaro Posada Amarillas

Hermosillo, Sonora

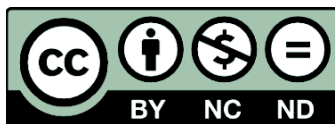
Abril 2022

Universidad de Sonora

Repositorio Institucional UNISON



**"El saber de mis hijos
hará mi grandeza"**



Excepto si se señala otra cosa, la licencia del ítem se describe como openAccess

Resumen

Los cúmulos de metales de transición han demostrado ser materiales novedosos, ofreciendo importantes ventajas sobre los catalizadores convencionales en numerosos procesos catalíticos, como la transformación de dióxido de carbono en metanol. En esta tesis, se ha llevado a cabo un estudio computacional de las propiedades físicas y químicas de cúmulos bimetalicos subnanométricos. El estudio se realizó mediante la combinación de cálculos de la Teoría del Funcionales de la Densidad (DFT) y del algoritmo de optimización global Basin-Hopping (BH). En particular, se analizaron tres tipos de cúmulos bimetalicos: Cu-Pt, Cu-Au y Re-Pt. También se investigó la adsorción de moléculas pequeñas, específicamente CO₂ y H₂, en cúmulos de Cu-Pt y Cu-Au en fase gaseosa. De este estudio se encontró que los cúmulos Cu-Pt bimetalicos son excelentes candidatos para las reacciones que involucran la activación de moléculas de H₂ o CO₂. Los cúmulos de Re-Pt se estudiaron tanto en fase gas como soportados en una superficie prístina de γ -Al₂O₃ (100), en tamaños desde los dos hasta seis átomos. El análisis de sus propiedades estructurales, energéticas y electrónicas reveló que los cúmulos bimetalicos de Re-Pt muestran una mayor estabilidad en comparación con los monometalicos de Re o Pt. Dado que los procesos catalíticos se producen a temperaturas elevadas, se estudió la fluxionalidad de los cúmulos de Re-Pt en fase gaseosa empleando la probabilidad de ocupación de sus isómeros. Los cúmulos de Re-Pt soportados en γ -Al₂O₃ mostraron tendencias estructurales similares a los en fase gaseosa y en acuerdo con resultados experimentales previos. Por último, motivado por el elevado costo computacional que supone realizar los cálculos para los cúmulos soportados, se exploró el uso de técnicas de aprendizaje automático o *machine learning* (ML). Para este fin, se empleó el método *symmetric Gradient-Domain Machine Learning* (sGDML) para estudiar los átomos de Pt y Pd soportados en un sustrato prístino de MgO (100). También utilizando sGDML, se calculó la difusividad de H en Pd en bulto en función de la temperatura y los valores obtenidos coinciden en gran medida con mediciones experimentales.

Palabras clave: cúmulos, optimización global, teoría de funcionales de la densidad, catálisis, adsorción, fluxionalidad, óxidos metálicos, alumina, *machine learning*

Abstract

Transition metal clusters have proven to be critical novel materials, offering major advantages over conventional catalysts in a range of value-added catalytic processes, such as carbon dioxide transformation to methanol. In this thesis, a computational study of the physical and chemical properties of subnanometer bimetallic transition metal clusters was carried out. The study was performed using the combination of Density Functional Theory (DFT) calculations and Basin-Hopping (BH) global optimization algorithms. In particular, three types of bimetallic clusters were analyzed: Cu-Pt, Cu-Au and Re-Pt. The adsorption mechanism of small molecules, namely CO₂ and H₂, on gas-phase Cu-Pt and Cu-Au tetramer clusters was also investigated, and it revealed the importance of considering the highly fluxional nature of transition metal clusters. From this study, it was found that bimetallic Cu-Pt clusters are excellent candidates for reactions which involve the activation of H₂ or CO₂ molecules. In the case of the Re-Pt clusters, they were studied both in the gas-phase and supported on the pristine γ -Al₂O₃ (100) surface, and in sizes ranging from two up to six atoms. The analysis of their structural, energetic and electronic properties revealed that bimetallic Re-Pt clusters show higher stability compared to monometallic Re or Pt clusters. As catalysis occurs at elevated temperatures, the fluxionality of Re-Pt gas-phase clusters was explored in terms of the isomer occupation probability. The γ -Al₂O₃-supported Re-Pt clusters displayed structural trends similar to their gas-phase counterparts and in great agreement with previous experimental findings. Finally, motivated by the high computational cost of performing calculations for supported clusters, the use of machine learning (ML) techniques was explored. The symmetric Gradient-Domain Machine Learning (sGDML) method was employed to study single Pt and Pd atoms supported on a MgO (100) pristine substrate. The diffusivity of H in bulk Pd as a function of the temperature was also calculated using sGDML and the obtained values were in excellent agreement with experimental measurements.

Keywords: clusters, global optimization, density functional theory, catalysis, adsorption, fluxionality, metal oxides, alumina, machine learning

Acknowledgements

First and foremost, I am deeply grateful to my supervisors, Dr. Lauro Oliver Paz Borbón and Prof. Alvaro Posada Amarillas, for their invaluable advice, continuous support, and patience during the past years.

I would like to thank CONACYT for awarding me the scholarship that allowed me to undertake my PhD studies. I would also like to acknowledge the cpu-time provided by Universidad de Sonora and Supercómputo UNAM (Miztli).

I would like to express my sincere gratitude to Prof. Klaus-Robert Müller, Prof. Alexandre Tkatchenko, Dr. Huziel E. Saucedo and Dr. Stefan Chmiela for giving me the opportunity to collaborate with them and for their hospitality during my stays in Berlin and Luxembourg. Part of this work could have not been possible without their help, guidance and fruitful discussions.

Finally, I would like to thank my parents for their relentless encouragement and untiring support.

Disclaimer

This thesis and the work described herein are entirely my own, except where I have acknowledged either help from a named person or a reference is given to a published source or a thesis. Text taken from another source will be enclosed in quotation marks and a reference will be given.

List of Publications

The results presented in this work were published in the following scientific articles:

- Paper 1 **CO₂ Adsorption on Gas-Phase Cu_{4-x}Pt_x (x=0–4) Clusters: a DFT Study**
L. E. Gálvez-González, J. O. Juárez-Sánchez, R. Pacheco-Contreras, I. L. Garzón, L. O. Paz-Borbón, and A. Posada-Amarillas
Physical Chemistry Chemical Physics **20**, 17071–17080 (2018)
- Paper 2 **H₂ Adsorption on Cu_{4-x}M_x (M = Au, Pt; x = 0–4) Clusters: Similarities and Differences As Predicted by Density Functional Theory**
L. E. Gálvez-González, J. A. Alonso, L. O. Paz-Borbón, and A. Posada-Amarillas
The Journal of Physical Chemistry C **123**, 30768–30780 (2019)
- Paper 3 **Structure, Energetics, and Thermal Behavior of Bimetallic Re-Pt Clusters**
L. E. Gálvez-González, A. Posada-Amarillas, and L. O. Paz-Borbón
The Journal of Physical Chemistry A **125**, 4294-4305 (2021)
- Paper 4 **BIGDML: Towards Exact Machine Learning Force Fields for Materials**
H. E. Saucedo, L. E. Gálvez-González, S. Chmiela, L. O. Paz-Borbón, KR. Müller, and A. Tkatchenko
Manuscript submitted for publication
- Paper 5 **DFT Study of Small Re-Pt Clusters Supported on γ -Al₂O₃**
L. E. Gálvez-González, A. Posada-Amarillas, and L. O. Paz-Borbón
Manuscript submitted for publication

Contents

1	Introduction	8
1.1	State of the art	9
1.2	Objectives and Goals	11
1.3	Structure	12
2	Theory	14
2.1	The Potential Energy Surface	14
2.2	Electronic Structure Calculations	16
2.2.1	The Many-Body Schrödinger Equation	16
2.2.2	The Density Functional Theory	18
2.2.3	The Hohenberg-Kohn Theorem	19
2.2.4	The Kohn-Sham Equations	19
2.2.5	Basis sets	21
2.2.6	Exchange and Correlation Functionals	22
2.2.7	Pseudopotentials	24
3	Methodology	26
3.1	Geometry Optimization	27
3.1.1	Local Optimization	27
3.1.2	Global Optimization	29
3.2	Energetic and Structural Analysis	32
3.2.1	Stability descriptors	32
3.2.2	Occupation probability	34
4	Adsorption of CO₂ and H₂ on Cu-Based Gas-Phase Clusters	36
4.1	Gas-Phase Cu _{4-x} Pt _x and Cu _{4-x} Au _x Clusters	37
4.2	Adsorption of H ₂ on Cu _{4-x} Pt _x and Cu _{4-x} Au _x Gas-Phase Clusters	40
4.3	Adsorption of CO ₂ on Gas-Phase Cu _{4-x} Pt _x Clusters	46

5	Gas-Phase and γ-Al₂O₃-Supported Re_nPt_m Clusters	51
5.1	Re _n Pt _m Gas-Phase Clusters	52
5.2	Re _n Pt _m Clusters Supported on γ -Al ₂ O ₃ (100)	62
6	Applications of Machine Learning to the Study of Adsorption Processes	70
7	Conclusions and outlook	77
A	Coordinates of the γ-Al₂O₃ unit cell	81
	Bibliography	82

Chapter 1

Introduction

The need to alleviate the effects of anthropogenic climate change has motivated the research and development of new and more efficient materials to capture and store atmospheric carbon dioxide (CO_2), which can be hydrogenated to produce useful compounds such as methanol (CH_3OH) and methane (CH_4) [1, 2]. One of the first steps in the development and production of renewable hydrocarbons from CO_2 is finding materials which are able to adsorb the molecules without hindering its capacity to react with other molecules required in the process, such as H_2 . However, molecular adsorption is a complex mechanism influenced by the nature of the adsorbent, the concentration of adsorbates on the adsorbent, and the temperature of the surrounding environment [3]. For this reason, a combined effort of experiments and theoretical studies is required to fully understand adsorption phenomena and design the best catalysts to convert CO_2 into renewable fuels.

Among the most common catalysts used in a wide range of industrial processes—including the hydrogenation of CO_2 —are those based on transition and noble metals such as platinum, gold or rhenium [4–12]. Given their scarcity and high cost, it is highly desirable to reduce the amount of material used without downgrading their catalytic performance. Another critical issue with conventional catalysts employed to transform CO_2 into value-added chemicals is the thermal and kinetic stability of this greenhouse molecule [13]. For these reasons, unconventional, novel, and more efficient catalysts need to be developed. A promising solution to these problems is the use of highly dispersed transition metal clusters supported on catalytically active metal oxides, such as $\gamma\text{-Al}_2\text{O}_3$, TiO_2 or CeO_2 . During the past years, these transition metal clusters have been the subject of intense experimental and computational research efforts due to their unique physical and chemical properties compared to their bulk counterparts[14–

18]. Furthermore, using bimetallic clusters can offer additional catalytic enhancement because of the synergy between the involved metal atoms[19–28]. Although small supported metal clusters offer better catalytic properties compared to larger nanoparticles or extended surfaces, their tendency to coalesce greatly reduces their reactivity over time [4]. Therefore, it remains a challenge to find combinations of supports and cluster compositions, sizes and morphologies that offer the best balance between stability and catalytic reactivity, activity and selectivity [29–33].

1.1 State of the art

Clusters are aggregates of atoms or molecules, whose sizes can range from only two up to 10^6 particles. Metal clusters are an important kind of clusters because they are employed in several catalytic processes. They can be classified as either monometallic, when the constituent metal atoms are all identical, or multimetallic, when they contain two or more chemical elements. Among the metal clusters, there are different varieties depending on the elements they are made of: s-block metal clusters, with delocalized and non-directional metallic bonding through the s orbitals; sp-metal clusters, whose covalent bonding involves both the s and p orbitals; and transition metal clusters, which have directional bonds involving the d orbitals and have a greater degree of covalency [34]. The experimental generation of clusters can be divided into four phases: vaporization, nucleation, growth and coalescence [34]. The first phase, vaporization, is the production of atoms in the gas phase. There are several ways to produce metal vapor: heat, pulsed-lasers, plasma, intense electrical discharges, bombardment with high energy ions, etc. The next step is the nucleation, or condensation of atoms to form cluster nuclei, followed by growth of those nuclei by the addition of more atoms. Finally, the formed clusters can coalesce to form larger clusters. Alternatively, metal clusters can also be synthesized by chemical methods [4, 35]. After the clusters have been generated, they can be characterized by a variety of experimental methods. The most appropriate techniques employed to characterize clusters will depend on their composition, electric charge, magnetic properties and whether they are in the gas-phase or supported on a surface. Gas-phase clusters can be studied by mass spectrometry, UV-visible and IR spectroscopy, electron spin resonance and other spectroscopic techniques. Measurements of surface-supported clusters are performed using common surface science techniques such as scanning tunneling microscopy (STM), scanning electron microscopy (SEM), transmission electron microscopy (TEM), atomic

force microscopy (AFM), X-ray diffraction (XRD), X-ray photoemission spectroscopy (XPS), etc [34].

Catalysts are substances which increase the rate of a chemical reaction when added to the reactants. They can be classified as either homogeneous, whose components are in the same phase as the reactant, or heterogeneous, where the phase of the components differs from that of the reactant. The components in heterogeneous catalysis are typically solid surfaces and reactants in the gas phase. A heterogeneous catalysis process usually consists of three phases: adsorption, reaction and desorption. Adsorption refers to the adhesion of atoms or molecules (the *adsorbates*) on a surface (the *adsorbent*). Adsorption phenomena can be classified into physisorption, when the particles adsorb via weak van der Waals forces, or chemisorption, when the adsorbates form covalent bonds with the surfaces. Moreover, in the case of molecules, chemisorption can be either non-dissociative when the adsorbate molecule remains intact after adsorption, or dissociative when the molecule breaks up with the resulting atoms bonding to the adsorbent surface. After the molecules have been adsorbed on the surface, chemical reactions can occur. The surface of a catalyst lowers the activation barrier to bond breaking and stabilizes reaction intermediates which eventually proceed to form reaction products. The activity of catalysts depends on the total catalyst surface area and this is the reason why smaller particles show greater reactivity. For bulk transition metals, chemical reactivity on their surfaces depends on the number and arrangement of the d electrons. However, for finite-size clusters, reactivity is also dependent on the number of atoms and their morphology. In structure sensitive reactions, the dependence of catalytic activity on particle size is more complex, with certain critical sizes being responsible for the catalysis process. Finding efficient bimetallic nanocatalysts requires a rigorous analysis of both its geometric and electronic structure to understand the interplay between the two metals and how they correlate with the observed physical properties and their chemical reactivity. Finally, after the reaction, the products must be desorbed from the surface. For this reason, in a good catalyst, the molecular adsorption must be strong enough to hold the reactants, but not too strong or else it would inhibit the desorption process.

Computational methods are very powerful tools that can help us predict and design better catalysts, as well as explain previously known, but not well-understood, phenomena related to catalysis. Together with experimental studies, computational catalysis can help us advance the development of more efficient catalysts with lower

production costs. Modern computational schemes have contributed extensively in the understanding of the effects of the interaction between clusters—both gas-phase and supported—with small adsorbates such as O₂, CO, CO₂, ethylene and ethanol for example [36–43]. Nevertheless, in order to simulate realistic catalytic processes it is required to mimic, as much as possible, the experimental conditions of the actual catalyst [44–47]. For instance, for a given chemical reaction it is necessary to investigate the binding mechanism between reactants and catalyst, considering the reciprocal effect of the adsorbed molecules on cluster structure, as well as the consequences of this interplay on the catalyst properties [48, 49].

In the case of clusters, previous studies have remarked the importance of extensively exploring their potential energy surface (PES) to determine the putative lowest-energy structures of these minuscule systems. This can be achieved by using global optimization techniques, often combined with electronic structure methods such as density functional theory (DFT). Density functional theory is one of the main workhorse methods for electronic structure calculations [50, 51]. The use of first principle calculations—as opposed to using classical or semi-empiric potentials—is especially important for small transition metal clusters composed of heavy elements such as platinum or gold. For these elements, the relativistic effects play a key role in determining the electronic and geometric structures of small clusters [52]. These relativistic effects, as well as other relevant phenomena such as dispersion forces or electron correlation effects, can be readily incorporated in modern computational electron structure calculations. Nonetheless, performing extensive *ab initio* explorations of the PES of bimetallic clusters supported on realistic catalytic surfaces—which can require simulation cells of hundreds of atoms—often demands enormous computational costs. In recent years, there has been intense research efforts aiming to develop Machine Learning (ML) methods to perform calculations with the same accuracy of *ab initio* calculations, but at a fraction of their computational cost [53–75]. However, simulating surface-supported clusters using ML still poses a considerable challenge due to their fluxional properties and the complex structure of the supports [17, 76, 77].

1.2 Objectives and Goals

The main objective of this thesis is to understand how the composition, morphology and the cluster-support interaction affect the adsorption properties of small molecules on transition metals clusters. These questions will be answered by assuming the hypothesis

that computational quantum chemistry tools can accurately predict the properties and model the interactions of molecules, metal clusters and metal oxide supports.

The specific goals of this work are to:

- Comprehend the basic concepts of the Density Functional Theory and learn how to apply it to solve specific problems.
- Use, modify and implement computational tools for the global exploration of potential energy surfaces using algorithms such as Basin Hopping Monte Carlo.
- Find the global minima and low-energy isomers for Cu_xPt_y ($x + y \leq 10$) metal clusters.
- Investigate the effect of the cluster-support interaction on the structure of Cu_xPt_y ($x + y \leq 10$) metal clusters.
- Obtain the optimal geometries of free and supported Cu_xPt_y ($x + y \leq 10$) metal clusters interacting with a CO_2 molecule.
- Calculate the activation and adsorption energies for each one of the cluster-molecule systems considered, as well as some reactivity and stability descriptors.
- Propose new Cu_xPt_y -based metal cluster structures for the conversion of CO_2 into methanol.
- To analyse the interactions between clusters and oxide substrates, the case of bimetallic Pt-Re clusters on $\gamma\text{-Al}_2\text{O}_3$.
- To explore machine-learning (ML) implementations to describe materials at the nanoscale.
- Motivate new experiments to characterize the interaction of CO_2 with metal clusters and compare the experimental results with the predictions obtained here.

1.3 Structure

This study was divided in three sections. The first section is based on the investigation of the adsorption mechanisms of CO_2 and H_2 on gas-phase copper-based bimetallic clusters. The main motivation for this study is understanding which characteristics—such

as composition, geometry or electronic properties—make the best clusters for molecular adsorption of CO₂ and H₂. Another purpose of this part is trying to explain the adsorption mechanisms of small molecules on bimetallic clusters, particularly on those composed of transition and noble metals.

The second section is based on the study of small bimetallic Re-Pt clusters, both in the gas-phase and supported on γ -Al₂O₃. In this part, a global optimization scheme was used to explore the PES of those clusters and find their low-lying isomers. Several structural and electronic properties of those clusters are analysed with the aim of finding their most stable structures. The effects of the temperature on the relative occupation probabilities of each isomer were calculated for the gas-phase clusters. In the case of γ -Al₂O₃-supported clusters, the binding mechanisms of the metal atoms with the surface are also explored.

In the final section, the application of machine learning techniques to the study of atoms supported on magnesium oxide (MgO) is presented. This study showcases the potential of using ML to accelerate computational catalysis by providing force fields with the accuracy of *ab initio* calculations, but at a fraction of the cost and with high re-usability. Although only supported single atoms are explored in this part, this is one of the first ML studies for complex materials and it is just the first step towards developing ML potentials for clusters supported on catalytic-relevant substrates such as metal oxides.

Chapter 2

Theory

2.1 The Potential Energy Surface

The potential energy surface (PES) of a collection of atoms defines the potential felt by their nuclei as a function of the positions of those atoms. Exploring the PES of a particular system can give us insight into the most stable geometries or the most favorable reaction pathways.

The PES characteristics depend on the level of theory employed to compute the interatomic potential. Different levels of theory can give rise to completely different PES. Figure 2.1 shows the difference between the PES of the Au₃ trimer as obtained with two different levels of theory. By using a semi-empirical potential, the predicted global minima of Au₃ is a perfect equilateral triangle. This potential also suggest the existence of a high energy isomer with a linear structure. In contrast, using DFT to calculate the PES of Au₃ suggest that the GM is a triangular cluster with an obtuse Au-Au-Au angle. At this level of theory, the equilateral triangle is a meta-stable isomer 0.11 eV higher in energy than the GM. In this case, the linear cluster is no longer a minima of the PES, but a transition state structure. The geometries predicted by DFT are in closer agreement with experiments [52] than those obtained by using semi-empirical potentials. These results illustrate the importance of choosing the correct level of theory for the study of clusters.

The most stable geometries of molecules, clusters and any material are those in which the forces acting upon their nuclei vanish. So in order to find those structures, we need a recipe to calculate the interatomic forces. We can compute those forces by solving the many-body Schrödinger equation for the nuclei (2.11) directly, but this is

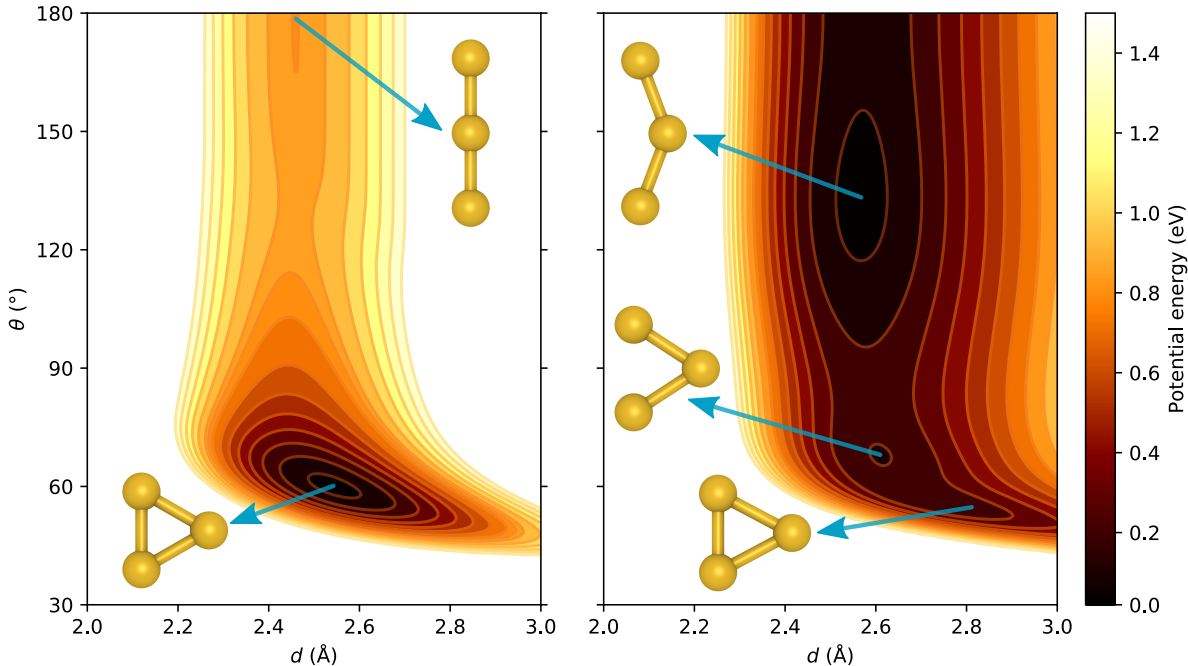


Figure 2.1: PES of a Au_3 cluster as calculated using: (a) a semi-empirical potential and (b) DFT.

computationally too expensive for most but the simplest molecules. Instead, we will approximate the nuclei as classical particles. This approximation for the nuclei is widely used to calculate the atomic forces and yields accurate results for most elements [50]. Defining the effective potential for the nuclei $U(\mathbf{R})$ as the sum of the electronic energy $E_e(\mathbf{R})$ and the electrostatic repulsion between nuclei,

$$U(\mathbf{R}) = \frac{e^2}{4\pi\epsilon_0} \sum_{I < J}^M \frac{Z_I Z_J}{|\mathbf{R}_I - \mathbf{R}_J|} + E_e(\mathbf{R}), \quad (2.1)$$

where e is the elementary charge, ϵ_0 is the vacuum permittivity, Z_I is the atomic number of nucleus I and \mathbf{R}_I are the coordinates of the same nucleus. The corresponding equation of motion for the I -th nucleus is

$$m_I \frac{d^2 \mathbf{R}_I}{dt^2} = \mathbf{F}_I, \quad (2.2)$$

where $\mathbf{F}_I = -\nabla_I U(\mathbf{R})$ is the force acting upon nucleus I . The force term corresponding to the electronic energy $E_e(\mathbf{R})$ can be calculated by taking advantage of the Hellmann-Feynman theorem. From this theorem, it can be shown that only the nuclei positions and the corresponding ground-state electron density are needed to compute the atomic forces [50, 78]. The effective potential thus defines the PES of the system which is being

studied.

2.2 Electronic Structure Calculations

Density functional theory (DFT) is one of the main workhorse tools in computational chemistry and materials science. It has been used extensively to predict the electronic, structural, vibrational, optical, magnetic and other properties of a wide variety of systems, from small organic molecules to complex extended materials. In the particular case of clusters, it has been successfully applied to the study of gas-phase clusters of diverse compositions including carbon, organic and inorganic compounds, and metals from all groups of the periodic table. It has also been employed to shed light on the interaction of clusters with metal oxide surfaces, 2D materials such as graphene, among other substrates. These previous studies have shown the wide applicability of DFT to the study of metal clusters.

2.2.1 The Many-Body Schrödinger Equation

For a system consisting of N electrons with coordinates $\mathbf{r}_1, \mathbf{r}_2, \dots, \mathbf{r}_N$ and M nuclei with coordinates $\mathbf{R}_1, \mathbf{R}_2, \dots, \mathbf{R}_M$, the corresponding Hamiltonian is

$$\hat{H} = \hat{T}_{\text{elec}} + \hat{T}_{\text{nuclei}} + \hat{V}(\mathbf{r}, \mathbf{R}). \quad (2.3)$$

The first two terms in the right-hand side of equation (2.3) are the respective kinetic energy operators for the electrons and nuclei:

$$\hat{T}_{\text{elec}} = - \sum_{i=1}^N \frac{\hbar^2}{2m_e} \nabla_i^2 \quad \text{and} \quad \hat{T}_{\text{nuclei}} = - \sum_{I=1}^M \frac{\hbar^2}{2m_I} \nabla_I^2, \quad (2.4)$$

where m_I is the rest mass of each nucleus I . The subscript i denotes derivatives respect to the electronic coordinates, while the I indicates derivatives respect to the nuclear coordinates. The operator $\hat{V}(\mathbf{r}, \mathbf{R})$ contains the Coulomb potentials corresponding to the repulsion between electrons, the repulsion between nuclei, and the attraction between electrons and nuclei:

$$\hat{V}(\mathbf{r}, \mathbf{R}) = \frac{e^2}{4\pi\epsilon_0} \left[\sum_{i<j}^N \frac{1}{|\mathbf{r}_i - \mathbf{r}_j|} + \sum_{I<J}^M \frac{Z_I Z_J}{|\mathbf{R}_I - \mathbf{R}_J|} - \sum_{i=1}^N \sum_{I=1}^M \frac{Z_I}{|\mathbf{r}_i - \mathbf{R}_I|} \right]. \quad (2.5)$$

Using Hartree atomic units allows us to simplify the notation and write more elegant equations. In these units, the masses are measured in units of the electron mass m_e , the distances in units of the average electron orbital radius a_0 of the H atom in its fundamental state, and the energies in units of the Coulomb energy for an electron-proton pair separated by a distance a_0 , E_{Ha} :

$$E_{\text{Ha}} = \frac{e^2}{4\pi\epsilon_0 a_0}, \quad (2.6)$$

where 'Ha' stands for Hartree. Using the Hartree atomic units, the many-body time-independent Schrödinger equation for the systems can be written as:

$$\left[-\sum_{i=1}^N \frac{1}{2} \nabla_i^2 - \sum_{I=1}^M \frac{1}{2m_I} \nabla_I^2 + \sum_{i<j}^N \frac{1}{|\mathbf{r}_i - \mathbf{r}_j|} + \sum_{I<J}^M \frac{Z_I Z_J}{|\mathbf{R}_I - \mathbf{R}_J|} - \sum_{i=1}^N \sum_{I=1}^M \frac{Z_I}{|\mathbf{r}_i - \mathbf{R}_I|} \right] \Psi = E_{\text{tot}} \Psi. \quad (2.7)$$

For all but the simplest systems, solving equation (2.7) directly poses a problem so complex that it exceeds the modern computational power [50]. Thus, some approximations must be done to get solutions in a reasonable time. Given that nuclei are much heavier than electrons, with the mass of a proton alone being 1836 times the electron mass, we can assume that the motion of nuclei and electrons in molecules can be decoupled. This is known as the Born-Oppenheimer or adiabatic approximation [50, 79]. Under this approximation, the total wavefunction Ψ can be expressed as the product of an electronic wavefunction and a nuclear wavefunction,

$$\Psi(\mathbf{r}, \mathbf{R}) = \psi_{\mathbf{R}}(\mathbf{r}; \mathbf{R}) \phi(\mathbf{R}), \quad (2.8)$$

where $\psi_{\mathbf{R}}(\mathbf{r}; \mathbf{R})$ is the electronic wavefunction with the nuclei positions as parameters, and $\phi(\mathbf{R})$ is the nuclear wavefunction. This decoupling of the electronic and nuclear wavefunctions allows us to separate equation (2.7) into two equations, one for the electrons and one for the nuclei. To achieve this, we substitute (2.8) into (2.7) and divide by $\psi_{\mathbf{R}}(\mathbf{r}; \mathbf{R}) \phi(\mathbf{R})$,

$$\begin{aligned} & -\frac{1}{\psi_{\mathbf{R}}(\mathbf{r}; \mathbf{R})} \sum_{i=1}^N \frac{1}{2} \nabla_i^2 \psi_{\mathbf{R}}(\mathbf{r}; \mathbf{R}) + \sum_{i<j}^N \frac{1}{|\mathbf{r}_i - \mathbf{r}_j|} - \sum_{i=1}^N \sum_{I=1}^M \frac{Z_I}{|\mathbf{r}_i - \mathbf{R}_I|} \\ & - \frac{1}{\phi(\mathbf{R})} \sum_{I=1}^M \frac{1}{2m_I} \nabla_I^2 \phi(\mathbf{R}) + \sum_{I<J}^M \frac{Z_I Z_J}{|\mathbf{R}_I - \mathbf{R}_J|} - E_{\text{tot}} = 0, \end{aligned} \quad (2.9)$$

where we have neglected derivatives of the electronic wavefunction with respect to nuclear coordinates, and derivatives of the nuclear wavefunction with respect to electronic coordinates. Applying separation of variables leads to a pair of equations, one of them describing the electronic states,

$$\left[-\sum_{i=1}^N \frac{1}{2} \nabla_i^2 + \sum_{i<j}^N \frac{1}{|\mathbf{r}_i - \mathbf{r}_j|} - \sum_{i=1}^N \sum_{I=1}^M \frac{Z_I}{|\mathbf{r}_i - \mathbf{R}_I|} \right] \psi_{\mathbf{R}}(\mathbf{r}; \mathbf{R}) = E_e(\mathbf{R}) \psi_{\mathbf{R}}(\mathbf{r}; \mathbf{R}), \quad (2.10)$$

and another one describing the nuclear states,

$$\left[-\sum_{I=1}^M \frac{1}{2m_I} \nabla_I^2 + \sum_{I<J}^M \frac{Z_I Z_J}{|\mathbf{R}_I - \mathbf{R}_J|} + E_e(\mathbf{R}) \right] \chi(\mathbf{R}) = E_{\text{tot}} \chi(\mathbf{R}). \quad (2.11)$$

The term $E_e(\mathbf{R})$ is the electronic energy as a function of the nuclear coordinates. Although decoupling the many-body Schrödinger equation has simplified the problem significantly, the solutions for the equations (2.10) and (2.11) remain too complex for most systems. Therefore, we will focus on solving the electron-only equation (2.10) under the framework of the density functional theory (DFT).

2.2.2 The Density Functional Theory

The central variable of the DFT method is the electron density $n(\mathbf{r})$, which gives us the probability of finding any electron at position \mathbf{r} , while the other electrons have arbitrary positions [50, 80]. The use of $n(\mathbf{r})$ to describe our N -electron system instead of the electronic wavefunction $\psi_{\mathbf{R}}$ reduces the number of coordinates involved from $3N$ to only three. To obtain the expression for the electron density, we must first consider the probability of finding an electron i at \mathbf{r} , when the rest of the electrons can be anywhere, which is given by:

$$P(\mathbf{r}_i = \mathbf{r}) = \int \cdots \int |\psi_{\mathbf{R}}|^2 \prod_{j \neq i}^N d\mathbf{r}_j, \quad (2.12)$$

where $\psi_{\mathbf{R}}$ is a function of all the electron coordinates with the nuclei positions as parameters, and the integral is over all the coordinates, except \mathbf{r}_j . Therefore, the

electron density $n(\mathbf{r})$ is the sum of the probabilities $P(\mathbf{r}_i = \mathbf{r})$ for all N electrons, i.e.

$$\begin{aligned} n(\mathbf{r}) &= \sum_i^N P(\mathbf{r}_i = \mathbf{r}) \\ &= N \int |\psi_{\mathbf{R}}|^2 d\mathbf{r}_2 \cdots d\mathbf{r}_N. \end{aligned} \quad (2.13)$$

From (2.13) it can be seen that integrating the electron density yields the total number of electrons N .

2.2.3 The Hohenberg-Kohn Theorem

Hohenberg and Kohn built the foundations of DFT by applying the variational principle to the study of the homogeneous gas of interacting electrons [80, 81]. They demonstrated that the many-body ground-state energy is a unique functional of the electron density. To prove this theorem, let us consider a system of N electrons in an external potential $V_n(\mathbf{r})$. It can be shown by a *reductio ad absurdum* that two different external potentials cannot lead to the same ground-state electron density. Therefore, V_n is uniquely determined by the electron density. Furthermore, the external potential defines the wavefunction of the system, which in turn determines the total energy. Hence, the total ground-state energy of the system is uniquely determined by $n(\mathbf{r})$, i.e.

$$E = F[n(\mathbf{r})], \quad (2.14)$$

where $F[n(\mathbf{r})]$ is a universal functional. For all the allowed electron densities, the energy functional reaches its minimum only for the ground-state electron density $n_0(\mathbf{r})$ [50, 80, 81], which can be expressed as:

$$\left. \frac{\delta F}{\delta n} \right|_{n_0} = 0, \quad (2.15)$$

where the δ denotes the functional derivative.

2.2.4 The Kohn-Sham Equations

While the Hohenberg-Kohn theorem establishes a strong theoretical foundation to study many-electron systems, it does not provide a way to compute the aforementioned functional. Kohn and Sham proposed to approximate the real system of interacting electrons with a fictitious system of *non-interacting* electrons with electron density $n(\mathbf{r})$, moving

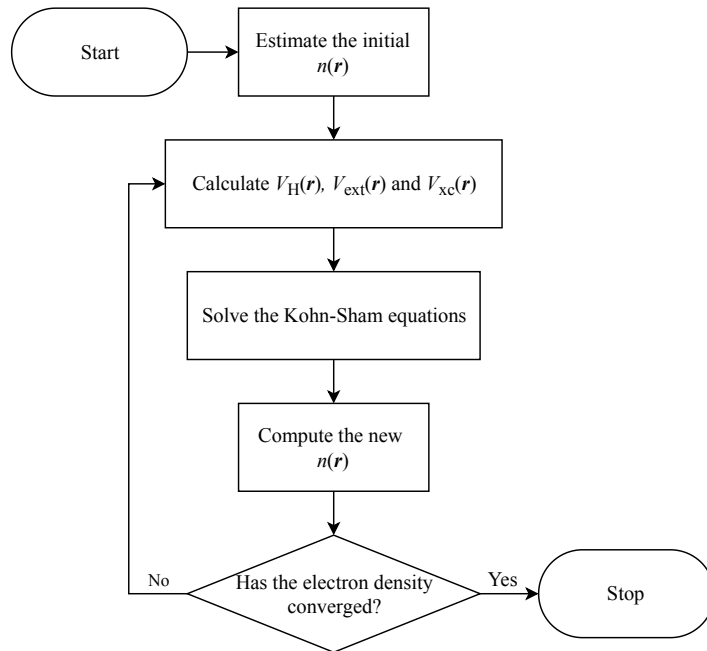


Figure 2.2: Flowchart for the self-consistent solution to the Kohn-Sham equations.

in a effective potential [80, 82]. Under this scheme, the energy functional is broken down in the form

$$E[n(\mathbf{r})] = \int V_{ext}(\mathbf{r})n(\mathbf{r})d\mathbf{r} + \frac{1}{2} \int \frac{n(\mathbf{r})n(\mathbf{r}')}{|\mathbf{r} - \mathbf{r}'|} d\mathbf{r}d\mathbf{r}' + T_s[n(\mathbf{r})] + E_{xc}[n(\mathbf{r})]. \quad (2.16)$$

The first term in the right-hand side of equation (2.16) corresponds to the external potential and the second term is the classical Coulomb energy. $T_s[n(\mathbf{r})]$ is the kinetic energy of the fictitious system, and $E_{xc}[n(\mathbf{r})]$ contains the exchange and correlation energy of the real system.

For the fictitious system of non-interacting electrons, we can express the electron density as the sum of the individual probabilities of finding each electron at position \mathbf{r} ,

$$n(\mathbf{r}) = \sum_{i=1}^N |\phi_i(\mathbf{r})|^2, \quad (2.17)$$

where $\phi_i(\mathbf{r})$ are the Kohn-Sham wavefunctions of each electron. Applying the Hohenberg-Kohn variational principle (2.15), subject to the orthonormality constraints of the wavefunctions $\phi_i(\mathbf{r})$, leads to the system of N one-electron Schrödinger equations known as

the Kohn-Sham equations

$$\left[-\frac{1}{2}\nabla^2 + V_{ext}(\mathbf{r}) + V_H(\mathbf{r}) + V_{xc}(\mathbf{r}) \right] \phi_i(\mathbf{r}) = \epsilon_i \phi_i(\mathbf{r}), \quad (2.18)$$

where $V_H(\mathbf{r})$ is the Hartree potential [50, 80], given by:

$$V_H(\mathbf{r}) = \int \frac{n(\mathbf{r}')}{|\mathbf{r} - \mathbf{r}'|} d\mathbf{r}', \quad (2.19)$$

and $V_{xc}(\mathbf{r})$ is the exchange and correlation (xc) potential,

$$V_{xc}(\mathbf{r}) = \frac{\delta E_{xc}}{\delta n}. \quad (2.20)$$

The potentials $V_H(\mathbf{r})$ and $V_{xc}(\mathbf{r})$ both depend on the electron density, which in turn is a function of the Kohn-Sham orbitals $\phi_i(\mathbf{r})$. However, to calculate $\phi_i(\mathbf{r})$ we must solve the equations 2.18, which are subject to $V_H(\mathbf{r})$ and $V_{xc}(\mathbf{r})$. To overcome this problem, the Kohn-Sham equations are computationally solved in a iterative *self-consistent field* loop (SCF) as shown in Figure 2.2.

2.2.5 Basis sets

In practice, the Kohn-Sham orbitals $\phi_i(\mathbf{r})$ are usually expressed in terms of basis sets. Two of the main formulations used are the linear combination of atomic orbitals (LCAO) and the plane-wave expansion. In the LCAO approach, the Kohn-Sham orbitals are expressed as combinations of orbitals $\chi_j(\mathbf{r})$ centered at the atomic nuclei:

$$\phi_i(\mathbf{r}) = \sum_j c_{ij} \chi_j(\mathbf{r}). \quad (2.21)$$

The basis functions $\chi_j(\mathbf{r})$ are commonly modelled using analytical functions such as Gaussian-type orbitals (GTO) or Slater-type orbitals (STO), or by numerical functions. Each representation has its advantages and disadvantages. Since STOs are solutions to the Schrödinger equation for hydrogen-like atoms, they provide a more accurate representation of the atomic orbitals near the nucleus. Meanwhile, GTOs offer a computational advantage as the product of two different GTOs is a linear combination of GTOs centered on a point along the axis connecting the centers of the former. Gaussian-type orbitals can also be used to approximate Slater-type orbitals. The resulting basis set are denoted by STO- n G, where n is the number of GTOs used to represent each STO. Considering that valence electrons are largely responsible for the molecular bonding, it

is common to represent valence orbitals by using two or more basis functions. Basis sets which incorporate this feature are called double- ζ , triple- ζ , and so on, depending on the number of basis functions used for the valence orbitals.

Another method commonly used to represent the Kohn-Sham orbitals is by using plane-waves (PWs). This approach arises from the Bloch's theorem which states that the wavefunctions of a system in a periodic potential can be expressed as

$$\phi_i(\mathbf{r}) = e^{i\mathbf{k}\cdot\mathbf{r}}u_i(\mathbf{r}), \quad (2.22)$$

where $u_i(\mathbf{r})$ is a periodic function with the same periodicity as the cell and k is the wave vector. We can express $u_i(\mathbf{r})$ in terms of plane-waves where the reciprocal lattice vectors \mathbf{G} are the wave vectors. These vectors \mathbf{G} are subject to the periodicity constraint $\mathbf{G}\cdot\mathbf{R} = 2\pi n$, where \mathbf{R} are the real space lattice vectors and n is an integer. As a result, the Kohn-Sham orbitals can be expanded into an infinite sum of plane-waves as

$$\phi_i(\mathbf{r}) = \frac{1}{\Omega} \sum_{\mathbf{G}} \tilde{u}_i(\mathbf{k} + \mathbf{G})e^{i(\mathbf{k}+\mathbf{G})\cdot\mathbf{r}}, \quad (2.23)$$

where Ω is the volume of the periodic cell. In practice, only a reduced set of plan-waves is used by choosing an appropriate cut-off energy value. One of the main advantages of using PWs is that they are—unlike LCAO—-independent of the positions of the atoms. Their periodicity makes them ideal for extended, periodic systems such as clusters supported on metal oxides. Nonetheless, they are also suitable for isolated systems if the cell used is large enough to minimize the interaction between periodic images.

2.2.6 Exchange and Correlation Functionals

In the Kohn-Sham scheme, the exchange and correlation functional is unknown and must be approximated [50, 80, 82]. Over the past decades, numerous approaches have been implemented to obtain a good approximation for the exchange and correlation functionals. The simplest of them is the local density approximation (LDA) [50, 80, 83] and can be expressed as:

$$E_{xc}^{LDA}[n(\mathbf{r})] = \int n(\mathbf{r})\epsilon_{xc}^{unif}(n(\mathbf{r}))d\mathbf{r}, \quad (2.24)$$

where $\epsilon_{xc}^{unif}[n(\mathbf{r})]$ is the exchange-correlation energy per particle of an homogeneous electron gas with density $n(\mathbf{r})$ at point r . In this case, the exchange-correlation energy is approximated at each point as that of a homogeneous electron gas with the same electron density of the real system at that point [83]. This approximation can be generalized to include the electron spin, which is known as the local spin density approximation (LSD), and is given by:

$$E_{xc}^{LSD}[n_{\uparrow}, n_{\downarrow}] = \int n(\mathbf{r})\epsilon_{xc}^{unif}(n_{\uparrow}, n_{\downarrow})d\mathbf{r}. \quad (2.25)$$

Further approximations incorporate contributions not only from the electron density, but also from its gradient or its Laplacian [83]. When they include the gradient of the electron density, they are known as generalized gradient approximations (GGA) [83], whose functional form is

$$E_{xc}^{GGA}[n_{\uparrow}, n_{\downarrow}] = \int n(\mathbf{r})f(n_{\uparrow}, n_{\downarrow}, \nabla n_{\uparrow}, \nabla n_{\downarrow})d\mathbf{r}, \quad (2.26)$$

where f is a parametrized function of the electron density and its gradient. Exchange-correlation approximations that incorporate the Laplacian of the electron density or the kinetic energy are called meta-generalized gradient approximations (meta-GGA) [83].

So far, the approximations we have discussed have been local, since they depend only on the local properties of the electronic density. When they include a percentage of non-local Hartree-Fock exchange energy, they are called hybrid functionals [83]. Both local functionals and hybrid functionals have advantages and disadvantages. Since exact functionals must be non-local, the accuracy of local functionals may be lower than that of hybrid functionals for some systems, but local density functionals model transition metal bonds and vibrational frequencies more accurately [84] and have a lower computational cost. Hybrid functionals can improve the accuracy of the calculations, but they demand more computational resources.

In particular, the Perdew-Burke-Ernzerhof (PBE) GGA exchange-correlation functional was chosen for all the calculations done in this work. The PBE-GGA functional is parametrized using only fundamental constants, with no empirical parameters involved [85]. This widely used functional has been shown to produce reliable results for transition metals [86–90]. Given the PBE functional affordability in terms of computational cost—the number of homotops in a bimetallic cluster containing a number of N_A

and N_B metal atoms increases as $(N_A + N_B)! / N_A! N_B!$ —it allows us to thoroughly explore the PES of gas-phase and supported bimetallic clusters with confidence.

Although DFT is accurate enough to provide acceptable predictions for structural and cohesive properties of materials, it fails when it comes to predicting the electronic bandgaps of semiconductors. A variety of approaches have been developed to overcome this critical issue. One of these methods is the use of hybrid functionals, which can reach relatively high accuracy at the expense of a much higher computational cost. Another commonly used approach is the DFT+U correction, whose computational cost is not much higher than that of normal DFT computations. The DFT+U method adds a Hubbard correction (U) to the functional which accounts for the on-site Coulomb interaction of localized electrons [91, 92]. The value of U can be derived from first principle calculations, but in practice it is usually fitted to experimental data [93]. The use of DFT+U can be relevant when dealing with reducible metal oxides with narrow bandgaps such as TiO_2 or CeO_2 , which behave as semiconductors. In contrast, it might not be necessary to include any correction if the calculations only involve non-reducible metal oxides with large bandgaps like MgO or Al_2O_3 [93].

Another shortcoming of common local and hybrid GGA functionals is that they do not account for the long-range electron correlations responsible for the van der Waals (vdW) dispersive forces. These vdW interactions—together with electrostatic and exchange-repulsion interactions—affect the configuration and orientation of molecules on surfaces and thus cannot be ignored when studying molecular adsorption processes. Commonly used implementations which incorporate the vdW dispersion corrections into the Kohn-Sham DFT formalism are those developed by Grimme (DFT-D) [94, 95], and Tkatchenko and Scheffler (TS) [96]. In this work, functionals derived from DFT-D were employed to analyze the interaction of H_2 and CO_2 with Cu-based clusters.

2.2.7 Pseudopotentials

Core electrons do not contribute directly to the bonding mechanisms between atoms. Pseudopotentials replace the all-electron potentials with effective potentials which replicate the screening effects of the core electrons. It can be seen from Figure 2.3 how the all-electron wavefunction and its pseudo-wavefunction are nearly identical above a given cutoff radius r_c , even though they differ appreciably below r_c . Using pseudopotentials—

and thus reducing the electrons involved to the valence electrons only—can significantly decrease the computational cost of electronic structure calculations. This reduction is particularly important when used together with plane-wave basis sets. The rapid oscillations of the wavefunctions in the core region would require impractically high energy cutoff values. Pseudopotentials can also be used with LCAO basis sets, in this case they are also referred to as effective core potentials. While LCAO basis functions can easily reproduce the rapid oscillations in the core regions, the use of effective potentials can reduce the computational cost compared the all-electron calculations. Another advantage of pseudopotentials is that they can readily incorporate relativistic effects which are crucial for heavy elements.

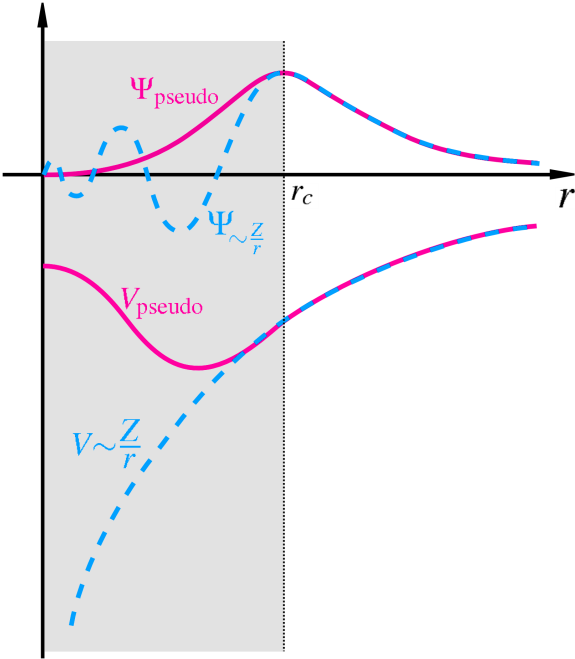


Figure 2.3: Schematic comparison of an all-electron potential and its wavefunction (dashed lines) with their corresponding pseudopotential and pseudo-wavefunction (solid lines).

Chapter 3

Methodology

The study of the adsorption of molecules on metal clusters in this study was performed via a combination of DFT calculations and global optimization algorithms. The main steps followed to achieve this task are described in Figure 3.1. The first step was the exhaustive global exploration of the PES of the clusters considered, using DFT to calculate the potential energy and the interatomic forces. The next step was to place the molecules around the global minima clusters of each composition on every non-equivalent adsorption site. Then the combined cluster and molecule systems were locally relaxed at the DFT level. Finally, the properties of the lowest-energy structures found were analysed using a variety of structural and energetic descriptors.

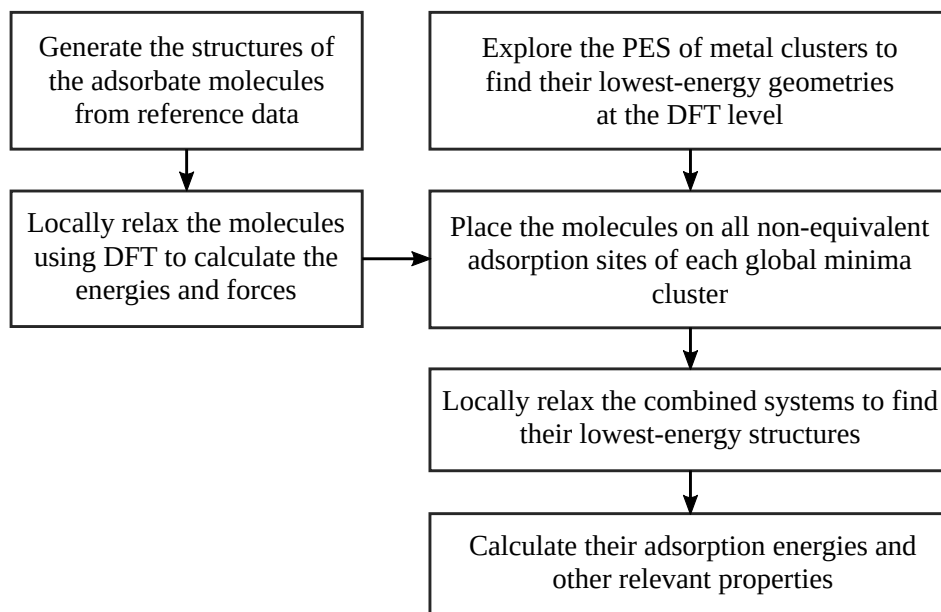


Figure 3.1: Flowchart for the procedure followed in this work to study the adsorption of molecules on metal clusters.

3.1 Geometry Optimization

3.1.1 Local Optimization

Finding the minima of the PES requires the use of optimization algorithms where $U(\mathbf{R})$ is the objective function. These algorithms can be broadly classified as *local* or *global*. Local optimization algorithms are used to find the local or relative minima of a function in a limited range. A brief summary of the most common algorithms will be provided here. A more detailed description can be found in the literature [97]. The simplest among these algorithms is known as steepest descent or gradient descent, where the function is iteratively minimized by taking steps in the opposite direction of its gradient. In our particular problem, the negative gradient of the potential energy is equal to the force. While this algorithm is very simple to implement, it might converge slowly to the minima and require a large number of steps. This can be an inconvenience since the Kohn-Sham equations must be solved at every step to compute the forces. Hence, we will need more efficient algorithms to solve our optimization problem. Among the algorithms commonly used for structure optimization are: quasi-Newton methods such as the limited-memory Broyden-Fletcher-Goldfarb-Shanno (L-BFGS) [98]; those based on molecular dynamics such as the Quick-Min Verlet method (QM) [97], the damped-Verlet method [50], or the fast inertial relaxation engine (FIRE) method [99]; the conjugate gradients (CG) [100]; and the Berny algorithm [101].

The software packages—Gaussian 09 [102] and Quantum Espresso [103, 104]—used in this work to perform DFT calculations employ different local optimization algorithms. By default, Gaussian 09 uses the Berny algorithm, while optimizations in Quantum Espresso can be done using either the BFGS or the QM Verlet algorithms. An example of a minimal input file used to locally relax a Pt₄ cluster in Gaussian 09 is given below:

```
% nprocshared=8
# pbepbe/sdd scf=(maxcycle=150) opt=(maxcycle=100)
```

Local minimization example of a Pt₄ cluster

```
0 1 ! Charge (0) and spin multiplicity (1)
Pt   2.00   0.00   0.00
Pt  -2.00   0.00   0.00
Pt   0.00   1.25   0.00
Pt   0.00  -1.25   0.00
```

In the previous example, the calculations will be performed using the PBE functional with the Stuttgart/Dresden triple- ζ LCAO basis set with relativistic effective core potentials (SDD) [105]. The `maxcycle` keyword specifies the maximum number of either self-consistent cycles (for `scf`) or optimization steps (for `opt`). The numbers before the coordinates indicate that the cluster is neutral and is in a singlet state. The positions of the atoms are given in cartesian coordinates, in Å. The equivalent input file used to relax the same cluster in Quantum Espresso is as follows:

```
&control
  calculation= 'relax', ! Local optimization
  pseudo_dir = '/path/to/pseudopotential/files/',
  title = 'Local minimization example of a Pt4 cluster.',
/

&system
 ibrav= 1, ! Calculations will be performed in a cubic cell
  A = 10.0, ! Lattice parameter of the cubic cell
  nat = 4, ! Total number of atoms
  ntyp = 1, ! Number of distinct elements involved
  ecutwfc = 40.0, ! Kinetic energy cutoff (in Ry) for wavefunctions
  ecutrho = 400.0, ! Kinetic energy cutoff (in Ry) for charge density
  nspin = 2, ! The calculations will be spin-polarized
  total_magnetization = 0, ! Total spin
/

&electrons
  conv_thr = 1.0d-6, ! Convergence threshold for DFT self-consistent cycles
/

&ions
  ion_dynamics = 'bfgs', ! The BFGS algorithm will be used to optimize
/

ATOMIC_SPECIES
Pt 195.84 Pd.pbe-n-rrkjus_psl.1.0.0.UPF ! Element Atomic_mass Pseudopotential
```

```
K_POINTS {gamma}
```

```
ATOMIC_POSITIONS {angstrom}
```

```
Pt    2.00    0.00    0.00  
Pt   -2.00    0.00    0.00  
Pt    0.00    1.25    0.00  
Pt    0.00   -1.25    0.00
```

Since Quantum Espresso uses PW basis-sets, we must place the cluster in a simulation cell large enough to minimize the interaction between its periodic images. In this case, the cell is a cube of side 10.0 Å. In contrast to Gaussian, in Quantum Espresso the spin state is specified by setting the total spin (S) and not the multiplicity ($2S+1$). The calculations can also be spin-unrestricted if we use the keyword `starting_magnetization` instead of `total_magnetization`. By doing so, Quantum Espresso will try to find the optimal magnetization value which minimizes the electronic energy. The optimization steps will be performed using the BFGS algorithm with default convergence criteria (1.0×10^{-3} a.u. for the forces, and 1.0×10^{-4} a.u. for the energy). In this example, a scalar relativistic ultra-soft pseudopotential for Pt will be used. By setting `K_POINTS` the reciprocal space will be sampled at the Γ point only, an appropriate choice for isolated systems such as gas-phase clusters or molecules.

3.1.2 Global Optimization

Global optimization refers to the problem of finding the absolute minimum or maximum of a function in a given search space. In computational chemistry and materials science, global optimization is used to find the most stable structures, which correspond to the global minima of their PES. Numerous global optimization methods have been developed for the particular case of atomic clusters, such as simulated annealing (SA) [106], Basin Hopping (BH) [79, 107], genetic algorithms (GA) [108], particle swarm optimization (PSO) [109], etc. Genetic algorithms are part of a class of optimization techniques inspired by the principles of natural evolution, known as evolutionary algorithms. In the GA, an initial population of individuals—a set of different structures in the case of clusters—evolves for a number of generations until the convergence criterion is reached. The evolution of the population is achieved by using evolutionary operators including mating, mutation and natural selection [108]. Particle swarm optimization algorithms (PSO) are based on the behaviour of swarms. In this case, a population of candidate

solutions (called particles) move in the search space guided by their best known local solutions, but also by the best solution known by the whole population [109]. In the Monte Carlo basin-hopping method, the PES is transformed into a set of staircases with plateaus corresponding to the energy minima of the system. This transformation is achieved by assigning the energy of the local minimum to every geometry that leads to that particular minimum after a local optimization. The transformed PES ($\tilde{E}(\mathbf{R})$) is then given by:

$$\tilde{E}(\mathbf{R}) = \min[E(\mathbf{R})], \quad (3.1)$$

where \min indicates that a local optimization is performed starting from \mathbf{R} . Figure 3.2 schematically represents this transformation for a one-dimensional PES.

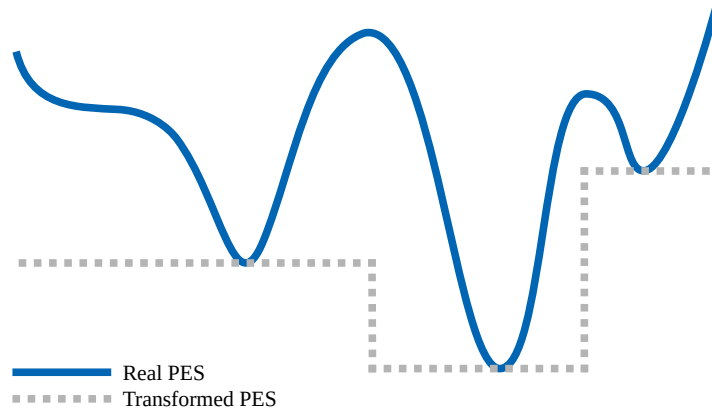


Figure 3.2: Transformation of a one-dimensional PES into a set of staircases by using the Basin Hopping algorithm.

The Monte Carlo BH algorithm is outlined in Figure 3.3. The first step is generating an initial random configuration, which is relaxed using a local optimization algorithm to get a first minimum with energy E_{old} . This minimum structure is perturbed by randomly displacing its atoms, and the new configuration is then relaxed to find a new minimum with energy E_{new} . The random displacement of the atoms is called the *shake* or *kick* move. The new minimum is accepted if its energy difference with respect to the old minimum $\Delta E = E_{\text{new}} - E_{\text{old}}$ satisfies the Metropolis criterion, i.e. if $\Delta E < 0$ or if $\exp(-\Delta E/kT) > R$ where $0 \leq R \leq 1$ is a random number. The process is then repeated using the new minimum as the starting configuration. For clusters composed of two or more elements, the coordinates of two atoms of different elements can also be swapped. This step is called *exchange* or *swap* move.

Compared to the GA or PSO methods, the BH algorithm only requires a single

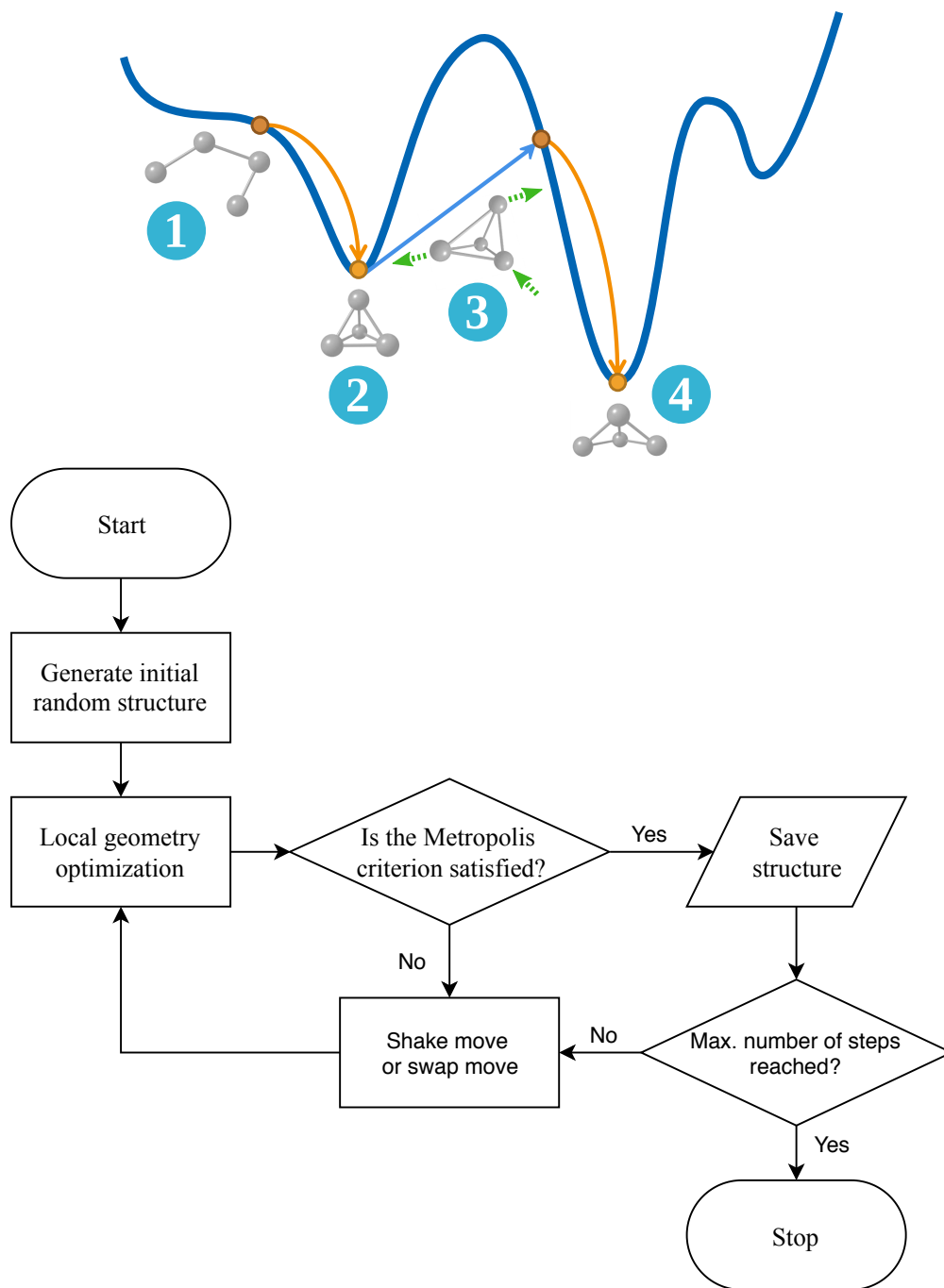


Figure 3.3: (Top) Schematic illustration of the Basin Hopping algorithm steps: (1) initial random structure, (2) local optimization of the initial structure, (3) *shake* move and (4) local optimization of the perturbed structure. (Bottom) Basin Hopping global optimization algorithm flowchart.

initial structure, not a whole initial population of them. While generating a population of small gas-phase cluster structures is computationally feasible, the same cannot be said for clusters supported on substrates composed of tens or hundreds of atoms. For

this reason, BH was the method of choice to explore the PES of both gas-phase and supported metal clusters in this work.

Two different BH-DFT software were employed in the present work: one developed by the group of Posada-Amarillas [110], coupled to Gaussian 09; the other one by Paz-Borbón *et al* which uses Quantum Espresso as the DFT calculator [111]. The latter is freely available at <https://github.com/NanoCatalysis/Basin-Hopping>. The key difference between these two implementations is that using Quantum Espresso—which employes PW basis sets—allows us to explore the PES of both supported clusters as well as those in the gas-phase.

3.2 Energetic and Structural Analysis

3.2.1 Stability descriptors

Numerous descriptors can be used to analyze the stability of metal clusters, such as the binding energy E_b , the mixing energy Δ , the second difference in energy Δ_2 , or the second difference in atom-evaporation energy Δ_2^v [112].

The average binding energy per atom E_b compares the total energy of the cluster with the energy of its individual atoms. For a bimetallic cluster composed of elements A and B, E_b is given by:

$$E_b(A_nB_m) = -\frac{E_{\text{tot}}(A_nB_m) - nE_{\text{tot}}(A) - mE_{\text{tot}}(B)}{N}, \quad (3.2)$$

where $N = m + n$ is the total number of atoms. To examine the relative stability of monometallic clusters, the second difference in energy Δ_2 and the stability function Δ_2^v were used. The former is given by:

$$\Delta_2(N) = E_{\text{tot}}(N-1) + E_{\text{tot}}(N+1) - 2E_{\text{tot}}(N), \quad (3.3)$$

where $E_{\text{tot}}(N)$ is the total energy of the monometallic clusters of size N . The function Δ_2^v is expressed as:

$$\Delta_2^v(N) = 2E_v(N) - E_v(N+1) - E_v(N-1) = \Delta_2(N) - \Delta_2(N-1), \quad (3.4)$$

where $E_v(N)$ is the atom-evaporation energy of the cluster of size N . This stability descriptor was proposed by Martínez and Alonso, and they found it correlated better with the mass spectra of small carbon clusters [112].

The mixing energy of bimetallic clusters is used to analyze the effect of alloying,

$$\Delta(A_nB_m) = E_{\text{tot}}(A_nB_m) - \frac{nE_{\text{tot}}(A_N) + mE_{\text{tot}}(B_N)}{N}, \quad (3.5)$$

which compares the total energy of the bimetallic cluster with the total energies of the most stable monometallic clusters of the same size. The mixing energy takes negative values when there is a favorable mixing, while positive values suggest demixing tendencies [5].

During the study of molecule adsorption on gas-phase clusters, the adsorption energy E_{ads} is used to measure the interaction between the molecules and the clusters. The adsorption energy was also used to analyze the bonding strength between the clusters and the metal oxide substrates, and is given by

$$E_{\text{ads}} = E_{\text{adsorbate}} + E_{\text{adsorbent}} - E_{\text{total}}, \quad (3.6)$$

where $E_{\text{adsorbate}}$, $E_{\text{adsorbent}}$, and E_{total} are the total energies of the adsorbate, the adsorbent and the combined system, respectively. It must be noted that these total energies are those of each system relaxed independently. Higher adsorption energy values indicate stronger bonding between the adsorbate and the adsorbent.

While there can be multiple ways to analyse the nucleation and growth of clusters, one of them is calculating the nucleation energy (E_{nucl}) [113]. For a supported cluster, E_{nucl} is given by

$$E_{\text{nucl}} = E_{\text{cluster}_N/\text{support}} + E_{\text{support}} - E_{\text{cluster}_{N-1}/\text{support}} - E_{\text{single-atom}/\text{support}}, \quad (3.7)$$

and it is calculated using the total energies of the supported cluster of size N , of the support, and of a single atom supported on the same substrate. The nucleation energy represents the energy gained or lost when a single supported atom is combined with a cluster of size $N - 1$ to form a larger cluster with N atoms. For monometallic clusters, the single atom is of the same element as the cluster. In the case of bimetallic clusters, the single atom can be of either of the metals that compose the cluster.

3.2.2 Occupation probability

In realistic conditions atoms do not remain fixed at their equilibrium positions: they are constantly moving. Molecules and clusters can translate, rotate, vibrate and even undergo structural transitions between isomers. Subnanometer metal clusters in particular have shown high degrees of fluxionality and an abundance of low-energy isomers [10, 36, 76, 77]. Considering these characteristics of metal clusters, how can we know if the GM or some other isomer is the most common structure at a given temperature? This question can be answered by computing the occupation probability of each isomer at different temperatures. To calculate these probabilities, we will represent the isomers of each cluster as an ensemble. Using the superposition approximation, we can express the canonical partition function of the PES as the sum of the contributions of each local minima [76, 77, 79]:

$$Z = \sum_k Z_k, \quad (3.8)$$

where Z_k is the individual partition function corresponding to the isomer a . The partition functions of each isomer are calculated considering the electronic, vibrational, and rotational degrees of freedom:

$$Z_k = Z_{k,elec}Z_{k,vib}Z_{k,rot}. \quad (3.9)$$

The electronic partition function $Z_{elec,a}$ is

$$Z_{k,elec} = g_k e^{-\beta E_k}, \quad (3.10)$$

where g_k is the spin degeneracy the isomer k , E_k is its ground state electronic energy, $\beta = 1/kT$ and k is the Boltzmann constant.

To simplify the calculations, we will approximate the PES as a collection of harmonic potentials at the vicinity of each local minima, as shown in Figure 3.4. Then, we can use the partition functions of a quantum harmonic oscillator,

$$Z_{k,vib} = \prod_i^{3N-6} \frac{e^{-\beta h\nu_{k,i}/2}}{1 - e^{-\beta h\nu_{k,i}}}, \quad (3.11)$$

to compute the vibrational contributions for each isomer k .

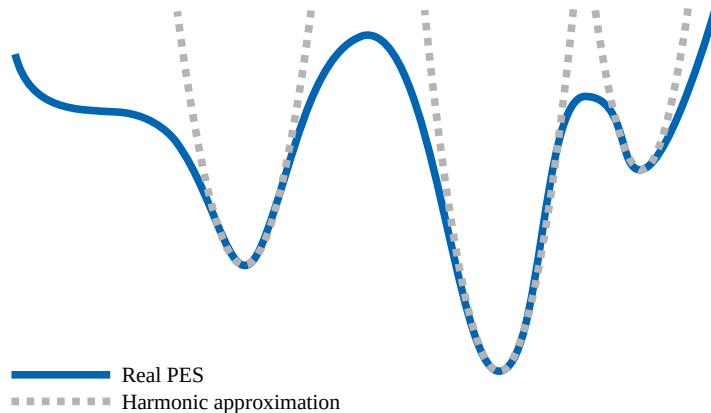


Figure 3.4: Harmonic approximation to the local minima of the PES.

Finally, the rotational partition function is given by

$$Z_{k,rot} = \frac{\sqrt{\pi}}{\sigma_k} \left(\frac{2}{\beta \hbar^2} \right)^{\frac{3}{2}} \sqrt{I_{k,1} I_{k,2} I_{k,3}}, \quad (3.12)$$

where σ_k is the order of the rotational subgroup of each isomer k , and the $I_{k,i}$ are the respective principal moments of inertia.

In this way, the occupation probability of each isomer k can be calculated as

$$P_k = \frac{Z_k}{Z}. \quad (3.13)$$

Beyond the calculation of the occupation probability, this method allows us to compute the ensemble average for any property A of the clusters at finite temperatures. This is done by calculating the property A_k for each cluster k and assigning a weight equal to the occupation probability P_k to it:

$$\langle A \rangle = \sum_k P_k A_k \quad (3.14)$$

Since the harmonic approximation does not consider the anharmonicity of the PES, this approach might not be reliable at high temperatures. However, it has been successfully applied to calculate the occupation probabilities and ensemble-averaged properties of clusters for temperatures up to 1500 K [76, 77, 114, 115].

Chapter 4

Adsorption of CO₂ and H₂ on Cu-Based Gas-Phase Clusters

Nanoparticles of precious metals such as platinum (Pt) and gold (Au) are regarded as the best catalysts due to their high stability and reactivity at low reaction temperatures [116–120]. However, its prohibitive cost and scarcity has paved the way to investigate improvements via alloying with more common transition metals [36, 37, 121–123], without reducing their performance as catalysts. Nanoalloys of transition metals have been widely studied as promising candidates for catalytic conversion of CO₂ into methanol (CH₃OH) and hydrocarbons such as methane (CH₄) [1, 2, 124–126]. The efficiency of these systems can be attributed in part to their relative stability under reaction conditions and to the synergy resulting from combining different metals [127, 128]. These effects enhance the chemical reactivity of nanoparticles and clusters, in which size and chemical ordering also play a significant role [127, 129]. The interaction of transition metal clusters with hydrogen is also of particular interest for advanced technological applications. Among these applications are the molecular conversion to renewable hydrocarbons, new hydrogen storage materials, and electrocatalytic processes such as the hydrogen evolution reaction (HER) [37, 125, 130–134]. A first step to assess the performance of clusters as catalysts is to study their interaction with relevant molecules. Nevertheless, molecular adsorption is a complex mechanism influenced by the nature of the adsorbent, the concentration of adsorbates on the adsorbent, and the temperature of the environment [3]. Therefore, the search for better catalysts requires exhaustive theoretical and experimental work. The focus of this chapter is on the study of the adsorption mechanisms of H₂ and CO₂ molecules on ultrasmall Cu-based clusters.

The study of the adsorption of CO₂ and H₂ molecules on gas-phase copper-based

$\text{Cu}_{4-x}\text{Pt}_x$ and $\text{Cu}_{4-x}\text{Au}_x$ ($x = 0-4$) clusters was carried out using the Gaussian 09 software package [102], which uses Gaussian type orbitals. The particular basis set employed was the Stuttgart/Dresden triple- ζ with relativistic effective core potentials (SDD) [105]. The exchange-correlation functional used was the Perdew-Burke-Ernzerhof GGA functional [85]. In order to identify the spin multiplicity that leads to the lowest total energy for each cluster, local geometry optimizations were performed using different multiplicity values for each composition. The spin multiplicities corresponding to the lowest total energies were used to carry out the PES exploration using a BH-DFT algorithm [110]. For each cluster, 150 basin-hopping steps were carried out. The local structure optimizations were performed using the Bernaly algorithm [101] without geometrical restrictions, with convergence conditions on forces ($< 3.0 \times 10^{-4}$ Ha/Bohr), displacements ($< 2.0 \times 10^{-3}$ Bohr), and their respective RMS values. For the optimization of the combined systems (molecules+clusters), the molecules were placed on the non-equivalent bridge, top, and hollow sites of each global minima cluster. The combined structures were then locally relaxed using the same Bernaly procedure described above. The reported results correspond to the adsorption sites with the lowest total energy.

4.1 Gas-Phase $\text{Cu}_{4-x}\text{Pt}_x$ and $\text{Cu}_{4-x}\text{Au}_x$ Clusters

Figure 4.1 depicts the most stable structures of the $\text{Cu}_{4-x}\text{Au}_x$ and $\text{Cu}_{4-x}\text{Pt}_x$ gas-phase cluster found by thoroughly exploring their PES using an *ab initio* basin hopping algorithm. The leftmost column in Figure 4.1 shows the putative global minima (GM) for each composition, and the rest of the columns show their respective low-lying isomers in order of increasing energy. All $\text{Cu}_{4-x}\text{Au}_x$ clusters found, including the monometallic Cu and Au tetramers, are planar structures. In particular, the rhombic structures of the $\text{Cu}_{4-x}\text{Au}_x$ global minima are in agreement with previous works [135–138]. The Au_4 cluster has been studied by Ghiringhelli *et al* [138] using DFT and dispersion corrections. The structures of the ground state (rhombus) and the first low-lying isomer (Y-shape) are reproduced by our calculations. The positions of the Cu and Au atoms in the rhombus as the composition changes are in full agreement with the structures predicted by Zhao *et al* [135].

In contrast with the $\text{Cu}_{4-x}\text{Au}_x$ cluster, the GM of Cu_2Pt_2 , Cu_1Pt_3 and Pt_4 are all tetrahedra, and many other $\text{Cu}_{4-x}\text{Pt}_x$ isomers found are also three-dimensional. There has been discrepancy between the Pt_4 GM geometries reported in previous works on

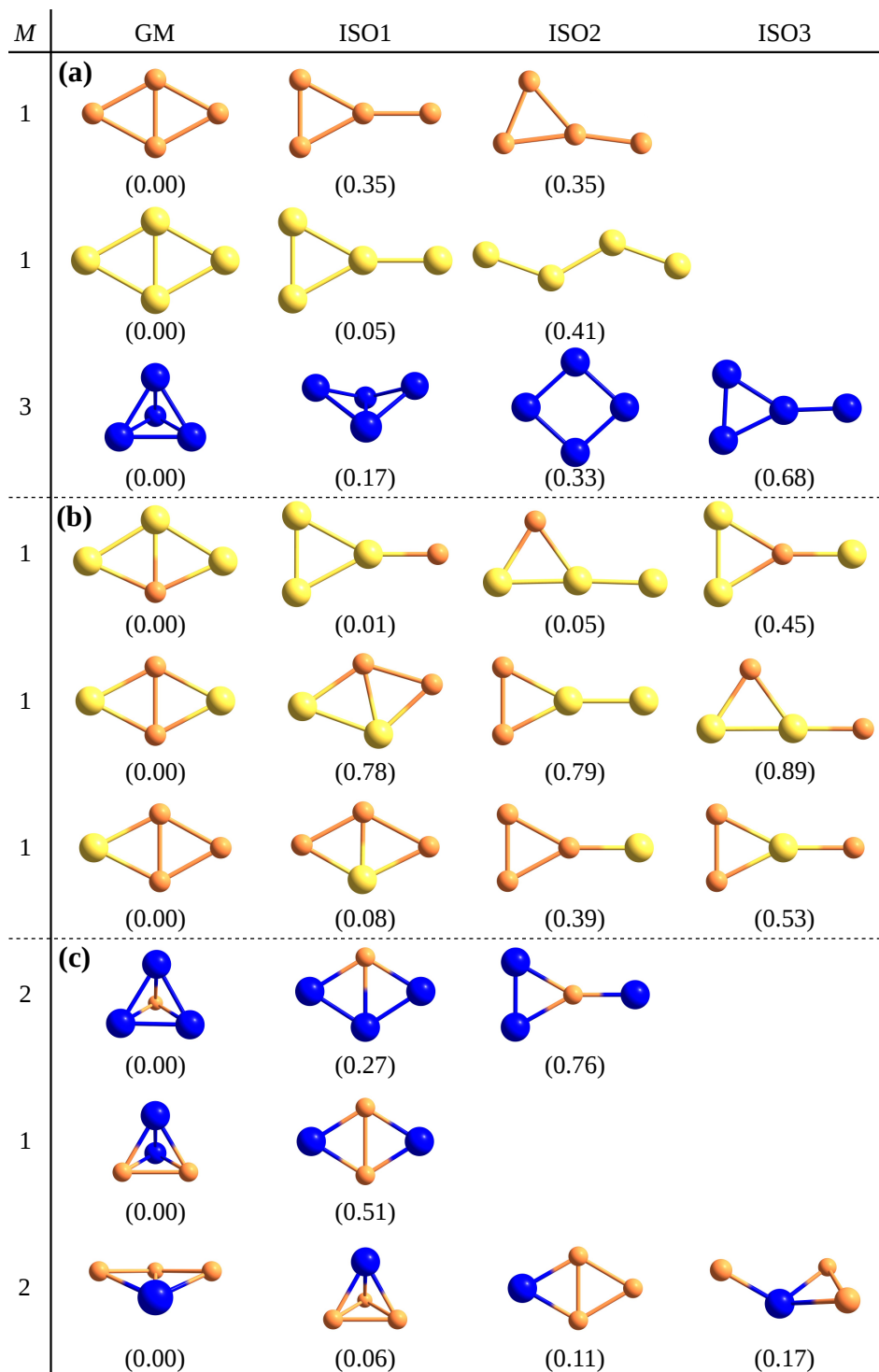


Figure 4.1: Global minima and low-lying isomers of (a) monometallic Cu_4 , Au_4 and Pt_4 clusters; (b) bimetallic $\text{Cu}_{4-x}\text{Au}_x$ clusters; and (c) bimetallic $\text{Cu}_{4-x}\text{Pt}_x$ clusters. Copper atoms are shown in orange, gold atoms in yellow, and platinum atoms in blue. The relative total energies (in eV) with respect to the GM are shown in parentheses. The value is M the multiplicity that minimizes the total energy of the respective cluster.

Table 4.1: Calculated HOMO-LUMO gap values (E_g , in eV), binding energies (E_b , in eV), mixing energies per atom (Δ/N , in eV/atom), spin multiplicities M , average bond lengths ($\langle d_{\text{Cu-Cu}} \rangle$, $\langle d_{\text{Cu-M}} \rangle$, and $\langle d_{\text{M-M}} \rangle$, in Å), and point group symmetries for the bimetallic $\text{Cu}_{4-x}\text{M}_x$ ($M = \text{Pt, Au}$) GM clusters.

Cluster	E_g	E_b	Δ/N	M	$\langle d_{\text{Cu-Cu}} \rangle$	$\langle d_{\text{Cu-M}} \rangle$	$\langle d_{\text{M-M}} \rangle$	Point group
Cu_4	0.98	1.50	0.00	1	2.37	-	-	D_{2h}
Cu_3Pt_1	0.47	1.91	-0.03	2	2.41	2.44	-	C_{2v}
Cu_2Pt_2	0.64	2.37	-0.13	1	2.51	2.48	2.63	C_{2v}
Cu_1Pt_3	0.48	2.72	-0.10	2	-	2.53	2.61	C_{3v}
Pt_4	0.13	2.99	0.00	3	-	-	2.63	T_d
Cu_3Au_1	1.35	1.63	-0.15	1	2.35	2.53	-	C_{2v}
Cu_2Au_2	1.66	1.74	-0.28	1	2.33	2.51	-	C_s
Cu_1Au_3	1.29	1.61	-0.15	1	-	2.51	2.71	C_{2v}
Au_4	0.97	1.44	0.00	1	-	-	2.72	D_{2h}

DFT-based global optimization. Trinchero *et al* also found the tetrahedron as the GM [139], while Chaves *et al* reported the bent-rhombus as the lowest energy structure [140]. This disagreement highlights the intrinsic differences between using plane-waves and gaussian-type orbitals as basis sets. The differences in the structural trends of $\text{Cu}_{4-x}\text{Au}_x$ and the $\text{Cu}_{4-x}\text{Pt}_x$ bimetallic clusters can be attributed to the electronic configurations of Au and Pt atoms.

The energetic and structural properties of the $\text{Cu}_{4-x}\text{Au}_x$ and $\text{Cu}_{4-x}\text{Pt}_x$ GM clusters calculated in this work are summarized in Table 4.1. In general, the energy gaps

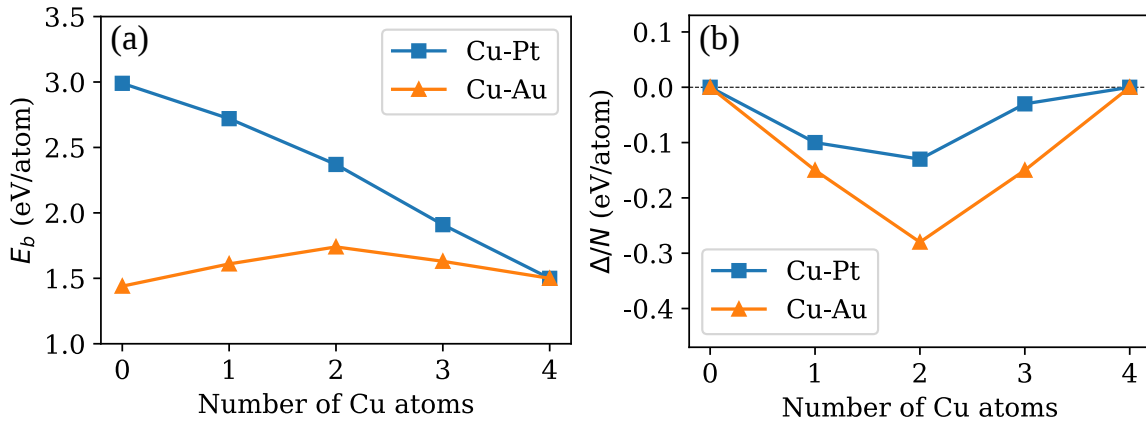


Figure 4.2: (a) Binding energy per atom and (b) mixing energy per atom for the $\text{Cu}_{4-x}\text{Au}_x$ and $\text{Cu}_{4-x}\text{Pt}_x$ GM clusters, as a function of the number of Cu atoms.

between the highest occupied molecular orbitals (HOMO) and the lowest unoccupied molecular orbitals (LUMO) are consistently wider in Au-containing clusters than in their Pt-containing counterparts. The binding energies and mixing energies for the $\text{Cu}_{4-x}\text{Pt}_x$ and $\text{Cu}_{4-x}\text{Au}_x$ clusters were calculated to assess the structural stability of each composition. From Figure 4.2 it can be seen that binding energies per atom are higher in the $\text{Cu}_{4-x}\text{Pt}_x$ clusters compared to the values for the $\text{Cu}_{4-x}\text{Au}_x$ clusters. This trend indicates that Cu atoms form stronger bonds with Pt atoms than with Au atoms. The mixing energy is negative for all the bimetallic GM structures considered, implying a favorable mixing tendency, especially for Cu_2Au_2 and Cu_2Pt_2 .

4.2 Adsorption of H_2 on $\text{Cu}_{4-x}\text{Pt}_x$ and $\text{Cu}_{4-x}\text{Au}_x$ Gas-Phase Clusters

The configurations with the lowest total energy for each composition are shown in Figure 4.3. For the Cu_{4-x} and the bimetallic $\text{Cu}_{4-x}\text{Au}_x$ clusters, the adsorption was non-dissociative and the preferred adsorption site was on-top of the tri-coordinated Cu atoms. In contrast, for the Au_4 and the bimetallic $\text{Cu}_{4-x}\text{Pt}_x$ clusters, the lowest-energy configurations were those where the H-H bond was cleaved, resulting in a dissociative adsorption. These results are in agreement with previous works on the adsorption of hydrogen on Au-based bimetallic clusters by Zhao *et al* [135], and Fang and Kuang [141]. While the adsorption is always dissociative in the clusters containing Pt, no clear trend was observed on the position of the two H atoms of the dissociated molecule. The dissociative adsorption of hydrogen on some cationic platinum clusters (Pt_2^+ - Pt_7^+) has been observed experimentally by Kerpel *et al* [142].

Figure 4.4 shows the calculated adsorption energy values for H_2 on the $\text{Cu}_{4-x}\text{M}_x$ ($\text{M} = \text{Pt}, \text{Au}$) clusters. In general, the calculated E_{ads} values for the $\text{Cu}_{4-x}\text{Pt}_x$ clusters were higher than for those containing Au. The E_{ads} values of H_2 adsorbed on the $\text{Cu}_{4-x}\text{Au}_x$ clusters remained inside a somewhat narrow range, from 0.50 to 0.65 eV, as can be observed from Figure 4.4, with the lowest value corresponding to the bimetallic Cu_2Au_2 , and the highest value to the monometallic Au_4 cluster. For the $\text{Cu}_{4-x}\text{Pt}_x$ clusters, the E_{ads} values showed a tendency to increase with the number of Pt atoms, from 0.54 eV for the monometallic Cu_4 cluster, up to 1.65 eV for Pt_4 . The values of E_{ads} are consistent with the results of Zhao *et al* [135] for $\text{Cu}_{4-x}\text{Au}_x$ clusters and Petkov

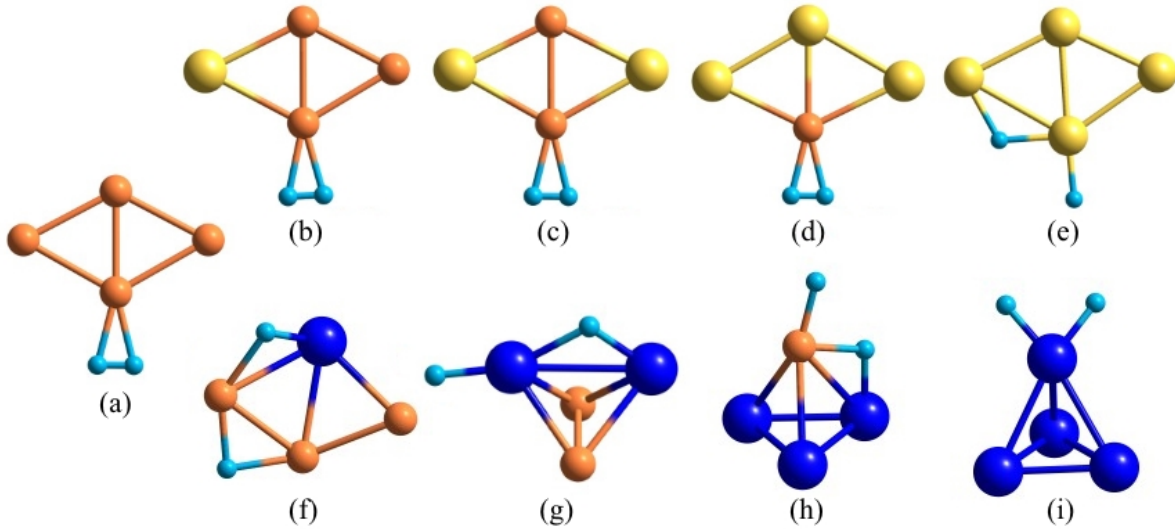


Figure 4.3: Lowest-energy configurations of molecular H₂ adsorbed on: (a) Cu₄, (b) Cu₃Au₁, (c) Cu₂Au₂, (d) Cu₁Au₃, (e) Au₄, (f) Cu₃Pt₁, (g) Cu₂Pt₂, (h) Cu₁Pt₃, and (i) Pt₄. H atoms are shown in cyan.

et al [143] for tetrahedral Pt₄. It has been shown that dispersion interaction can play an important role in the adsorption mechanisms of molecules on clusters [144, 145]. In this work, the effects of dispersion corrections on the adsorption energies were analyzed using the Grimme's semiempirical DFT-D3 method [95]. The results are summarized in Table 4.4. The dispersion contribution had a constant value of 0.04 eV for all clusters. While this value may seem small, it contributes to a percent change in the E_{ads} between 6% and 8% for Cu_{4-x}Au_x clusters.

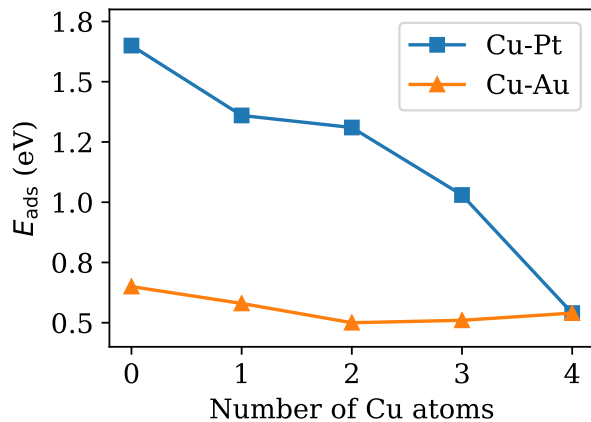


Figure 4.4: Adsorption energy values for the H₂ molecule adsorbed on the Cu_{4-x}M_x clusters, as a function of the number of Cu atoms.

Table 4.2: HOMO-LUMO gap value (E_g , eV) and adsorption energy (E_{ads} , eV) before (bare) and after H_2 adsorption (with H_2).

Cluster	E_g		E_{ads}	
	bare	with H_2	PBE	PBE+D3
Cu_4	0.98	1.84	0.54	0.58
Cu_3Pt_1	0.47	0.34	1.03	1.07
Cu_2Pt_2	0.64	0.86	1.31	1.37
Cu_1Pt_3	0.48	0.28	1.36	1.40
Pt_4	0.13	0.65	1.65	1.69
Cu_3Au_1	1.35	2.11	0.51	0.55
Cu_2Au_2	1.66	2.29	0.50	0.54
Cu_1Au_3	1.30	1.87	0.58	0.62
Au_4	0.98	2.20	0.65	0.69

The electronic HOMO-LUMO gap values (E_g) are considered reactivity descriptors for metal clusters. The E_g values for the $\text{Cu}_{4-x}\text{Au}_x$ and $\text{Cu}_{4-x}\text{Pt}_x$ clusters before and after adsorbing the H_2 molecule are shown in Figure 4.5. In general, there is correlation between the magnitude of E_{ads} and the E_g values of those clusters. The cluster containing Pt have narrower gaps and higher H_2 -adsorption energy values. In contrast, clusters with Cu present wider gaps and lower E_{ads} values. However, this correlation is only qualitative and other effects must be considered to fully understand the adsorption mechanisms. In particular, both Cu_4 and Au_4 have roughly the same E_g value (0.98 and 0.97 eV, respectively). However, the adsorption mode of H_2 is molecular on Cu_2 , but dissociative on Au_4 . This difference can be attributed to the contraction of s and p orbitals, and expansion of d and f due to relativistic effects. These effects are prominent in gold, but negligible in copper [146]. This affects the cluster reactivity leading to dissociation of the H_2 molecule [147, 148].

The adsorption of the H_2 molecule changes the HOMO-LUMO gaps of the clusters. For the $\text{Cu}_{4-x}\text{Au}_x$ clusters, the gap widens after adsorbing the hydrogen molecule, as can be seen in Figure 4.5. This effect suggests that adsorption of a second hydrogen molecule is less favorable than adsorption of the first one. The clusters containing Pt did not show a clear trend for the change in the HOMO-LUMO gap, but its value remained below 1.0 eV. These low values of E_g suggest that dissociative adsorption of a second H_2 is possible.

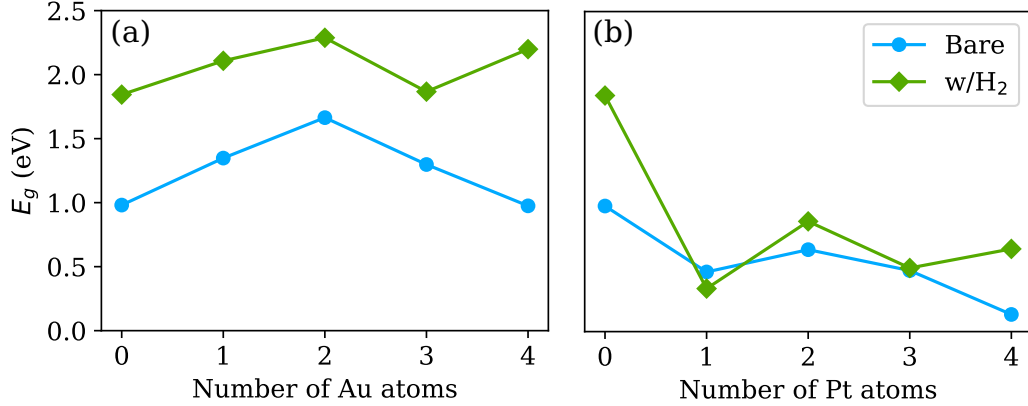


Figure 4.5: Frontier orbitals HOMO-LUMO gap values for the (a) $\text{Cu}_{4-x}\text{Au}_x$ and the $\text{Cu}_{4-x}\text{Pt}_x$ clusters, before (bare) and after adsorption (w/ H_2).

The interaction with the hydrogen molecule preserved the shape of the clusters, but induced small changes in the interatomic distances. Correspondingly, the interaction of the H_2 molecule with the clusters modified its structure after being adsorbed. Table 4.3 summarizes the structural changes of the hydrogen molecule. In general, the metal-metal bonds extended from 0.25% up to 1.92% after adsorbing the H_2 molecule.

Table 4.3: Bond length ($d_{\text{H-H}}$, Å) and harmonic stretching mode frequency value ($\nu_{\text{H-H}}$, cm^{-1}) in the free H_2 molecule before and after the molecule is adsorbed on the metal clusters (excluding cases corresponding to dissociative adsorption). Average metal-hydrogen bond lengths ($\langle d_{\text{M-H}} \rangle$, Å) are given for both molecular and dissociative adsorption. The values omitted of $d_{\text{H-H}}$ and $\nu_{\text{H-H}}$ correspond to the cases where the H-H bond was cleaved upon being adsorbed and, as a result, the H-H stretching mode disappeared.

	$d_{\text{H-H}}$	$\nu_{\text{H-H}}$	$\langle d_{\text{M-H}} \rangle$
Free	0.75	4328.28	-
Cu ₄	0.83	3201.02	1.70
Cu ₃ Pt ₁	-	-	1.71
Cu ₂ Pt ₂	-	-	1.71
Cu ₁ Pt ₃	-	-	1.58
Pt ₄	-	-	1.57
Cu ₃ Au ₁	0.82	3347.77	1.71
Cu ₂ Au ₂	0.82	3373.48	1.72
Cu ₁ Au ₃	0.82	3311.75	1.70
Au ₄	-	-	1.71

Meanwhile, the H-H bond in the H₂ molecule elongated upon being adsorbed and the vibrational frequency of the H-H stretching mode decreased. The average metal-hydrogen bond lengths were fairly similar for all compositions, with values ranging from 1.57 Å to 1.72 Å.

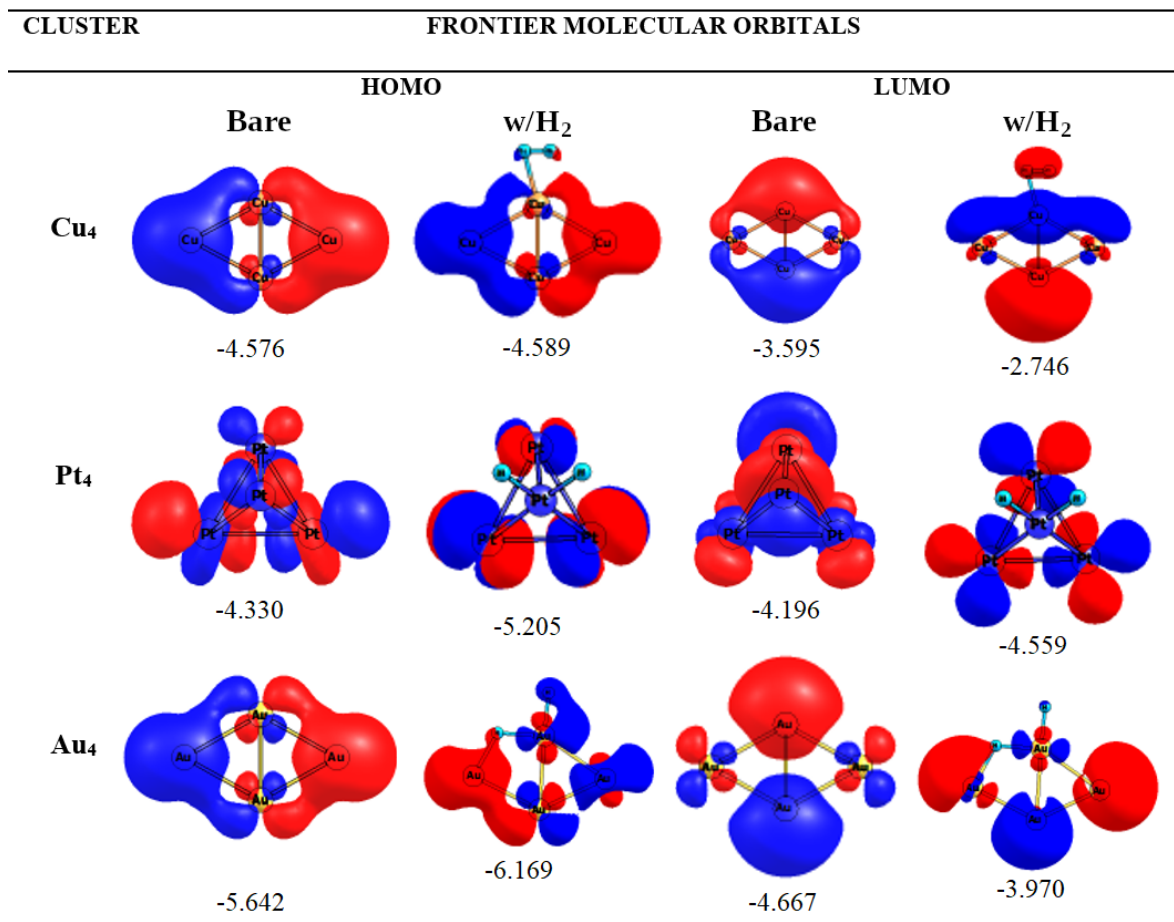


Figure 4.6: HOMO and LUMO frontier orbitals of the monometallic Cu₄, Pt₄, and Au₄ clusters before (bare) and after (w/H₂) adsorption of the H₂ molecule. The orbital eigenvalue energy (in eV) is shown below each MO.

Using the natural bond orbital (NBO) approach [149], the frontier orbitals of the clusters were calculated to elucidate the bonding mechanisms with the H₂ molecules. Figure 4.6 depicts the HOMO and LUMO frontier orbitals of Cu₄, Pt₄, and Au₄ clusters before (bare) and after adsorption (w/H₂). In the rhombus shaped Cu₄ and Au₄ bare clusters, the HOMO is distributed mainly around the atoms located at the vertices along the longest diagonal. A localized distribution of the HOMO around each Pt atom is observed for the Pt₄ bare cluster. In the three clusters the HOMO orbitals avoid the inner (hollow) region of the clusters. The spatial distribution of the LUMO orbital in

Cu_4 and Au_4 is opposite to that of the HOMO. The LUMO orbital is concentrated around the two atoms on the vertices of the short diagonal, avoiding again the hollow region. In Pt_4 the LUMO is distributed over the whole cluster. In the clusters with the adsorbate the global reactivity is modified due to the broadening of the HOMO-LUMO gap, which in turn occurs because of the changes in the energies of the frontier orbitals induced by the adsorption of hydrogen. In H_2Cu_4 this change consists in a strong lifting up of the energy of the LUMO orbital, while the change of the HOMO energy is negligible. The shape of the HOMO orbital in H_2Cu_4 is quite similar to that in Cu_4 and shows practically no contribution from the H atoms. This is because the orbitals of non-dissociated H_2 adsorbed on transition metals lie quite deep in energy [150]. For the three clusters, the NBO charges indicate that electron density is partially redistributed among atoms, thus giving stability to the overall cluster structure. Figure 4.7 shows the natural charge distribution before and after H_2 adsorption in clusters Cu_4 , Pt_4 , and Au_4 . In all cases, a small amount of charge remains on the H atoms attached to the respective metal atoms.

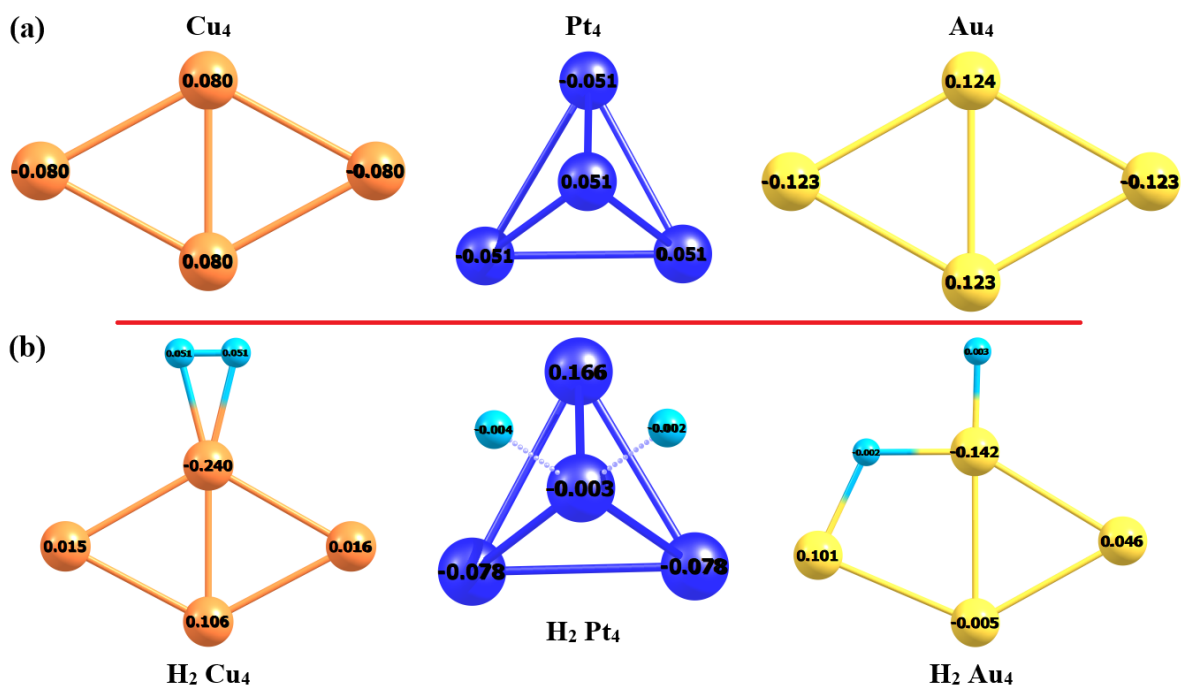


Figure 4.7: Natural charge distribution obtained from the natural population analysis calculation for (a) bare Cu_4 , Pt_4 , and Au_4 metal clusters, and (b) metal clusters with adsorbed H_2 . A negative sign indicates a gain of electronic charge.

4.3 Adsorption of CO₂ on Gas-Phase Cu_{4-x}Pt_x Clusters

The study of the adsorption of H₂ on Cu_{4-x}Pt_x and Cu_{4-x}Au_x revealed that the clusters containing Pt showed a higher reactivity, at least for this particular size. Considering this, the study of the adsorption of CO₂ was carried on only for the Cu_{4-x}Pt_x tetramers. The lowest-energy configurations of the CO₂ molecules adsorbed on the Cu_{4-x}Pt_x gas-phase clusters are shown in Figure 4.8. The calculations were carried out starting from several non-equivalent adsorption sites, and it was found that the CO₂ molecules prefer binding to these clusters in a bridge position. For bimetallic clusters, except Cu₃Pt₁, the CO₂ molecule binds to the metal cluster via its C-O in a bridge position between the Cu and Pt atoms, with the C atom always bound to a Pt atom.

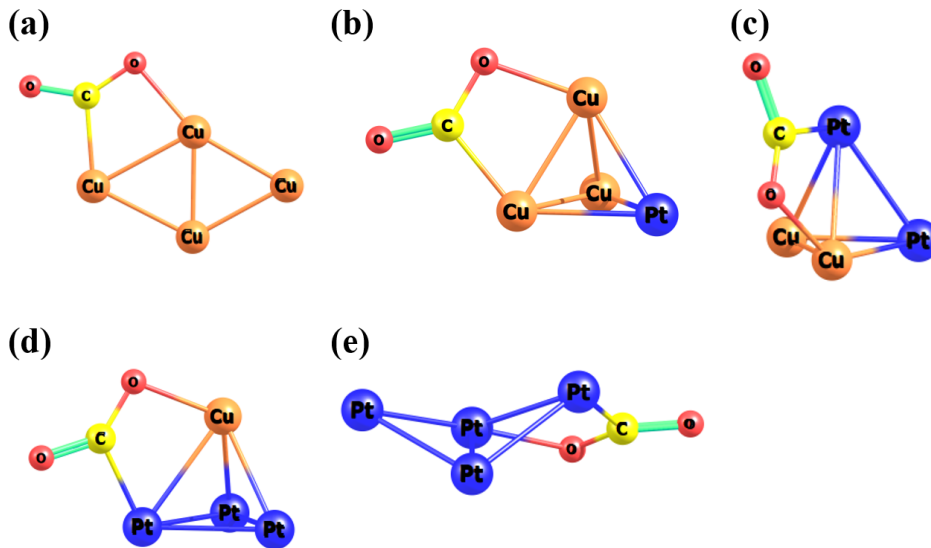


Figure 4.8: Lowest-energy configurations of the CO₂ molecule adsorbed on the Cu-Pt clusters: (a) Cu₄, (b) Cu₃Pt₂, (c) Cu₂Pt₂, (d) Cu₁Pt₃, and (e) Pt₄.

The effects of the dispersion interactions were also considered for these systems. In this case, they were included by using the long-range corrected hybrid functional ω B97XD [151]. The impact of using this hybrid functional on the structure of the clusters—compared to the results using PBE—was minimal. However, the resulting E_{ads} and E_g values increased significantly compared to those obtained with PBE, as seen in Table 4.4. This is likely due to parameterization of the ω B97XD functional and the inclusion of a 100% long-range exact-exchange. For metal clusters, it has been previously reported that using Hartree-Fock exchange within hybrid functionals leads

to inaccurate description of the electronic structure for small metal clusters [151–153]. Following this consideration, only results obtained using the PBE functional are discussed for CO₂ adsorption on the Cu-Pt clusters.

Table 4.4: HOMO-LUMO gap value (E_g , eV) and adsorption energy (E_{ads} , eV) before (bare) and after CO₂ adsorption (with CO₂).

Cluster	E_g		E_{ads}	
	bare	with CO ₂	PBE	ω B97XD
Cu ₄	0.98	1.00	0.81	3.02
Cu ₃ Pt ₁	0.47	0.50	1.01	2.99
Cu ₂ Pt ₂	0.64	1.04	1.64	3.93
Cu ₁ Pt ₃	0.48	0.28	1.44	3.63
Pt ₄	0.13	0.27	1.16	3.09

The calculated adsorption energy values (E_{ads}) of the CO₂ molecules on the Cu-Pt tetramers are shown in Table 4.4, alongside the HOMO-LUMO frontier orbital gaps for the clusters before and after adsorbing the molecules. For most of the clusters, the calculated adsorption energy is larger than 1 eV, except for the Cu₄ cluster onto which CO₂ adsorption strength is 0.81 eV using the PBE functional. This value compares quite well with that obtained by Liem and Clarke [154] of a bent CO molecule adsorbed on Cu(110) surface. The strongest E_{ads} value (1.64 eV) corresponds to the bimetallic Cu₂Pt₂ cluster, and it decreases as the number of Cu or Pt atoms in the cluster increases (see Figure 4.9). The Cu₄ cluster has the lowest E_{ads} at 0.81 eV, which is close to the value found by Liem and Clarke [154] (0.751 eV) for a bent CO₂ molecule adsorbed on a Cu(110) surface. For most clusters, except for Cu₁Pt₃, the HOMO-LUMO gap widens upon adsorption of the CO₂ molecule.

In all cases, the initially linear CO₂ molecule bends after being adsorbed by the clusters. This phenomenon has been reported to happen on both metal surfaces [154, 155] and metal clusters [7], and is related to an increased reactivity of the CO₂ molecules. In order to analyze the cause of the molecule bending, the LUMO frontier orbitals were calculated for both the linear CO₂ molecule and the clusters with the adsorbate (Figure 4.10). For most clusters, excluding the Pt-rich Pt₄ and Cu₁Pt₃, it can be observed that electron density transfers from the LUMO of the cluster to the LUMO of the CO₂ molecule. This transfer is necessary to stabilize the combined system configuration

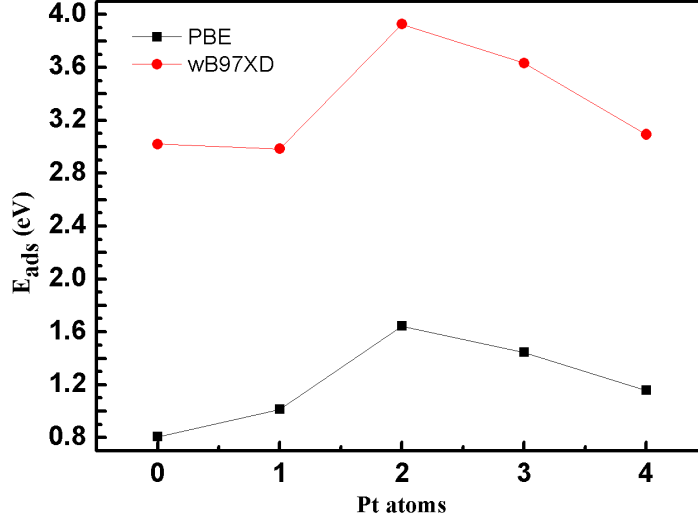


Figure 4.9: Adsorption energy E_{ads} for the CO_2 molecule adsorbed on each $\text{Cu}_{4-x}\text{Pt}_x$ GM clusters, as a function of the number of Pt atoms.

[156]. Table 4.5 lists the average C-O distance in the CO_2 molecule and the O-C-O angle, before and after the adsorption; as well as the total natural charge for each cluster after adsorbing the CO_2 molecule. The positive values of the total charges corroborate that electron density transfers from the clusters to the molecules.

The structures of most clusters remained unchanged after adsorbing the molecule, except for Cu_1Pt_3 and Pt_4 , which underwent isomerization. The Pt_4 cluster transformed from a tetrahedron to a bent rhombus, and Cu_3Pt_1 , initially a rhombus, folded to become a tetrahedron. These dynamic transformations are similar to those reported in direct imaging experiments of Au_{20} clusters [157], where they found that Au_{20} cycles between its isomer structures. This peculiar behavior justify the analysis of the PES

Table 4.5: Average C-O bond length ($\langle d_{\text{C-O}} \rangle$, in Å) and O-C-O angle value of the CO_2 molecules, and total natural charge for each clusters after molecule adsorption (δ^+)

	$\langle d_{\text{C-O}} \rangle$	$\angle \text{OCO}$	δ^+
Linear	1.21	180.0	-
Cu_4	1.27	138.6	0.48
Cu_3Pt_1	1.29	132.5	0.59
Cu_2Pt_2	1.29	136.6	0.46
Cu_1Pt_3	1.28	137.2	0.45
Pt_4	1.29	134.3	0.41

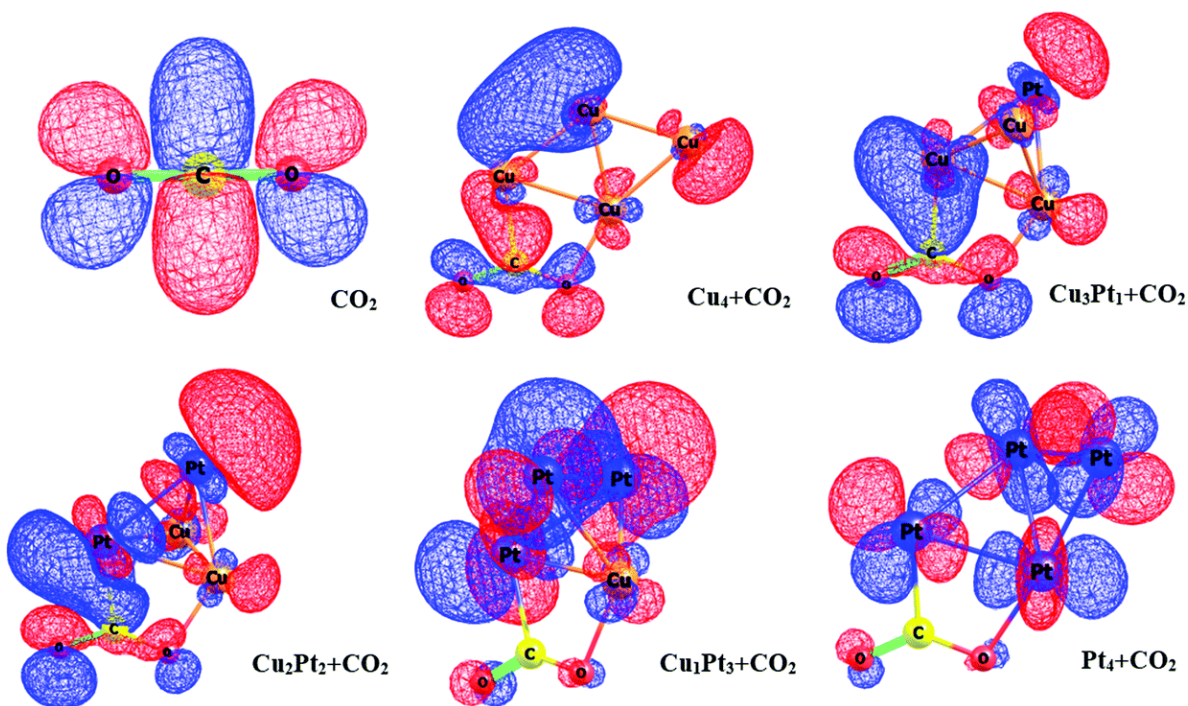


Figure 4.10: LUMO frontier orbital isosurface plot of the linear CO_2 molecule and the $\text{Cu}_{4-x}\text{Pt}_x$ clusters with the adsorbed CO_2 molecule.

flatness associated with these metal clusters. For this purpose, the transition state (TS) energy barriers between the GM and the first isomer structures were calculated using the linear synchronous transit (LST) method, as shown in Figure 4.11. For Pt_4 , the TS barrier is rather small (0.30 eV) and the activation energy from the ISO1 to the GM is ~ 0.08 eV. These characteristics explain the fluxional character of the Pt_4 cluster assisted via the CO_2 interaction. For Cu_3Pt_1 cluster the estimated activation energy resulted to be about 0.60 eV, twice as that of the Pt_4 cluster. However, the energy difference between its ISO1 and its GM is only 0.06 eV. Compared to the clusters that did not exhibit conversion, both the energy barrier and the energy difference between the GM and the first isomer are smaller in those cases which isomerized. These results highlight the importance of the fluxional nature of metal clusters in catalytic processes. Therefore, it is crucial to consider the low lying isomers—not only the global minimum—to fully understand the properties of these systems.

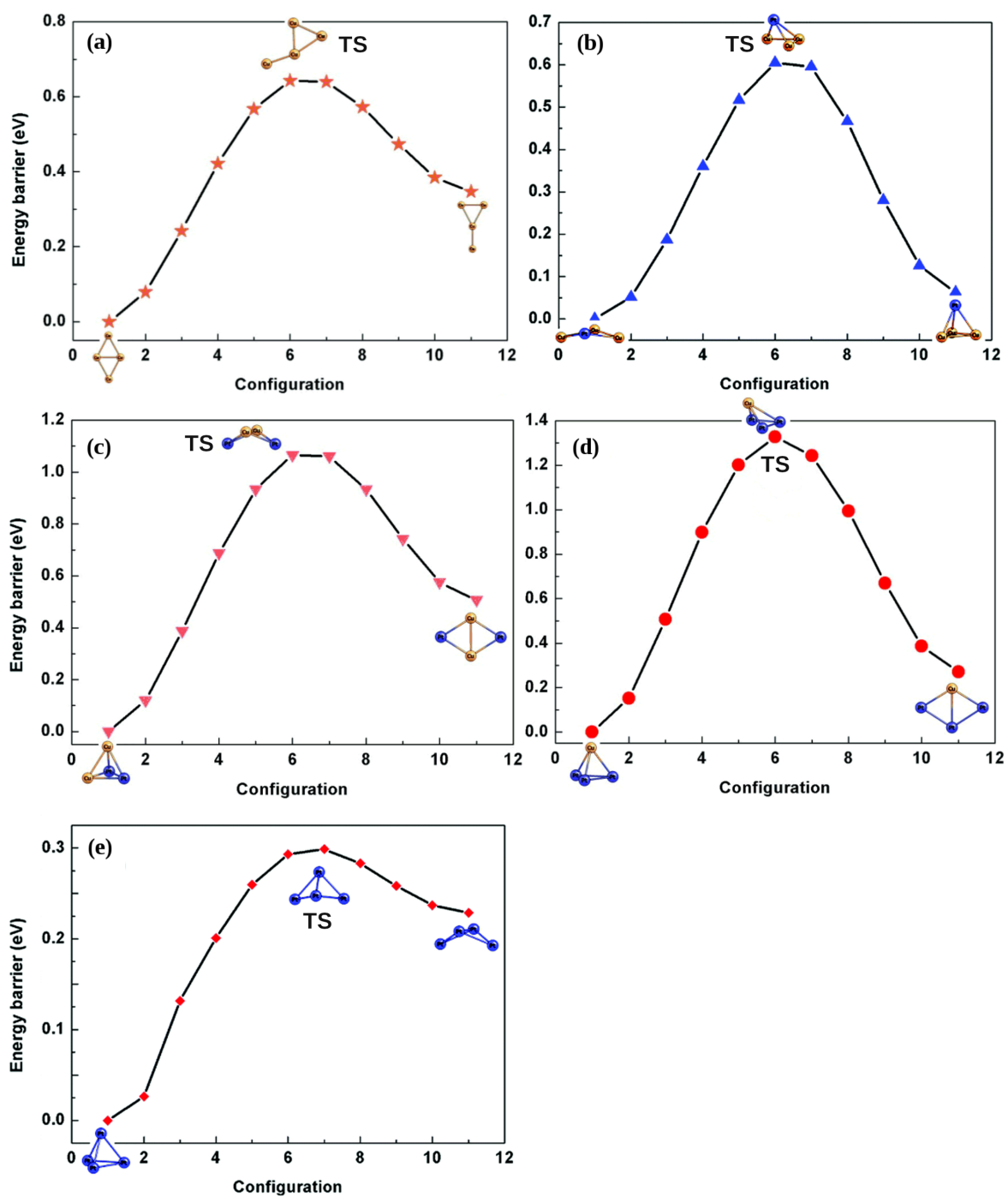


Figure 4.11: Transition state energy barriers between the GM and their respective first isomers for (a) Cu₄, (b) Cu₃Pt₂, (c) Cu₂Pt₂, (d) Cu₁Pt₃, and (e) Pt₄.

Chapter 5

Gas-Phase and γ -Al₂O₃-Supported Re_nPt_m Clusters

Platinum-based materials are widely considered the best catalysts for a variety of important reactions in energy conversion, such as oxygen reduction [158, 159]. In particular, when alloyed with rhenium—one of the rarest elements on Earth—Re-Pt alloys have found niche applications such as superalloys in turbine blades [160], in low-temperature water-gas shift reactions [161, 162], as efficient catalysts for high octane gasoline production via hydrocarbon reforming [163–166], or as direct ethanol fuel cells (DEFC) when Sn is also included [167]. The superior catalytic activity of such bimetallic catalyst and its increased stability—namely against coking—has been experimentally rationalized as a conjunction of structural and electronic effects due to Re content [168–170]. In this respect, computational studies—mostly based on DFT calculations—have contributed extensively to the understanding of the effects of the interaction between Pt-based bimetallic clusters - both gas-phase and supported - with small adsorbates such as O₂, CO, CO₂, ethylene and ethanol for example [36–43]. Some of these previous studies have remarked the importance of the putative global minimum structure, as well as low-lying isomers exhibiting structural changes in both, cluster and molecule, the former showing structural inter-conversion and the latter the existence of molecular activation or even dissociation. In particular, Re clusters have been studied in the gas-phase [89, 171, 172], supported on graphene [173], acting as a doping agent in Au [174, 175], Co [176], Sn [177] and Si [178] clusters; or even forming Re-Pt unsaturated complexes surrounded by organic ligands [179, 180]. Although previous DFT-based computational studies have dealt with Re-based alloys catalysts [181–183] (including Re-Pt) there is a lack of work in the literature on the description of the geometrical and electronic properties of bimetallic Re-Pt clusters.

For the study of Re-Pt clusters, both in the gas-phase and supported, the PES explorations were carried out using a DFT basin-hopping algorithm implemented in Python (BH-DFT) [111]. In this case, 100 BH-DFT steps were performed for each cluster size and composition. The BH-DFT code was coupled to the Quantum Espresso software, which uses plane-wave basis sets and pseudopotentials [103, 104]. The electronic calculations were performed at the GGA-PBE level of theory [85]. Scalar relativistic pseudopotentials were used to model the core electrons. To speed up the initial exploration of the PES, the energy cutoffs used were 20 Ry for the kinetic energy and 160 Ry for the charge density. These values were doubled for the re-optimization stage. The local relaxations were stopped when the convergence criteria for the energy ($< 1.0 \times 10^{-4}$ Ry) and for the forces ($< 1.0 \times 10^{-3}$ a.u.) were reached. A Marzari-Vanderbilt occupation smearing of 0.01 Ry was applied to broaden the density of states at the Fermi level [184]. For the gas-phase clusters, all calculations were done in a simple cubic cell of side 10 Å to avoid interaction between the periodic images. For the supported clusters, we used a simulation cell with dimensions $a = 21.13$ Å, $b = 31.82$ Å and $c = 40.55$ Å, and angles $\alpha = \beta = \gamma = 90^\circ$. The γ -Al₂O₃ (100) surface was constructed using the model proposed by Digne *et al* [185, 186]. Slabs composed of 2x2 unit cells with four atomic layers were used to model the γ -Al₂O₃ substrate. The slabs were separated by a vacuum of 20 Å perpendicular to the surface. In all cases, the reciprocal space was sampled at the Γ point only.

5.1 Re_nPt_m Gas-Phase Clusters

The putative global minima (GM) of the gas-phase clusters are shown in Figure 5.1, along with their respective symmetry point groups and binding energies. It can be seen that, in bimetallic clusters, Re atoms tend to aggregate while most Pt atoms remain separated from each other, even in Pt-rich clusters. This trend indicates that Re-Re and Re-Pt bonds predominate over Pt-Pt bonds.

In general, Re_n clusters have shorter interatomic distances than Pt_m clusters of the same size. This is a consequence of the stronger Re-Re bonds and the corresponding higher binding energy values.

The relative stability of the pure clusters was analyzed by means of the functions Δ_2

N	Re_N	$\text{Re}_{N-1}\text{Pt}_1$	$\text{Re}_{N-2}\text{Pt}_2$	$\text{Re}_{N-3}\text{Pt}_3$	$\text{Re}_{N-4}\text{Pt}_4$	$\text{Re}_{N-5}\text{Pt}_5$	Pt_6
2	 2.02 Triplet, $D_{\infty h}$	 2.06 Sextet, $C_{\infty v}$	 1.90 Triplet, $D_{\infty h}$				
3	 2.69 Quartet, C_{2v}	 2.82 Singlet, C_s	 2.95 Quartet, C_{2v}	 2.47 Triplet, D_{3h}			
4	 3.50 Singlet, D_{4h}	 3.35 Doublet, C_{2v}	 3.27 Triplet, C_1	 3.41 Doublet, D_{3h}	 2.78 Quintet, C_{2v}		
5	 3.76 Quartet, C_s	 3.75 Singlet, C_{2v}	 3.73 Doublet, C_1	 3.66 Triplet, C_1	 3.60 Singlet, C_{2v}	 3.01 Triplet, C_s	
6	 4.33 Triplet, O_h	 4.05 Quartet, C_s	 4.03 Singlet, C_s	 3.98 Doublet, C_s	 3.88 Singlet, C_{2v}	 3.73 Doublet, C_1	 3.27 Triplet, D_{3h}

Figure 5.1: Calculated putative GM monometallic Re, Pt and bimetallic Re-Pt gas-phase clusters, ranging from 2 up to 6 atoms in size for all compositions ($N = m + n$). Binding energy per atom (E_b) values are shown in eV, along with their corresponding spin multiplicities and symmetry point groups. Re and Pt atoms are shown in blue and gray, respectively.

and Δ_2^v , whose values are plotted in Figure 5.2. For the Re_n clusters, these descriptors show even-odd oscillations, suggesting that even-sized clusters are more stable than odd-sized ones. The octahedral Re_6 GM cluster seems particularly stable, both its Δ_2 and Δ_2^v values are higher than any other Re cluster, and it has the highest binding energy of all the clusters studied. This result agrees with the findings published by Miramontes *et al* [4], who report that the graphene-supported octahedral Re_6 is the most stable structure amongst the Re_n ($n < 13$) clusters. Another remarkable feature of the Re_6 GM is its small HOMO-LUMO gap of 0.07 eV, being the narrowest among all the GM clusters. Compared to the Re clusters, the values for the stability functions for the pure Pt clusters are smaller in magnitude, with Pt_6 having the highest value. Like Re_6 , the Pt_6 GM cluster has a narrow HOMO-LUMO gap, with a value of 0.14 eV.

So far we have focused our attention on the GM structures, but the study of low-

Table 5.1: Calculated binding energies (E_b , in eV), HOMO-LUMO gap values (E_g , in eV), mixing energies per atom (Δ/N , in eV/atom), spin multiplicities M , average bond lengths ($\langle d_{\text{Re-Re}} \rangle$, $\langle d_{\text{Re-Pt}} \rangle$ and $\langle d_{\text{Pt-Pt}} \rangle$, in Å), and symmetry point groups for Re_nPt_m putative global minima (GM) clusters.

Cluster	E_b	E_g	Δ/N	M	Re-Re	Re-Pt	Pt-Pt	Point group
Re_2	2.02	1.12	0.00	3	2.03	-	-	$D_{\infty h}$
Re_1Pt_1	2.06	1.06	-0.11	6	-	2.28	-	$C_{\infty v}$
Pt_2	1.90	0.38	0.00	3	-	-	2.32	$D_{\infty h}$
Re_3	2.69	0.60	0.00	4	2.18	-	-	C_{2v}
Re_2Pt_1	2.82	0.98	-0.21	1	2.04	2.31	-	C_s
Re_1Pt_2	2.95	0.63	-0.42	4	-	2.25	-	C_{2v}
Pt_3	2.47	0.17	0.00	3	-	-	2.49	D_{3h}
Re_4	3.50	0.85	0.00	1	2.24	-	-	D_{2h}
Re_3Pt_1	3.35	0.44	-0.03	2	2.27	2.50	-	C_{2v}
Re_2Pt_2	3.27	0.75	-0.13	3	2.16	2.31	-	C_1
Re_1Pt_3	3.41	0.84	-0.45	2	-	2.24	-	D_{3h}
Pt_4	2.78	0.25	0.00	5	-	-	2.52	C_{2v}
Re_5	3.76	0.29	0.00	4	2.44	-	-	C_s
Re_4Pt_1	3.75	0.55	-0.14	1	2.26	2.29	-	C_{2v}
Re_3Pt_2	3.73	0.34	-0.27	2	2.29	2.39	-	C_1
Re_2Pt_3	3.66	0.48	-0.35	3	2.13	2.37	2.55	C_1
Re_1Pt_4	3.60	0.69	-0.44	2	-	2.27	-	C_{2v}
Pt_5	3.01	0.23	0.00	3	-	-	2.47	C_s
Re_6	4.33	0.07	0.00	3	2.43	-	-	O_h
Re_5Pt_1	4.05	0.15	0.10	4	2.41	2.51	-	C_s
Re_4Pt_2	4.03	0.45	-0.05	1	2.41	2.49	-	C_s
Re_3Pt_3	3.98	0.37	-0.18	2	2.33	2.51	-	C_s
Re_2Pt_4	3.88	0.28	-0.25	1	2.18	2.43	2.71	C_{2v}
Re_1Pt_5	3.73	0.42	-0.28	2	-	2.35	2.65	C_1
Pt_6	3.27	0.14	0.00	3	-	-	2.51	D_{3h}

lying isomers is equally important, given the fluxional nature of metal clusters [10, 76, 187, 188]. Figure 5.3 shows the different Re_n GM and isomer structures found in this work. The GM structures the clusters with less than five atoms are all planar or quasi-planar, whereas the geometries of larger clusters are three-dimensional. All the Re_3 isomers are isosceles triangles. The GM of Re_4 is a square, the first isomer is a bent rhombus and the second isomer is a planar rhombus. The lowest-energy structure of Re_5 is an oblique pyramid with a trapezoidal base, the first isomer is a square pyramid, the second isomer is a triangular bipyramid, and the third isomer is a oblique pyramid with a kite base. For these clusters, we also found a few spin isomers (not shown in the figure) with the same structure as the GM and the first isomer, but with different multiplicities. Finally, besides the octahedral GM structure of Re_6 , our algorithm did

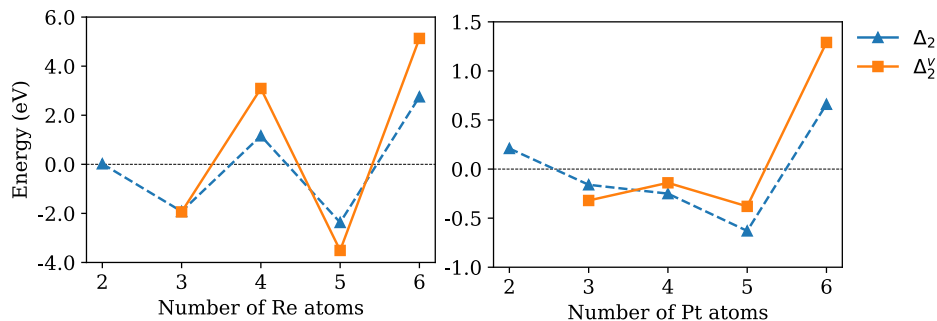


Figure 5.2: Second difference in energy Δ_2 and second difference in atom-evaporation energy Δ_2^v for (a) Re_n and (b) Pt_m clusters, as a function of the number of atoms.

not find any other low-energy isomers for this cluster.

Figure 5.3 also shows the geometries of the GM and low-lying isomers for the monometallic Pt clusters. The Pt clusters GM structures found have been previously reported in the literature [5], with the only difference being the multiplicity of Pt_3 . While the GM geometries of these clusters are all planar or quasi-planar, three-dimensional isomer structures are found in clusters with as few as four atoms. The only minimum structure we found for Pt_3 was an equilateral triangle. For Pt_4 , the GM geometry is a bent rhombus, and the first isomer is a tetrahedron. The GM structure of Pt_5 is

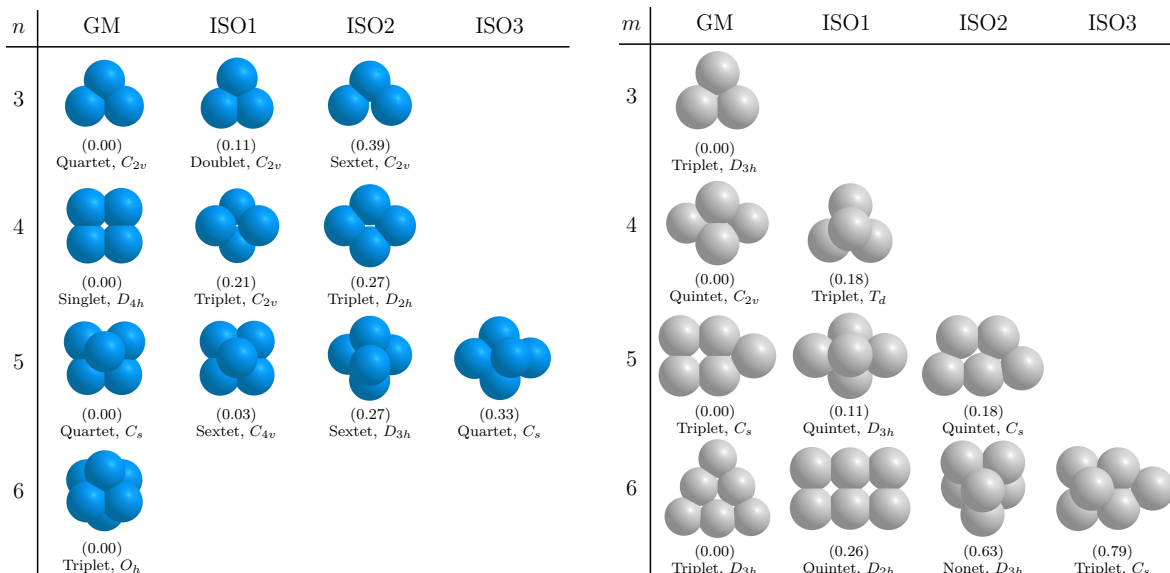


Figure 5.3: Global minima and low-lying isomers of (left) Re_n and (right) Pt_m clusters along with their corresponding multiplicities and point groups. The energy difference, in eV, between the GM structure and the respective isomer is shown in parenthesis.

made up of four atoms forming a square and the last one bonded to two of them on a bridge position. The first isomer of Pt_5 is an equilateral triangular bipyramid, and the second isomer is a planar irregular pentagon. In the Pt_6 GM structure, the six atoms are arranged in an equilateral triangle. The first isomer is a rectangle, the second isomer is a equilateral triangular prism, and the third isomer is an oblique pentagonal pyramid with an irregular base.

Table 5.1 summarizes the properties of the bimetallic GM clusters. As was previously mentioned, the Re atoms tend to aggregate in the center of the bimetallic clusters. This tendency minimizes the number of Pt-Pt bonds, with most clusters having no Pt atoms bonded together. Similarly to the monometallic clusters, the Re-Re bonds are the shortest and the Pt-Pt bond the longest, with the Re-Pt bond lengths in between. Clusters doped with a single atom feature some interesting properties.

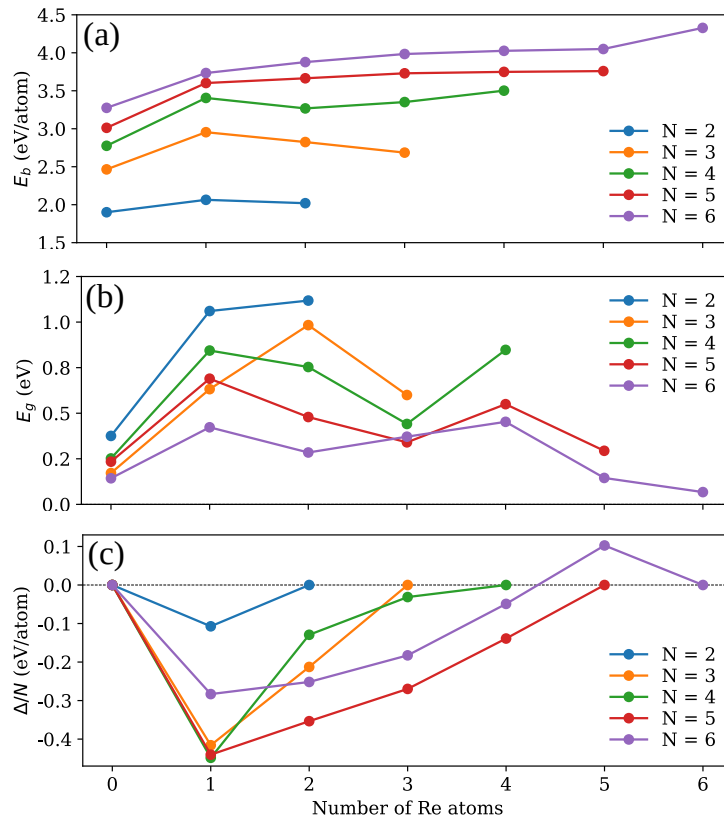


Figure 5.4: Calculated (a) binding energy per atom, (b) HOMO-LUMO gap value, and (c) mixing energy of global minima Re_nPt_m clusters as a function of the number of Re atoms.

The binding energy values for all GM clusters are depicted, as a function of the

number of Re atoms, in Figure 5.4. There is a general tendency for larger clusters and Re-rich clusters to have higher binding energy than smaller clusters or pure Pt clusters. Doping Pt clusters with a single Re atom can increase the binding energy appreciably. Like the binding energy values, the frontier HOMO-LUMO gap values (E_g), shown in the same figure, are considerably wider in bimetallic clusters with a single Re atom than in pure Pt cluster. The most favorable mixing is also found in the Re_1Pt_m clusters, which have the largest mixing energy values for each size. As can be seen from Figure 5.5, the Re atom is always located in the center of the Re_1Pt_m clusters, including their isomers. In the lowest energy configurations of these clusters, the Re atom bonds to all the Pt atoms. Reducing the number of Re-Pt bonds increases the total energy, as can be seen in the Re_1Pt_5 isomers. The trend of Re atoms to aggregate in the center of the clusters agrees with the strong anti-segregation tendency of single Re atoms in bulk Pt reported by Ruban *et al.*, wherein they calculated the surface segregation energies of transition metal atoms in transition-metal hosts [189]. The same tendency has been observed in Re-Co clusters [190]. Our findings indicate that the segregation of the Pt atoms in Re-Pt alloys can be observed in clusters as small as three atoms.

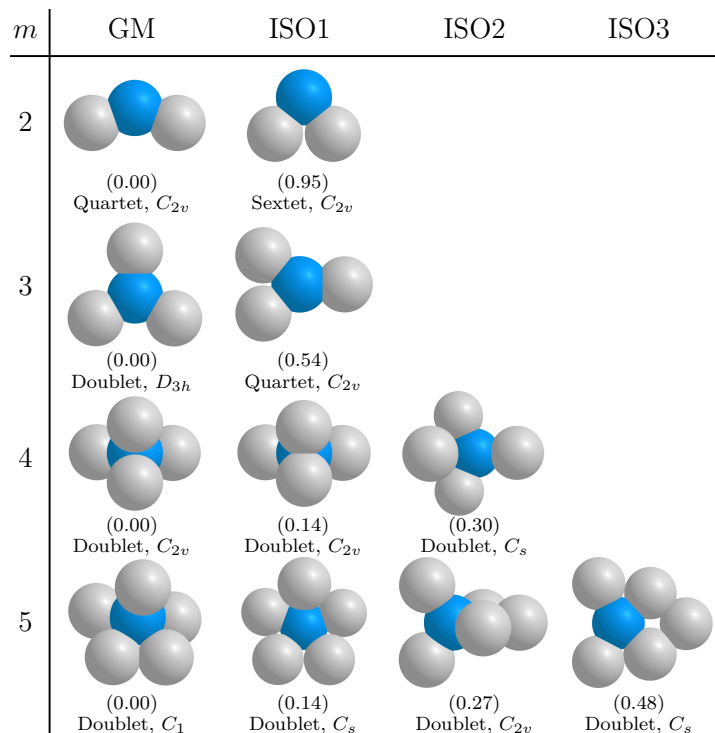


Figure 5.5: Global minima and low-lying isomers of Re_1Pt_m bimetallic clusters along with their corresponding multiplicities and point groups. The energy difference, in eV, between the GM structure and the respective isomer is shown in parenthesis.

The mixing energy gets closer to zero as the number of Re atoms increases, with Re_nPt_1 clusters having the smallest values for each size, except for Re_5Pt_1 , which is the only composition with a positive mixing energy value. The high stability of the Re_6 cluster may explain in part the demixing tendency of Re_5Pt_1 . We found that, in all Re_nPt_1 clusters, the Re atoms aggregate and the Pt atom is located on the periphery of the clusters, in some cases bonded only to a single Re atom. Amongst the clusters studied, Re_4Pt_1 was notable for having a large number of low-lying isomers with small energy differences between them, which might suggest it is a highly fluxional composition.

The projected density of states (PDOS) was employed to elucidate the bonding mechanisms of these bimetallic Re-Pt gas-phase clusters. Figure 5.13 shows the Re and Pt $5d$ and $6s$ orbital PDOS for all the Re_nPt_m pentamers. Except for Re_4Pt_1 (singlet), these clusters show spin asymmetry in their PDOS. For monometallic Pt_5 most of the contributions are from $5d$ -states, while the Re_5 cluster displays an important contribution from both $5d$ and $6s$ -states near the Fermi level; Figure 5.13(a,f). When one Pt atom is added to mix, such as in the Re_4Pt_1 cluster, both $5d$ and $6s$ -states from those Re and Pt atoms contribute to the highest occupied states within the PDOS, suggesting strong bonds formation through orbital hybridization; Figure 5.13(b). When Re atoms start occupying central sites within the cluster, such as in the Re_3Pt_2 and Re_2Pt_3 clusters, largest contributions to the PDOS for the highest occupied states are mainly arising from the Re $5d$ -states, but also a mixing between Pt $5d$ -states and those Re $6s$ -states contributes to the overall chemical bond; Figure 5.13(c,d). For Re_1Pt_4 cluster, a strong component within the chemical bond comes from the Pt $6s$ -states with the Re $5d$, thus explaining why this cluster has its Pt atoms not forming a bond between each other; Figure 5.13(e). This behavior as well as the directionality of the bimetallic Re-Pt gas-phase clusters bonding, can be explained by considering the electron configurations of the elements involved. For Re, its ground state configuration is $[\text{Xe}]4f^{14}5d^56s^2$, and for Pt, $[\text{Xe}]4f^{14}5d^96s^1$. Rhenium has a filled $6s$ and a half-filled $5d$ subshells, while platinum has only one electron occupying its $6s$ subshell and 9 electrons in its $5d$ subshell. This particular electronic structure implies that the Re atom can share its $5d$ electrons with both $6s$ and $5d$ electrons of each Pt atom to fill its $5d$ subshell, in agreement with the observed behavior of plotted PDOS of the Re_1Pt_4 cluster.

Although so far we have focused our attention on the description of those GM structures and low-lying energy isomers at 0 K, is equally important to describe the fluxional

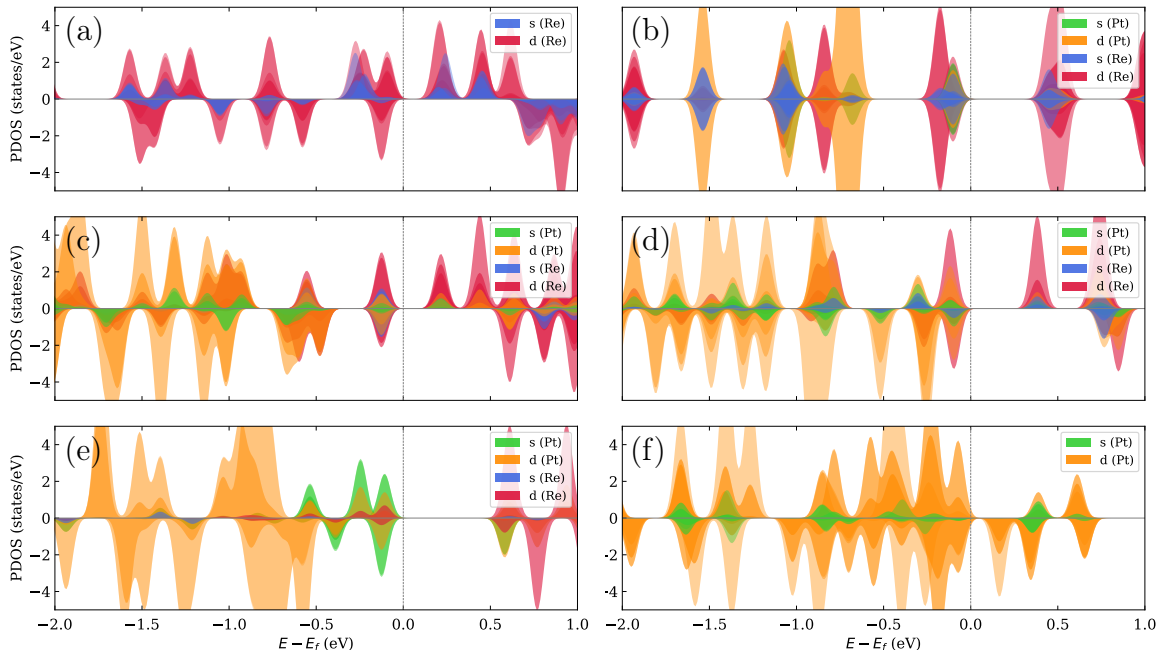


Figure 5.6: Majority spin (positive) and minority spin (negative) projected density of states (PDOS) for: (a) Re_5 , (b) Re_4Pt_1 , (c) Re_3Pt_2 , (d) Re_2Pt_3 , (e) Re_1Pt_4 , and (f) Pt_5 global minima clusters. Zero eV denotes the Fermi level.

nature of metal clusters at elevated temperatures [17, 76, 77, 114, 191, 192]. When discussing the concept of fluxionality, it implies that the lowest-energy (GM) cluster might not be the most populated structure at finite temperature, with some other isomers becoming more relevant. This is especially important because in most sub-nanometer particle applications as catalysts, temperature plays an important role in its activation and, in fact, can directly affect their structure thus modifying the (supported) nanocatalyst performance [17, 76, 77]. The approach used here allows to calculate and predict if either those GM structures of the bimetallic Re-Pt gas-phase or any of its low-energy isomers are the dominant ones as the temperature $T(K)$ increases, *i.e.* the crossing of the calculated occupation probabilities of the different cluster isomers located within the PES global exploration. To illustrate this concept, Figure 5.7 shows the calculated equilibrium occupation probabilities $P(T)$ in the temperature range of 0 - 1200 K. The harmonic approximation and similar temperature ranges (0 - 1500 K) have been applied to study the occupation probabilities of Al_N (2-65 atoms) [114], Cu_N (2-150 atoms) [191] and Pt_{13} [76] gas-phase clusters. Putative GM configurations at size 5-atom of Re_5 , Pt_5 and those bimetallic Re_4Pt_1 , Re_3Pt_2 , Re_2Pt_3 , Re_1Pt_4 gas-phase clusters are selected due to the amount of isomers found during our global optimization searches; thus helping to illustrate the concept of cluster fluxionality.

Starting with monometallic Re_5 gas-phase cluster, we can observe from Figure 5.7 (a) that at 0 K, it has the maximum $P_a(T)$ of 1.0. We also observe that the GM configuration is the most abundant structure throughout the entire 0-1200 K range. However, it is closely followed by the first energy isomer (ISO1), a square pyramid isomer. Even though there are only 0.03 eV total energy difference between these two structures, the lower symmetry of the GM (C_s) favors the $P_a(T)$ - as compared to the ISO1 (C_{4v}) - especially at low temperatures (namely below 400 K). However, ISO1 never reaches a 0.4 $P_a(T)$ within the whole temperature range. For the other two energy isomers (ISO2, ISO3), their calculated $P_a(T)$ is minimal, even at higher temperatures (<0.2). For bimetallic Re-Pt clusters, the rhenium-rich Re_4Pt_1 cluster is a very interesting case due to the wide diversity of structural isomers with a 0.29 eV total energy window; see Figure 5.7 (b). However, our calculations indicate that only two energy isomers are relevant: the GM and isomer ISO2 structures (0.12 eV higher in total energy). The planar, highly symmetrical GM structure is only relevant at temperatures below 200 K. Soon after, its calculated $P_a(T)$ decreases and a solid-solid transition at ~ 700 K occurs between this configuration and ISO2. This can be rationalized as a direct consequence of the GM structure high symmetry (C_{2v}) and low multiplicity (singlet) until the ISO2 structure (C_s) becomes the favored one. The rest of the ISO1, ISO3 - ISO5 configurations have less than 0.2 $P_a(T)$ at the high temperature range. Besides the GM configuration, there are two isomers (ISO1, ISO2) for Re_3Pt_2 located at 0.42 and 0.48 eV in total energy differences. Nevertheless, Figure 5.7 (c) indicates that only the GM configuration is present across the whole temperature range considered with a $P_a(T)$ just below 1.0. Similar results are obtained for Re_2Pt_3 where the GM is the most stable one. At this composition, only one energy isomer (ISO1) was found to be at 0.74 eV higher in total energy with basically no contributions to the overall calculated $P_a(T)$ for this system; see Figure 5.7 (d).

As mentioned previously, having 1 Re atom at its core makes the GM bimetallic Re_1Pt_4 structure quite stable, as shown in Figure 5.7 (e). While there are two relatively similar ISO1 and ISO2 configurations within 0.30 eV in total relative energy, again they never reach 0.2 $P_a(T)$, even at higher temperatures. For monometallic Pt_5 we do observe a $P_a(T)$ structural transition between the GM structure and the ISO2 configuration (0.18 eV higher in total energy) well above 1000 K. It is worth considering that both of these structures are planar, with the former having a capped, square type configuration and the latter a W-shape, as shown in Figure 5.7 (f). The isomer

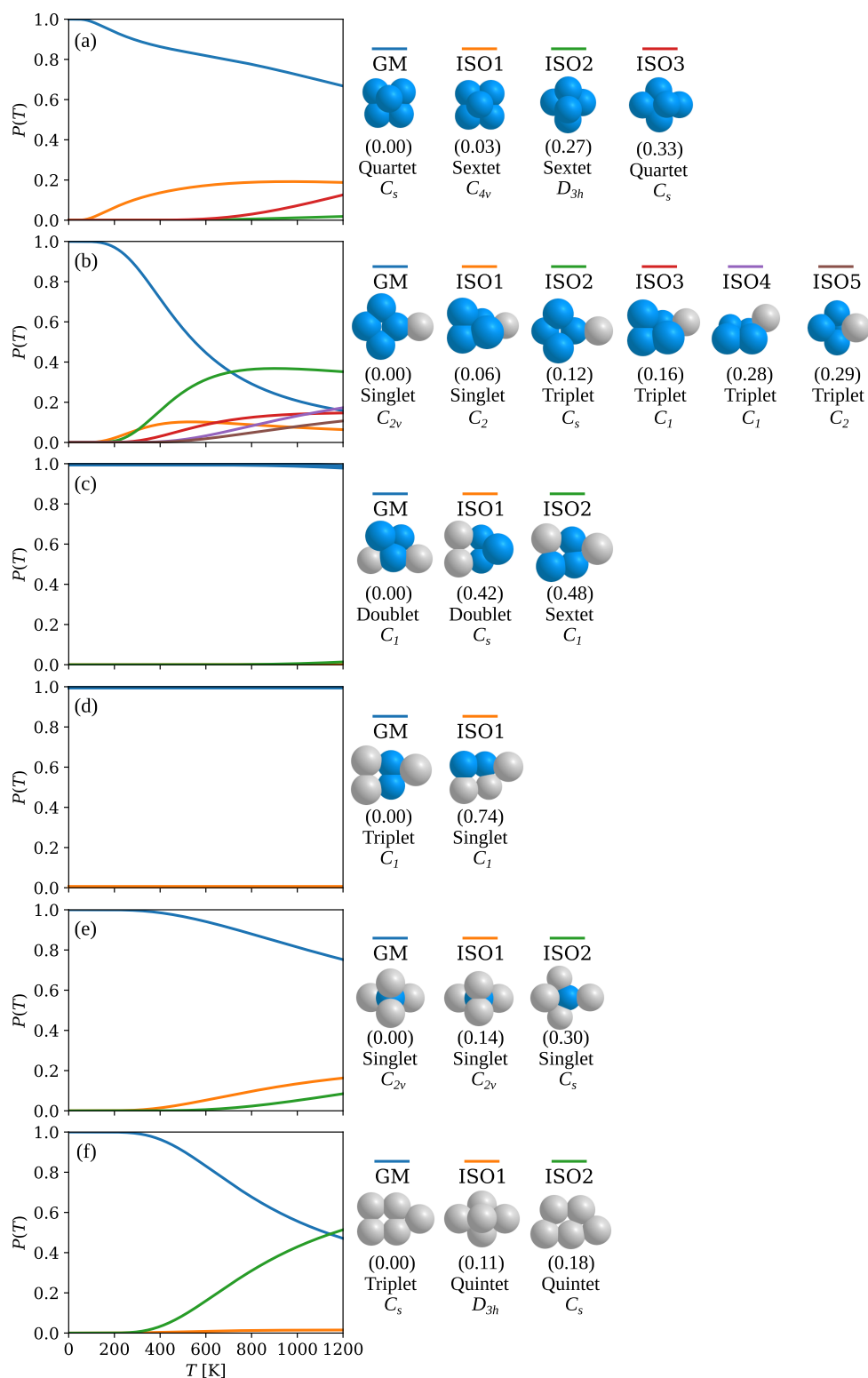


Figure 5.7: Calculated occupation probabilities, $P(T)$ as a function of temperature (in K) of both putative GM configurations and low-lying energy isomers of: monometallic (a) Re_5 , bimetallic (b) Re_4Pt_1 , (c) Re_3Pt_2 , (d) Re_2Pt_3 , (e) Re_1Pt_4 , as well as monometallic (f) Pt_5 gas-phase clusters. Total energy differences between GM structures and isomers are shown in eV, along with their corresponding spin multiplicities and symmetry point groups.

ISO1 - with its three-dimensional, trigonal bipyramidal geometry - barely contributing to the calculated $P_a(T)$ for this system. Finally, Figure 5.7 implies that as temperature increases, competition between structural gas-phase isomers can become fierce in some particular cases - namely the rhenium-rich Re_4Pt_1 cluster- and their relative fluxional $P_a(T)$ can have strong implications elucidating unseen catalytic active sites. This type of thermodynamical analysis can be helpful when trying to understand - from an atomistic perspective - reforming catalysts involving dispersed Re-Pt particles where reaction conditions can easily reach temperatures of 500 °C [165].

5.2 Re_nPt_m Clusters Supported on $\gamma\text{-Al}_2\text{O}_3$ (100)

Aluminum oxide—a ceramic compound with formula Al_2O_3 , commonly called alumina—has found widespread use in the catalysis industry, owed to its high surface area even at high temperatures [193]. It can exist in a set of polymorphic phases γ , δ , θ and α . The α phase is the most stable and it occurs naturally as the mineral corundum. The other metastable phases are known as transition aluminas and they are obtained by dehydrating aluminum hydroxides such as boehmite ($\gamma\text{-AlOOH}$), gibbsite ($\gamma\text{-Al(OH)}_3$) or bayerite ($\alpha\text{-Al(OH)}_3$), at different temperatures [194, 195]. Dehydration of boehmite yields the γ phase at around 300–500 °C. Heating $\gamma\text{-Al}_2\text{O}_3$ produces the δ phase at 700–800 °C. This δ phase transforms to $\theta\text{-Al}_2\text{O}_3$ around 900–1000 °C, which finally converts to the stable phase α at 1000–1100 °C [193, 194, 196].

Among the transition aluminas, γ -alumina has found its place as one of the most prevalent catalyst supports in the petrochemical industries [194, 195]. Transition metal clusters supported on γ -alumina—particularly those containing Pt—have been shown to be promising materials with enhanced catalytic activity towards several industrial reactions [197]. Despite its relevance, there has been a contentious debate regarding the atomic structure of γ -alumina. Some groups have described it as a defective spinel structure [196, 198], while others have argued a spinel-based structure imposes unnecessary constraints and they have proposed alternative models [185, 186, 194]. This controversy comes from the fact that γ -alumina is not a bulk material with a well-defined form, but rather an aggregate of nanoparticles with poor crystallinity [185, 186]. Therefore, no theoretical periodic model can truly describe the exact structure of this complex material.

Nonetheless, all theoretical and experimental studies agree that the oxygen atoms

in γ -alumina form a face-centered cubic (FCC) sublattice and the aluminum atoms occupy some of the tetrahedral and octahedral interstices. The precise distribution of the aluminum atoms and vacancies in the interstices of the oxygen lattice is what has been disputed for several years. The two predominant theoretical models for the structure of γ -alumina have been proposed by Digne *et al.* [185, 186, 194] and Pinto *et al.* [196]. In this work, the cell model by Digne *et al.* was chosen to represent the (100) surface of γ -alumina. The so-called Digne model is composed of 8 alumina units where the Al atoms occupy 25% of the tetrahedral sites of the FCC sublattice. This model is sufficiently large to replicate the main experimental characteristics of γ -alumina [199], while being small enough to be used for *ab initio* computational calculations. The (100) surface generated by the Digne model is characterized by the presence of penta-coordinated Al atoms (denoted Al_V) and three-coordinated O atoms (μ_3 -O) only, as can be seen in Figure 5.8. The γ -Al₂O₃ (100) surface was modelled using $2 \times 2 \times 1$ slabs separated by a vacuum of 15 Å in the vertical direction, perpendicular to the surface. The coordinates for the γ -Al₂O₃ unit cell used in the present work are provided in Appendix A.

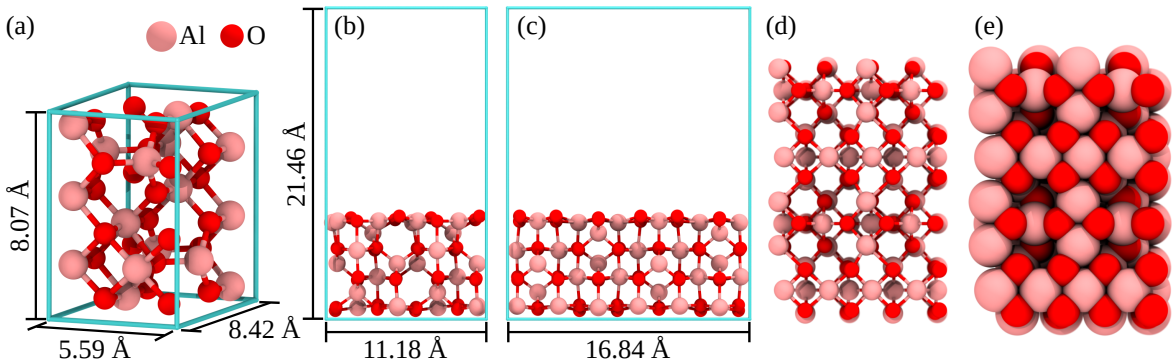


Figure 5.8: (a) Unit cell for γ -Al₂O₃ in the Digne model; (b) side view of the slab used to model the (100) surface; (c) top view of the (100) surface and (d) space-filling model of the same slab. Aluminum atoms are in pink and oxygen atoms in red.

The putative global minima (GM) structures of the Re_nPt_m clusters supported on a γ -Al₂O₃ (100) surface are depicted in Figure 5.9. The corresponding calculated properties of those clusters are summarized in Table 5.2. The same structural trends observed in the gas-phase remain in the γ -Al₂O₃-supported clusters. In all the bimetallic clusters, the Re atoms aggregate and anchor to the surface. Meanwhile, the Pt atoms tend to segregate around the Re atoms. It must also be noted that the Pt atoms in most bimetallic clusters do not bond to the oxygen atoms. These results are in line with the experiments by Bazin *et al.* where they found that Re atoms form oxidized substrates over the γ -Al₂O₃ surface and Pt atoms are dispersed above those Re atoms [12]. These

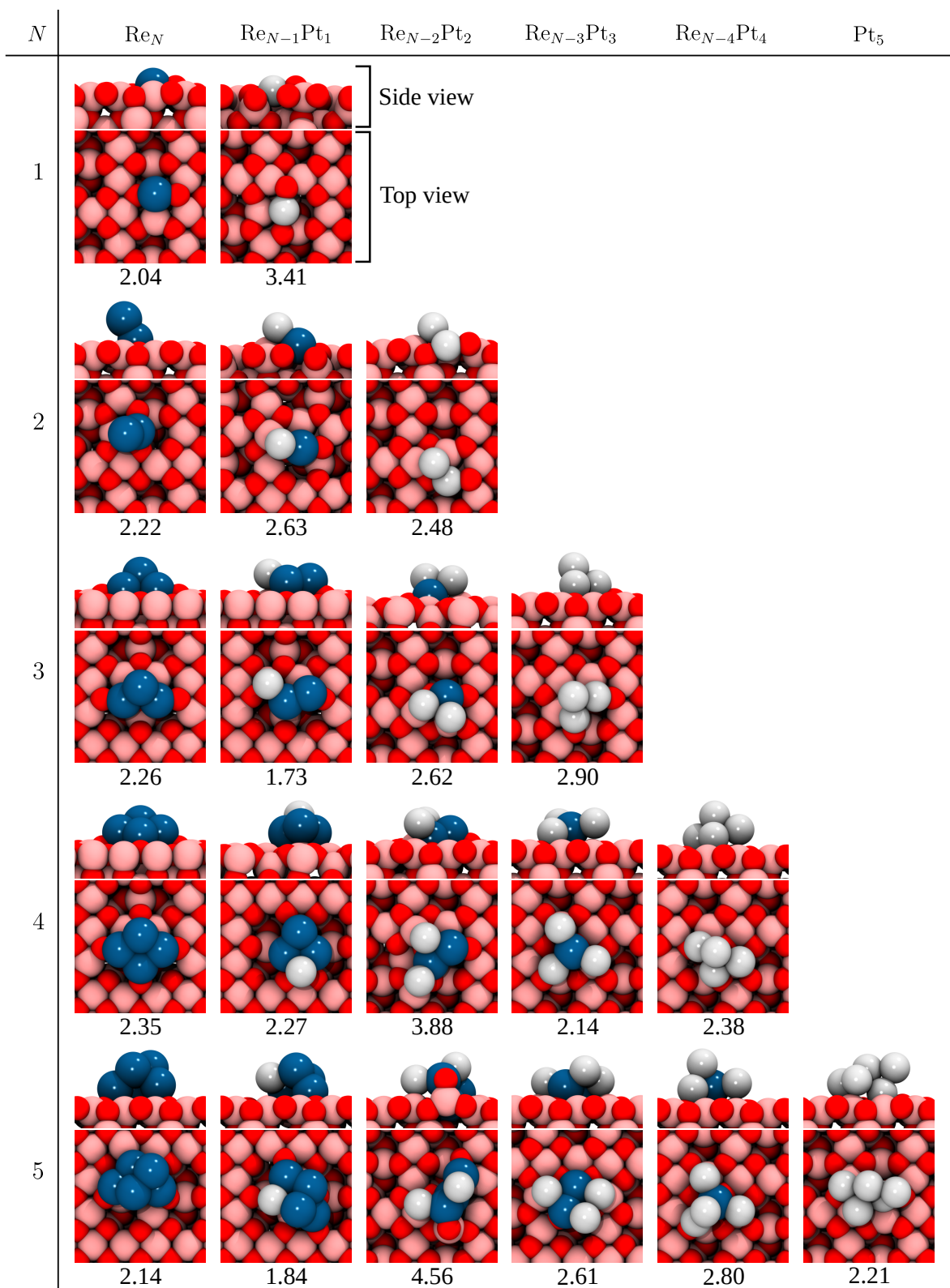


Figure 5.9: Putative global minima of single Re and Pt atoms as well as monometallic Re, Pt and bimetallic Re-Pt clusters supported on a $\gamma\text{-Al}_2\text{O}_3$ (100) surface. Re atoms are shown in blue, Pt atoms in white, Al atoms in pink, and O atoms in red. The numbers shown are the respective adsorption energy values in eV.

findings suggest that the anti-segregation tendency of Re atoms in Re-Pt alloys [189, 200] holds true even for supported subnanometer clusters. Similar to their gas-phase counterparts, Re clusters supported on γ -Al₂O₃ have the shortest average metal-metal bond lengths compared to the bimetallic Re-Pt and the monometallic Pt clusters of the same size. The metal-oxygen bonds are consistently shorter than the metal-aluminum bonds in all clusters sizes and compositions. Among all the clusters studied here, Re₂Pt₂ and Re₃Pt₂ show the strongest binding to the γ -Al₂O₃ substrate, as can be seen from Figure 5.10. The adsorption energy value for Re₃Pt₂ (4.56 eV) is almost an eV higher than that of Re₂Pt₂. They also present the most favorable mixing tendencies compared to other bimetallic clusters of the same sizes. These properties of Re₃Pt₂ indicate that it is the most structurally stable γ -Al₂O₃-supported cluster in the range of sizes considered here.

Table 5.2: Spin multiplicity (M), adsorption energy (E_{ads} , in eV), mixing energy per atom (Δ/N , in eV), net charge (in e^-), and average bond lengths (in Å) for the Re_{*n*}Pt_{*m*}/ γ -Al₂O₃ (100) GM clusters.

Cluster	M	E_{ads}	Δ/N	Net charge	Re-Re	Re-Pt	Pt-Pt	Re-Al	Re-O	Pt-Al	Pt-O
Re ₁	4	2.04	0.00	-0.14	-	-	-	2.43	2.02	-	-
Pt ₁	1	3.41	0.00	+0.29	-	-	-	-	-	2.37	2.05
Re ₂	3	2.22	0.00	-0.13	2.11	-	-	2.52	2.07	-	-
Re ₁ Pt ₁	4	2.63	-0.24	+0.26	-	2.44	-	2.56	1.99	2.46	-
Pt ₂	1	2.48	0.00	+0.37	-	-	2.50	-	-	2.53	2.01
Re ₃	2	2.26	0.00	-0.29	2.27	-	-	2.42	2.02	-	-
Re ₂ Pt ₁	1	1.73	0.04	+0.12	2.14	2.36	-	2.60	2.03	2.69	-
Re ₁ Pt ₂	4	2.62	-0.39	+0.30	-	2.47	2.61	2.43	2.00	2.50	-
Pt ₃	3	2.90	0.00	+0.30	-	-	2.54	-	-	2.53	2.08
Re ₄	1	2.35	0.00	-0.23	2.31	-	-	2.73	2.04	-	-
Re ₃ Pt ₁	2	2.27	-0.01	0.00	2.31	2.51	-	2.75	2.15	-	-
Re ₂ Pt ₂	1	3.88	-0.51	+0.27	2.19	2.36	-	2.59	2.02	2.47	-
Re ₁ Pt ₃	2	2.14	-0.39	+0.28	-	2.30	-	-	1.99	2.54	2.19
Pt ₄	3	2.38	0.00	+0.32	-	-	2.55	-	-	2.60	2.15
Re ₅	4	2.14	0.00	-0.18	2.42	-	-	2.75	2.18	-	-
Re ₄ Pt ₁	3	1.82	-0.09	-0.11	2.35	2.45	-	2.57	2.17	-	-
Re ₃ Pt ₂	2	4.56	-0.78	+0.38	2.30	2.40	-	2.64	1.96	2.60	-
Re ₂ Pt ₃	1	2.61	-0.48	+0.17	2.22	2.39	2.62	-	2.10	2.57	-
Re ₁ Pt ₄	2	2.80	-0.62	+0.25	-	2.35	2.55	-	2.17	2.56	2.10
Pt ₅	1	2.21	0.00	+0.42	-	-	2.57	-	-	2.56	2.18

There have been numerous theoretical studies of Pt clusters supported on γ -Al₂O₃ in recent years [7, 113, 201–203]. However, none of those works have dealt with the global optimization of the combined cluster and substrate systems. The putative global minima of these Pt_{*n*}/ γ -Al₂O₃ clusters—except for Pt₁ and Pt₅—differ from those reported

in the literature [7, 113, 201] in either the geometry, the adsorption configuration, or both. These structural discrepancies can be attributed to the unbiased global exploration of the PES of the combined system, which allows us to find structures that are not accessible by simple local relaxations. The preferred adsorption site of the single Pt atom is in a hollow site of the surface, which is consistent with the results presented in previous works by Aaron-Deskins *et al.* [197] and Mei *et al.* [201]. In this site, the Pt atom binds strongly to the oxide surface with an adsorption energy (E_{ads}) of 3.41 eV, which is slightly smaller than the value of 3.50 eV reported in those works. This difference might be caused by the use of different XC functionals and basis sets. Nevertheless, the interaction of a single Pt atom with the pristine $\gamma\text{-Al}_2\text{O}_3$ (100) is stronger than that of most other clusters considered in this work (only Re_2Pt_2 and Re_3Pt_2 bind more firmly to the substrate). The strong interaction of single Pt atoms with $\gamma\text{-Al}_2\text{O}_3$ has been experimentally shown to hinder the Pt sintering process, particularly at low Pt loadings [201]. In contrast to the single Pt atom, the monometallic Pt_n ($n \geq 2$) clusters do not bond to the $\gamma\text{-Al}_2\text{O}_3$ surface as strongly, with lower E_{ads} values ranging from 2.21 eV for Pt_5 to 2.90 eV for Pt_3 . The Pt dimer adsorbs on $\gamma\text{-Al}_2\text{O}_3$ surface with an atom located in a hollow site and the other on top of the first Pt atom, bound to a pair of Al_V atoms in a bridge position. Pt_3 forms an isosceles triangle with each atom of the base in a O-Pt- Al_V bridge configuration and the third atom unbound to the surface. Like its gas-phase analogue, the most stable geometry of $\text{Pt}_4/\gamma\text{-Al}_2\text{O}_3$ is a bent-rhombus. This rhombus is attached to the surface by two Pt atoms bound to a pair of O atoms and the third one bound to an Al_V atom. The structure of the $\text{Pt}_5/\gamma\text{-Al}_2\text{O}_3$ GM cluster is three-dimensional, as opposed to the planar structure of the GM gas-phase Pt_5 cluster [200].

Monometallic rhenium clusters supported on $\gamma\text{-Al}_2\text{O}_3$ follow similar structural trends compared to their platinum counterparts. However, the adsorption energies of rhenium clusters are lower than those of platinum clusters of the same size. The weaker interaction of those monometallic Re clusters with the substrate suggests they are less stable and might have a higher tendency to coalesce than monometallic Pt clusters. However, the adsorption energies *per se* are not enough to predict the coalescence of clusters and a better descriptor—such as the nucleation energy—is required for this purpose. Understanding the nucleation and growth of supported cluster is a crucial step in the design of better nanocatalysts. Owing to their higher number of active sites compared to the number of atoms, smaller clusters exhibit higher reactivity compared to larger ones. Using highly dispersed small clusters and atoms also reduces the required ma-

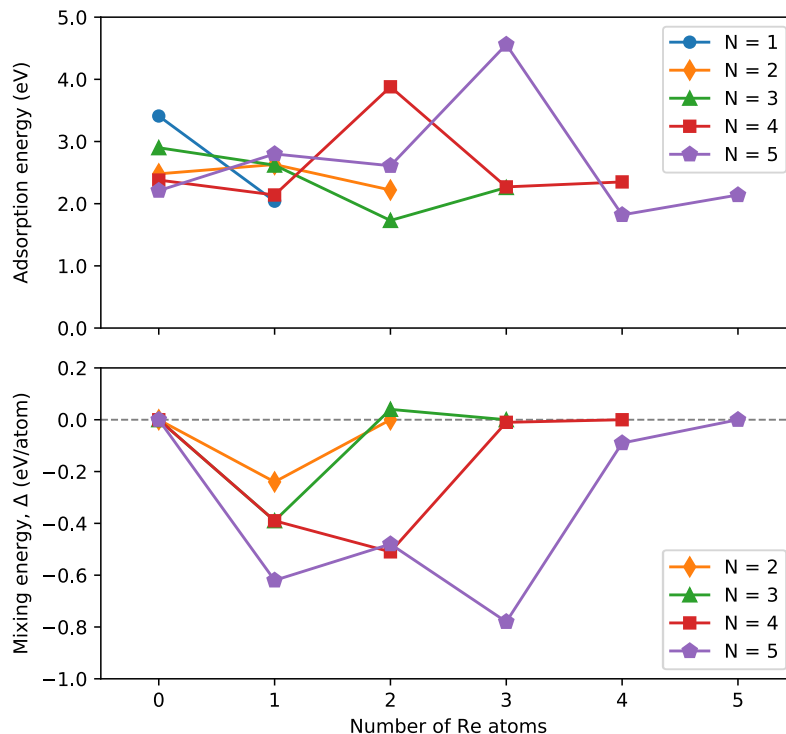


Figure 5.10: Calculated adsorption energy (top) and mixing energy (bottom) values for the Re_nPt_m clusters supported on $\gamma\text{-Al}_2\text{O}_3(100)$.

material. Thus, the coalescence of small clusters to form large nanoparticles leads to less efficient catalysts. Therefore, finding mechanisms to hinder the sintering of atoms and clusters is highly desired. One of such mechanisms is through alloying. By combining the appropriate metals we can create more stable clusters. For the particular case of Re-Pt clusters supported on $\gamma\text{-Al}_2\text{O}_3$, it has been shown that alloying Re with Pt leads to clusters with higher stability [12]. The nucleation pathways of Re and Pt clusters were computed by means of the nucleation energy. The most favorable nucleation pathways starting from the Re and Pt single atoms are shown in Fig. 5.11. The coalescence of Pt atoms into Pt clusters is energetically unfavorable.

A Bader charge analysis was performed to understand the bonding mechanisms of the clusters and to substrate. This analysis indicates that all monometallic Re clusters transfer electrons to the $\gamma\text{-Al}_2\text{O}_3$ surface, as can be seen in Table 5.2. In contrast—in the case of monometallic Pt clusters—the charge transfer is from the surface to the clusters. The same behavior is also observed in most bimetallic Re-Pt clusters analyzed here, except in Re_3Pt_1 and Re_4Pt_1 . A closer inspection of the charge distribution in those bimetallic Re-Pt clusters revealed that Re atoms tend to oxidize, which is con-

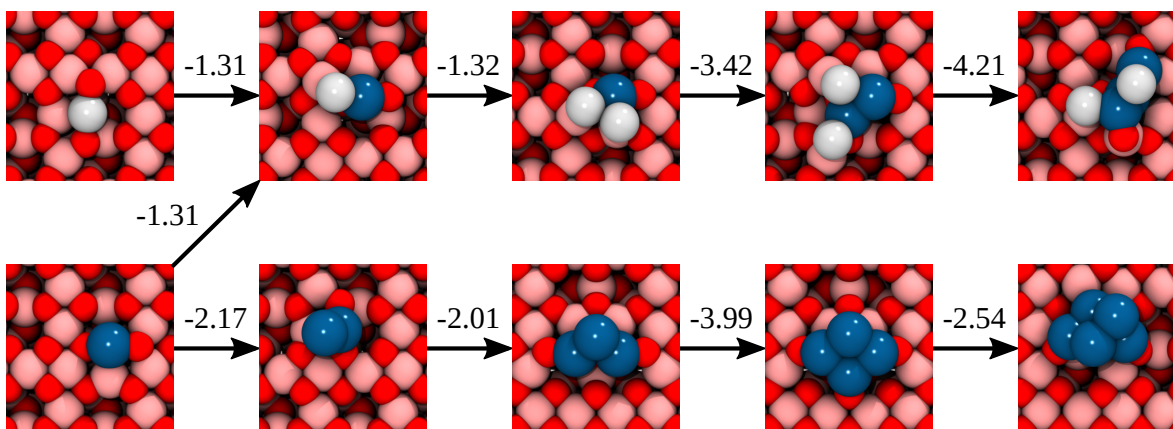


Figure 5.11: The two most favorable nucleation pathways for Re-Pt/ γ -Al₂O₃ clusters, starting from single Pt and Re atoms.

sistent with previous experimental works [12]. The calculated charge distributions for the γ -Al₂O₃-supported bimetallic Re-Pt clusters are shown in Figure 5.12.

In addition to the charge analysis, calculating the PDOS of these systems can also help us elucidate the bonding mechanisms between the metal clusters and the substrate. Figure 5.13 shows the Re, Pt, O and Al orbital PDOS for all the Re_nPt_m pentamers supported on γ -Al₂O₃ (100). The main contribution of the Re atoms to the PDOS around the Fermi level comes from the 5*d*-states, which spread across the energy range shown. In the case of the Pt atoms, the main contribution also comes from their 5*d*-states, but unlike the Re 5*d*-states they concentrate towards the Fermi level. The contribution to the PDOS from the 6*s*-states is negligible compared to that of the 5*d*-

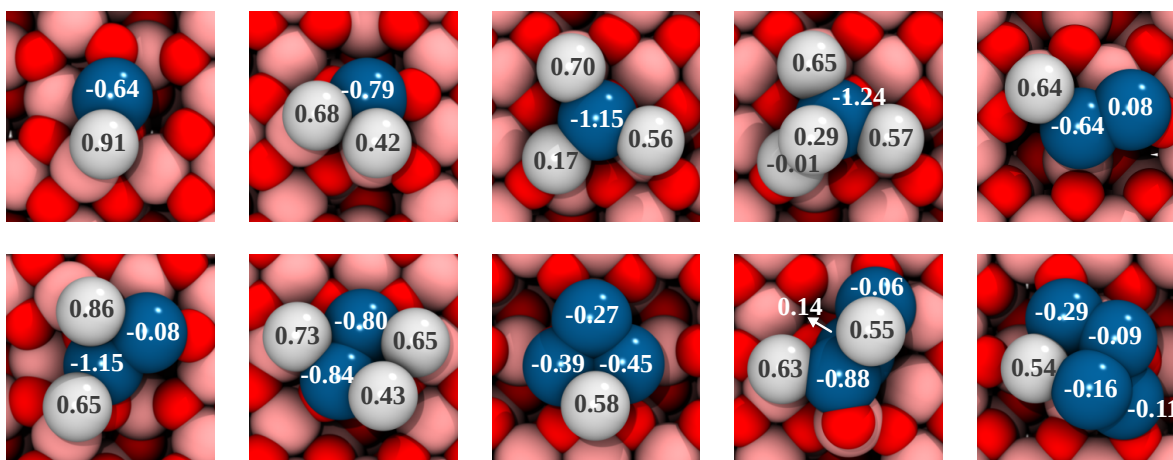


Figure 5.12: Charge distribution in bimetallic Re-Pt/ γ -Al₂O₃ (100) GM clusters. A negative sign indicates a gain of electronic charge.

states for both Pt and Re. In all the bimetallic clusters, there is barely any overlap between the Pt 5d-states and the deep O 2p-states. Lastly, the PDOS of the Al atoms extends far from the Fermi level which suggest no bonds form between the cluster and the surface Al atoms. These results are in good agreement with experimental works by Bazin *et al*, who found that Re forms an oxidized substrate linked to the γ -Al₂O₃ surface and the Pt atoms sit on top of the Re atoms without forming direct bonds with the support [12].

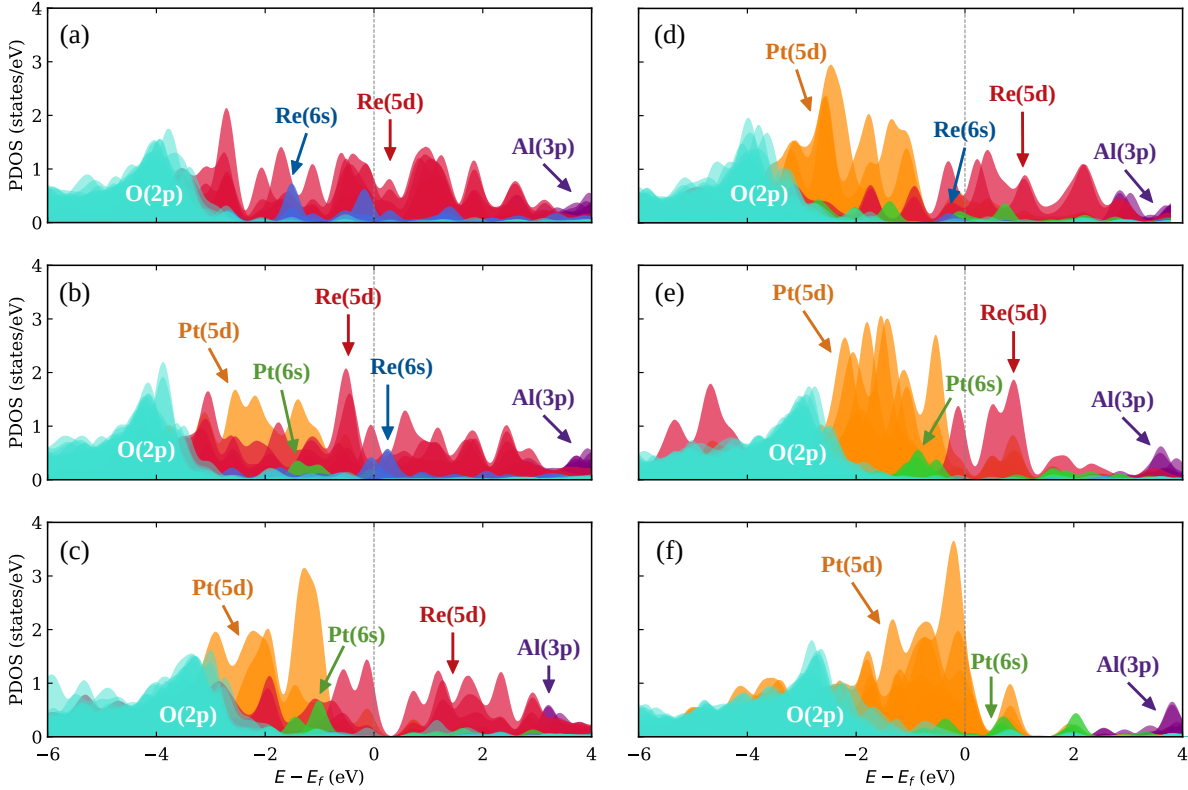


Figure 5.13: Projected density of states (PDOS) for Re-Pt clusters supported on γ -Al₂O₃(100): (a) Re₅, (b) Re₄Pt₁, (c) Re₃Pt₂, (d) Re₂Pt₃, (e) Re₁Pt₄, and (f) Pt₅. Atomic orbitals are displayed in different colors: red for Re 5d, dark blue for Re 6s, orange for Pt 5d, green for Pt 6s, cyan for O 2p and purple for Al 3p. Zero eV denotes the Fermi level.

Chapter 6

Applications of Machine Learning to the Study of Adsorption Processes

Although DFT based calculations are the main workhorse methods currently used in computational materials science, to bring about accurate and predictive simulations is still quite challenging. This is particularly true for materials with complex structures and hundreds or thousands of atoms. On top of the large number of atoms involved, performing extensive PES explorations of such systems—especially when using first-principles global optimization schemes or *ab initio* molecular dynamics (AIMD)—poses an additional challenge since those calculations must be repeated thousands of times. Since performing predictive *in silico* experiments using highly precise methodologies is still a prohibitive task for most extended systems of interest, many computational studies are limited to the analysis of their electronic structure at equilibrium, while using the harmonic approximation for mechanical properties. Fortunately, overcoming some of these limitations is now currently possible by using machine learned molecular force fields (ML-FFs). Machine learning (ML) algorithms can improve automatically through experience and by the use of data. They build models based on sample data—known as *training data*—to make predictions or decisions without being explicitly programmed to do so. In the case of ML-FFs, the training data are the geometric configurations of a particular system together with their respective potential energy values, interatomic forces or, in the case of periodic systems, stresses.

In recent years, several ML-FFs methods have been developed, which allow us to perform calculations with the same accuracy of *ab initio* calculations, but at a fraction of their computational cost [17, 53–77]. One of those methods is the symmetric gradient-domain machine learning (sGDML) approach. This highly accurate and data-efficient

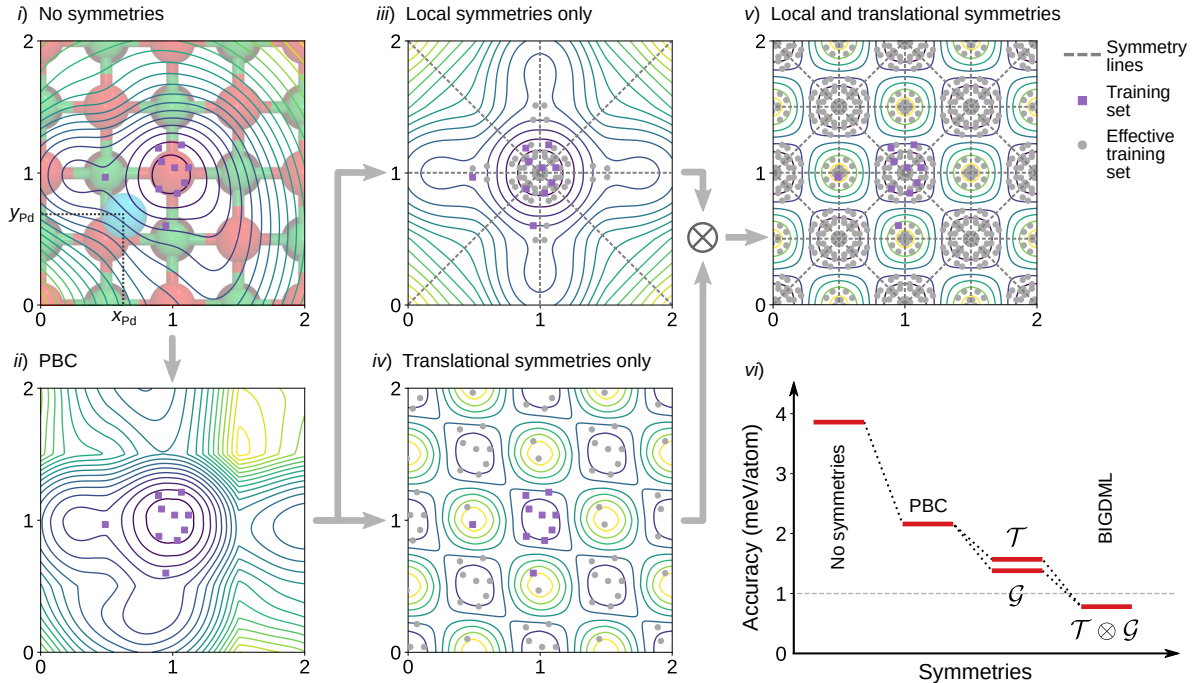


Figure 6.1: Schematic representation of the use of symmetries by sGDML to reconstruct a periodic PES from a limited number of data samples. The axis in the PES are the x and y coordinates of the Pd atom in units of the lattice constant of MgO. Models: *i*) Pure GDML, *ii*) GDML+PBC, *iii*) sGDML+PBC+ \mathcal{G} , *iv*) sGDML+PBC+ \mathcal{T} , and *v*) BIGDML. Panel *vi*) displays the incremental accuracy upon addition of each symmetry for the Pd₁/MgO (100) system.

method can reconstruct force fields from a limited number of geometry samples. When these samples are extracted from *ab initio* molecular dynamics (AIMD) trajectories, it can faithfully reproduce the details of the respective Born-Oppenheimer potential energy surfaces [54–60]. In contrast with other ML approaches which fit PES models, sGDML directly learns the functional relationship between interatomic forces and atomic coordinates, hence the name *gradient-domain*. By doing so, it avoids the need to use noisy numerical gradient operators and allows us to construct energy-conserving fields. It also incorporated all relevant physical symmetries for a particular system, such as rigid space group symmetries and dynamic non-rigid (fluxional) symmetries. Figure 6.1 shows how including the physical symmetries of a particular system allows sGDML to reconstruct its PES from a handful of training samples, even when they only contain information of a small region of it. Combining those two components allows sGDML to achieve high accuracy with only a limited number of training samples. To construct a ML-FF from a given training dataset, sGDML starts by encoding the molecular geometries using a descriptor. After transforming the atomic positions from

the real space to the descriptor space, then it finds all the equivalent permutations of the atoms. Finally, it trains the sGDML model using the provided training dataset. The similarity between a new, unknown geometry and those found in the training set is measured and then used to make a prediction of its potential energy and interatomic forces. In order to assess the accuracy of the sGDML model, the predictions given for a set of unknown geometries (called test dataset) will be compared to their real values. The difference between the estimated values and the real values provide a quantitative measurement of the accuracy of a given model. In principle, increasing the size of the training dataset will increase the accuracy of the ML model. As a part of this work, I co-developed an extension of sGDML which incorporates periodic boundary conditions (PBCs). This extension is called BIGDML—where BI stands for *Bravais-inspired*—and it expands the capabilities of sGDML to work with extended systems such as crystals, 2D materials or surfaces [204]. The information provided here is only a brief summary of the sGDML method, as well as on the BIGDML implementation. Further details can be found in the literature (see Refs. [54, 55, 60, 204]).

While sGDML has shown great potential for the study of organic molecules, its applicability to metal clusters—at least in its current state—is somewhat limited. One of the reasons for this limitation is the inclusion of physical symmetries. In the case of small organic molecules, the relevant symmetries are usually the point group symmetries, as well as the dynamic symmetries of functional groups such as hydroxyl, or methyl. Thus, the number of symmetry elements for those molecules is at most a few dozens. However, in the case of highly fluxional metal clusters, the number of relevant symmetries is not limited to their point group symmetries. It has been shown that the structure of transition metal clusters can fluctuate between several isomers with distinct geometries [36, 76, 200]. Therefore, to fully capture the fluxional nature of these systems, it is necessary to consider all the different, but physically equivalent ways to permute their atoms which leave the structures unaltered. Thus, the number of symmetry elements is $N!$ for a monometallic cluster with N atoms, and $N!M!$ for a bimetallic cluster of size $N + M$ atoms. As a result, the number of relevant physical symmetries for metal clusters quickly becomes insurmountable as they grow in size. In the case of supported clusters, this problem is even more challenging since we must also account for the symmetries of the substrate. Given these limitations, we will focus our attention to a simpler case: single metal atoms. While these systems might seem overly simple, they are relevant in the context of single-atom catalysts (SACs). It has been shown that SACs can offer superior catalytic performance compared to

clusters and nanoparticles [205–207]. These heterogeneous catalysts consist of isolated metal atoms supported on a range of substrates, such as metal oxides, metal surfaces or carbon-based material. Here we will use single Pt and Pd atoms supported on pristine magnesium oxide (100) substrates to showcase the capabilities of BIGDML to model surfaces. Magnesium oxide (MgO) has a rock-salt structure and its (100) facet is a flat surface with Mg and O atoms in a checkered pattern. The supercell used to model this surface consists of a 2×2 slab of MgO (100) with 3 layers with a single metal atom (either Pd or Pt) deposited on the surface, as can be seen in Figure 6.2. The calculations were performed in Quantum Espresso [103, 104] using the Perdew-Burke-Ernzerhof (PBE) [85] exchange-correlation functional and plane-wave basis sets with scalar-relativistic-corrected ultrasoft pseudopotentials. Energy cutoffs of 50 Ry were employed for the basis sets. In all cases, a uniform $3 \times 3 \times 1$ Monkhorst-Pack grid of k -points was used to integrate over the Brillouin zone. To generate the databases, we ran AIMD at 1000 K with time steps of 1.0 fs during 10,000 steps. A BIGDML model was training using 200 training samples.

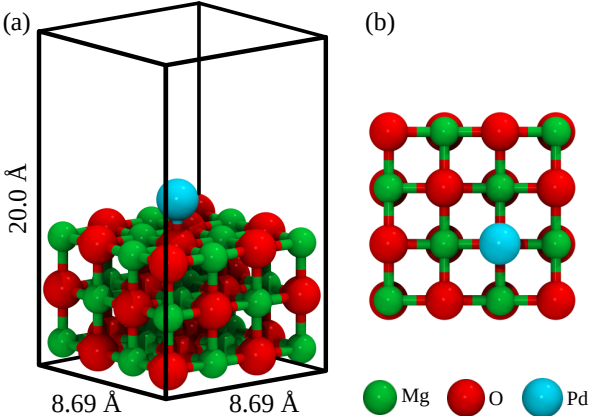


Figure 6.2: (a) Slab used to model the Pd_1/MgO (100) surface and (b) its top view. Magnesium atoms are in green, oxygen atoms in red and palladium atoms in cyan.

The full symmetry group for M_1/MgO ($\text{M}=\text{Pd},\text{Pt}$) is $T_{2 \times 2}^{(2)} \otimes C_{4v}$, which has 64 elements. In this context, the metal atom is chemisorbed at an oxygen site and the lowest energetic barrier that the Pd atom experiences is of 0.45 eV for Pd and 0.97 eV for Pt. In Figure 6.3 we show the minimum-energy path (MEP) of a Pd atom displacing from one minimum to another on the MgO surface computed by the nudged elastic band (NEB) method. It must be noted that the adatoms never crossed this barrier during the MD simulation used to generate the reference dataset. Hence, even though the model did *not* have information regarding the saddle point, the energetic barrier for Pd_1/MgO was

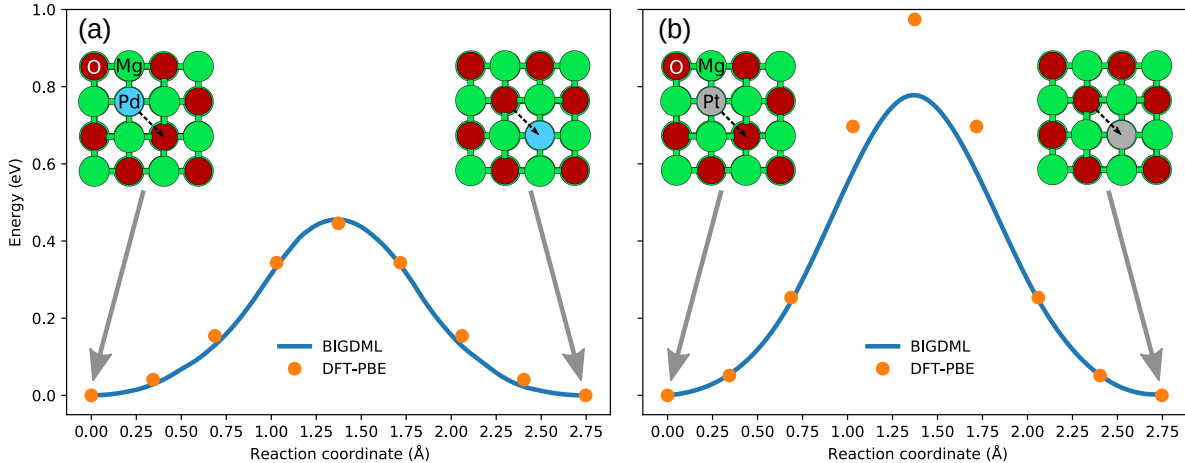


Figure 6.3: Comparison of the minimum-energy path between neighbouring oxygen-sites for (a) Pd and (b) Pt single atoms supported on MgO (100) surfaces using BIGDML (continuous line) and the reference method, DFT/PBE (circles).

nevertheless correctly modeled by BIGDML by incorporating translational and Bravais symmetries. However, the MEP for Pt_1/MgO was only accurately reproduced near the minima and its height was underestimated by about ~ 0.20 eV. This difference can be attributed to the higher value of the MEP for Pt_1 (0.97 eV) compared to that of Pd_1 (0.45 eV).

While calculating the MEP provides a valuable assessment of the accuracy of ML models, it hides the true capabilities of ML-FFs. The full potential of BIGDML lies on its ability to be used to calculate dynamic properties which require long-timescale simulations, such as the diffusivity of atoms. However, both Pd_1 and Pt_1 must overcome relatively high energy barriers to diffuse on the MgO (100). For this reason, we will focus our attention on an alternative problem: the diffusion of H in bulk Pd. Although the main topic of the present work is the interaction of transition metal clusters with small molecules, the motivation to study H in Pd remains the same: the research and development of renewable fuels. Hydrogen has become a promising alternative to fossil fuels as a cleaner energy source. Nevertheless, finding a safe, economical and high-energy-density hydrogen storage medium remains a challenge [208]. One of the proposed methods is to store hydrogen in interstitial sites of the crystal lattices of bulk metals [208–210]. Among these metals, palladium has been widely researched as a candidate, since it can absorb large quantities of hydrogen in a reversible manner [209]. Characterizing the diffusion of hydrogen in the crystal lattices at different temperatures is crucial to assess their performance as storage materials. In this case,

we used a supercell of $3 \times 3 \times 3$ with 32 Pd atoms and a single hydrogen atom. The calculations were performed at DFT/PBE level of theory using the Quantum Espresso software. The database was generated by running AIMD at 1000 K. We used time steps of 1.0 fs and a total dynamics of 6 ps. Monkhorst-Pack grids of $3 \times 3 \times 3$ k -points were used to integrate over the Brillouin zone for all materials. After training a BIGDML model using 100 training samples, we ran simulations at various temperatures from 300 K to 1000 K. We run both Born-Oppenheimer molecular dynamics (BOMD) and path-integral molecular dynamics (PIMD), which incorporate nuclear quantum effects (NQEs), using the interface of BIGDML with the i-PI simulation package [211]. The inclusion of NQEs is necessary to accurately describe the dynamics of light atoms such as H [209]. In each case, we employed a time step of 2.0 fs during 2,000,000 steps, for a total simulation time of 4 ns. Using this data we were able to compute the H diffusivity as a function of the temperature.

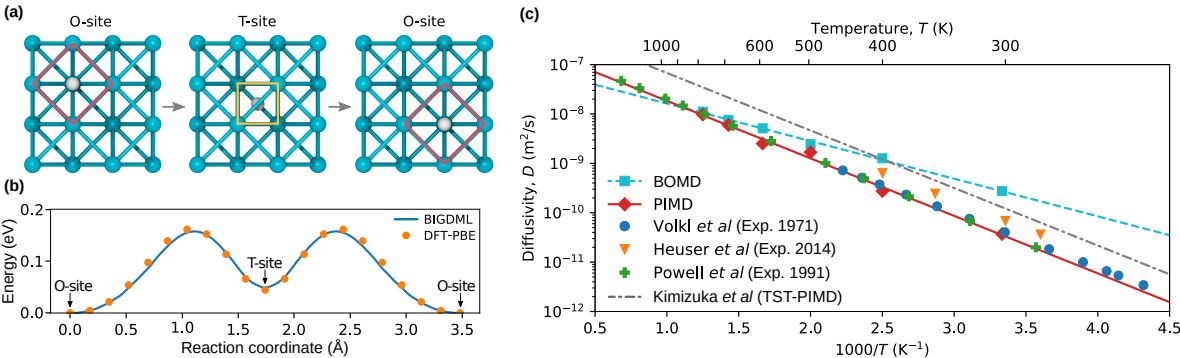


Figure 6.4: (a) Minima of the trajectory used to calculate the minimum-energy path (MEP) for the diffusion of H in FCC Pd. (b) MEP as calculated using BIGDML (continuous line) and DFT-PBE (circles) between adjacent O- and T-sites. (c) Diffusivity of H in bulk Pd as a function of the temperature. The cyan squares and red diamonds represent the values calculated running BOMD and PIMD using the BIGDML model, respectively. The lines are the Arrhenius fit to the data from MD@BIGDML (cyan, dashed), PIMD@BIGDML (red, solid) and TST-PIMD by Kimizuka *et al.* (gray, dash-dotted) [209]. Experimental data was taken from Refs. [212] (blue circles), [213] (orange triangles) and [214] (green crosses).

From the generated classical (BOMD) and quantum (PIMD) trajectories we have estimated the diffusivity of the hydrogen atom as a function of the temperature, which are shown in Figure 6.4-C along with transition-state theory (TST) results and experimental data. Usually, this quantity is estimated by using transition rate theory which only considers the energetics of the system (energy barrier and relative energy between adjacent states) [209]. A more robust methodology is to directly compute the diffusivity from the molecular dynamics results using the mean-square displacement analysis [215],

an option which MLFFs make feasible due to the long-time simulations required while keeping *ab initio* accuracy. From these results we observe an Arrhenius temperature dependence for the diffusivity ($D(T) = D_0 e^{-Q/kT}$) in both the BOMD and the PIMD cases, which is expected in the range of temperatures considered. While the TST-PIMD results by Kimizuka *et al.* [209] ($D_0 = 9.90 \times 10^{-7}$ m²/s, $Q = 0.23$ eV) accurately reproduce the experimental activation barrier Q for H in Pd, they considerably overestimate the value of the pre-exponential factor D_0 . In our case, the diffusivity of H in Pd at lower temperatures is overestimated by BOMD ($D_0 = 0.95 \times 10^{-7}$ m²/s, $Q = 0.151$ eV), but it is close to the reported values at high temperatures. Meanwhile, both the activation barrier ($Q = 0.231$ eV) and the pre-exponential factor ($D_0 = 2.70 \times 10^{-7}$ m²/s) calculated using BIGDML@PIMD are in excellent agreement with the experimental data at all temperatures.

The results presented in this chapter showcase the advantages of using ML-FFs to accelerate the study of complex materials. By performing a single AIMD simulation and training a BIGDML model using only a fraction of the generated data, it was possible to run multiple MD simulations at lower temperatures and even include nuclear quantum effects. If these additional simulations were to be run using full DFT calculations, they would require at least two orders of magnitude more computation time. Thanks to the use of physical symmetries, BIGDML is capable of achieving this feat using only 100s of data samples extracted from the original AIMD simulation. The use of BIGDML to analyze other periodic systems was also explored, but only those relevant to the topic of this thesis were presented here. A full description of BIGDML and its applications can be found in Ref. [204].

Chapter 7

Conclusions and outlook

In the first part of the present work, a systematic study on the adsorption of CO_2 on $\text{Cu}_{4-x}\text{Pt}_x$, and H_2 on $\text{Cu}_{4-x}\text{Au}_x$ and $\text{Cu}_{4-x}\text{Pt}_x$ gas-phase clusters was carried out. In order to locate the most stable structures, the PES of each cluster composition was explored using an unbiased Monte Carlo Basin Hopping algorithm. For the monometallic Cu_4 and Au_4 as well as the bimetallic $\text{Cu}_{4-x}\text{Au}_x$ clusters, the most stable geometries were all planar. As for Pt_4 and $\text{Cu}_{4-x}\text{Pt}_x$ clusters, the lowest-energy structures were either tetrahedra or quasi-planar bent rhombi. In general, $\text{Cu}_{4-x}\text{Pt}_x$ showed higher binding energies than $\text{Cu}_{4-x}\text{Au}_x$ clusters, which indicates that Cu atoms bind more strongly to Pt atoms than to Au atoms.

After finding the lowest energy geometries, the analysis of the adsorption process was performed on the putative global minima of each composition. All non-equivalent adsorption sites were explored for each cluster composition. In the case of molecular adsorption of H_2 on $\text{Cu}_{4-x}\text{Au}_x$ and $\text{Cu}_{4-x}\text{Pt}_x$ clusters, two adsorption modes were observed: a dissociative mode where the H-H bond was cleaved; and a non-dissociative mode. The dissociative adsorption occurs on Au_4 and on all the clusters which contain Pt atoms. On the rest of the clusters, the adsorption was non-dissociative and the preferred adsorption site for the H_2 molecule was on-top of the Cu atom. In general, the $\text{Cu}_{4-x}\text{Pt}_x$ clusters exhibit larger adsorption energy values compared to the $\text{Cu}_{4-x}\text{Au}_x$ clusters, and show a tendency to increase with number of Pt atoms. These results suggest that Cu-Pt clusters are better candidates than Cu-Au clusters for catalytic reactions that involve hydrogen activation.

From the study of the molecular adsorption of CO_2 on $\text{Cu}_{4-x}\text{Pt}_x$ clusters, it was found that the strongest interaction between the molecule and the cluster occurred

on the Cu_2Pt_2 cluster. This composition also had the best mixing tendency among the bimetallic $\text{Cu}_{4-x}\text{Pt}_x$ clusters, as suggested by its favorable mixing energy value. These results suggest that the Cu_2Pt_2 cluster is an excellent candidate to capture CO_2 molecules; however, further research is needed to assess its performance in a catalytic process. In all cases, the CO_2 molecule bends upon adsorption and this correlates with charge transfer to the LUMO frontier orbital of the molecule. The interaction of the CO_2 with the clusters causes a structural conversion in the Cu_3Pt_1 and Pt_x clusters, which can be explained due to the relatively small activation energies between the global minimum and the first low-lying cluster geometries. A more suitable composition for catalysis is Cu_3Pt_1 , which has stronger binding energy than Cu_2Pt_2 and a similar mixing energy value. Cu_3Pt_1 has a lower CO_2 -adsorption energy compared to Cu_2Pt_2 which might be desirable for optimal catalytic performance.

In the second part of this work, a thorough global exploration of the potential energy surface of subnanometer gas-phase and $\gamma\text{-Al}_2\text{O}_3$ -supported Re_nPt_m clusters was performed. We found numerous morphologies for the diverse compositions and sizes. For clusters up to four atoms and for all the monometallic platinum clusters, the most stable geometries were planar or quasi-planar. In contrast with our study on $\text{Cu}_{4-x}\text{Pt}_x$ gas-phase clusters, the putative global minima found for Pt_4 is a bent rhombus and the first isomer is the tetrahedron. This disagreement might be attributed to the use of plane-wave basis sets for the DFT calculations, instead of Gaussian-type orbitals. In the case of Re clusters, there was a transition to three-dimensional geometries for those with five or more atoms. In the bimetallic clusters, we found that Re atoms tend to aggregate in the center of the clusters, while the Pt atoms segregate and tend to not form bonds between themselves. The stability of the clusters was analysed by means of different energy descriptors, which predict that the most stable structure overall is the octahedral Re_6 cluster. Doping pure Pt clusters with a single Re atom is enough to add more stability to the clusters since it increases their binding energy significantly and widens their HOMO-LUMO gap values. This type of clusters also show the best mixing tendency among the bimetallic clusters. An analysis of the thermal behavior of those Re-Pt with five atoms was carried out by means of the harmonic superposition approximation. While the harmonic approximation neglects the anharmonicity of the PES and thus can only be accurate at low temperatures, it still provides a qualitative insight into the relative stability of the low-energy isomers. Overall, this analysis suggested that is more probable to find cluster geometries with lower symmetries, which tend to be more abundant at high temperatures compared to highly symmetric clus-

ters. In most cases, however, the structures with the highest occupation probabilities throughout the temperature range considered were those with the lowest total energy.

The study of the Re_nPt_m adsorbed on the $\gamma\text{-Al}_2\text{O}_3$ (100) revealed that the same structural trends found in the gas-phase can be observed for the supported clusters. Rhenium atoms bind to the support forming an oxidized substrate, while platinum atoms attach to the rhenium atoms and try minimize the bonds with the surface. This findings confirm experimental observations on the structure of Re-Pt clusters supported on $\gamma\text{-Al}_2\text{O}_3$. The calculated adsorption energies indicate that the most stable Re-Pt clusters supported on $\gamma\text{-Al}_2\text{O}_3$ (100) are Re_2Pt_2 and Re_3Pt_2 . All possible nucleation pathways starting from single atoms were analysed by means of the nucleation energies. It was found that the most favorable nucleation routes lead to the Re_3Pt_2 and Re_5 clusters, while the least favorable path is the coalescence of Pt atoms into monometallic clusters. This finding suggests that alloying Pt clusters with Re adds structural stability compared to monometallic Pt clusters. The electronic properties of those $\gamma\text{-Al}_2\text{O}_3$ -supported Re-Pt clusters were also investigated. A Bader charge analysis revealed that Pt-rich clusters transfer electrons to the $\gamma\text{-Al}_2\text{O}_3$ substrate, while the opposite is true for their Re-rich counterparts. The charge analysis also suggested that Re atoms tend to oxidize, while Pt atoms tend to reduce. The computed PDOS confirmed that the clusters binds to the substrate mainly through Re-O bonds, with negligible contributions from the Pt and Al atoms.

In the final section, a ML approach was employed to study the adsorption of single metal atoms on a pristine MgO surface, as well as the diffusion of H in bulk Pd. BIGDML, the ML method used for these studies, was able to reproduce the fine details of the PES of those systems, using only a small fraction of the training samples extracted from MD runs. This data-efficient method provided reusable force fields with the accuracy *ab initio* methods but at a much lower computational cost. Using BIGDML, it was possible to carry on multiple long-timescale MD simulations—including nuclear quantum effects—to calculate the diffusivity of H atoms in Pd. The diffusion coefficients obtained in this study were in excellent agreement with those experimental values reported in the literature.

The use of modern computational chemistry tools—namely DFT, BH-DFT and ML—enabled the study of the physical and chemical properties of transition metal clusters in this work. Assessing the effect of the interaction of small molecules and metal

oxide surfaces with those clusters was a central element of this study. It was found that those interactions can induce significant changes in the structural and electronic properties of those clusters. While the same could be said about other systems, the highly fluxional nature exhibited by transition metal clusters amplifies those effects. Hence, the fluxionality of metal clusters cannot be ignored if we want a complete study of their properties. To accomplish this task, an exhaustive exploration of their energy landscape must be performed to find all the relevant low-lying structural isomers. However, a thorough PES exploration of supported clusters remains a computational challenge, even on current powerful computers. Among the several obstacles that make this task so difficult are the enormous number of atoms required to model realistic substrates. The supports considered in this study were limited to pristine metal oxide surfaces, which were enough to reveal useful insights into the general properties of supported clusters. Nevertheless, a more complete analysis requires considering surface defects or the presence of molecules such as oxygen, hydrogen or water. Another key element that should be considered is the effect of the temperature on the catalytic properties of supported clusters.

On top of the sheer complexity of supported clusters, there is another issue that must be considered: the limitations of DFT, particularly for highly correlated systems. Overcoming those limitations requires the use of advanced methodologies such as coupled clusters calculations, which can be orders of magnitude more demanding than DFT. Combining all these factors leads to highly complex systems, which require substantial computational resources to be modelled. These problems are not exclusive to supported clusters, and they can be found in all areas of materials science and chemistry. For this reason, machine learning techniques have been applied in an effort to reduce the computational costs involved. By using these techniques, the data generated by computational calculations or experiments can be used to make new predictions and accelerate the research and discovery of new value-added materials. While there is still a lot of room for improvement in these areas, there are clear signs that we are taking steps in the right direction. We are not far from the day when we will be able to readily design new and better catalysts *in silico*, with reduced cost and enhanced properties.

Appendix A

Coordinates of the γ -Al₂O₃ unit cell

40

lattice="5.587 0.000 0.000 0.000 8.413 0.000 -0.083 0.000 8.068"

Al	1.999586	0.630975	4.937354
Al	3.504337	7.782025	3.130218
Al	3.504337	4.837475	3.130218
Al	1.999586	3.575525	4.937354
Al	0.576479	4.871127	6.954247
Al	4.927444	3.541873	1.113325
Al	4.927444	0.664627	1.113325
Al	0.576479	7.748373	6.954247
O	4.892156	3.415678	7.252747
O	0.611766	4.997322	0.814825
O	0.611766	7.622178	0.814825
O	4.892156	0.790822	7.252747
O	3.329125	7.714721	4.953489
O	2.174797	0.698279	3.114083
O	2.174797	3.508222	3.114083
O	3.329125	4.904779	4.953489
O	1.923694	3.415678	6.881639
O	3.580229	4.997322	1.185933
O	3.580229	7.622178	1.185933
O	1.923694	0.790822	6.881639
O	0.718085	7.706308	5.139043
O	4.785837	0.706692	2.928528
O	4.785837	3.499808	2.928528

0	0.718085	4.913192	5.139043
A1	2.095831	6.309750	1.016514
A1	3.408091	2.103250	7.051058
A1	4.878241	6.309750	1.008446
A1	0.625682	2.103250	7.059125
A1	3.374112	6.309750	6.010341
A1	2.129810	2.103250	2.057231
0	4.849537	6.309750	7.051058
0	0.654385	2.103250	1.016514
0	1.959812	6.309750	7.172071
0	3.544111	2.103250	0.895500
A1	4.808143	2.103250	4.017651
A1	0.695779	6.309750	4.049921
0	3.377248	2.103250	5.163246
0	2.126674	6.309750	2.904326
0	0.685394	2.103250	5.058367
0	4.818528	6.309750	3.009204

Bibliography

- ¹W. Wang, S. Wang, X. Ma, and J. Gong, “Recent advances in catalytic hydrogenation of carbon dioxide”, *Chem. Soc. Rev.* **40**, 3703–3727 (2011).
- ²P. G. Jessop, T. Ikariya, and R. Noyori, “Homogeneous hydrogenation of carbon dioxide”, *Chem. Rev.* **95**, 259–272 (1995).
- ³F. V. A. Dutra, B. C. Pires, T. A. Nascimento, and K. B. Borges, “Functional polyaniline/multiwalled carbon nanotube composite as an efficient adsorbent material for removing pharmaceuticals from aqueous media”, *J. Environ. Manage.* **221**, 28–37 (2018).
- ⁴O. Miramontes, F. Bonafé, U. Santiago, E. Larios-Rodriguez, J. J. Velázquez-Salazar, M. M. Mariscal, and M. J. Yacaman, “Ultra-small rhenium clusters supported on graphene”, *Phys. Chem. Chem. Phys.* **17**, 7898–7906 (2015).
- ⁵I. Demiroglu, K. Yao, H. A. Hussein, and R. L. Johnston, “DFT global optimization of gas-phase subnanometer Ru–Pt clusters”, *J. Phys. Chem. C* **121**, 10773–10780 (2017).
- ⁶Y. Wang, B. Xiang, H.-Q. Yang, and C.-W. Hu, “Density functional theory study on the nucleation and growth of Pt_n clusters on γ -Al₂O₃(001) surface”, *ACS Omega* **2**, 3250–3259 (2017).
- ⁷C. Liu, H. He, P. Zapol, and L. A. Curtiss, “Computational studies of electrochemical CO₂ reduction on subnanometer transition metal clusters”, *Phys. Chem. Chem. Phys.* **16**, 26584–26599 (2014).
- ⁸N. Aaron Deskins, D. Mei, and M. Dupuis, “Adsorption and diffusion of a single Pt atom on γ -Al₂O₃ surfaces”, *Surf. Sci.* **603**, 2793–2807 (2009).
- ⁹D. Raciti, J. Kubal, C. Ma, M. Barclay, M. Gonzalez, M. Chi, J. Greeley, K. L. More, and C. Wang, “Pt₃Re alloy nanoparticles as electrocatalysts for the oxygen reduction reaction”, *Nano Energy* **20**, 202–211 (2016).

- ¹⁰M. Gao, A. Lyalin, M. Takagi, S. Maeda, and T. Taketsugu, “Reactivity of gold clusters in the regime of structural fluxionality”, *J. Phys. Chem. C* **119**, 11120–11130 (2015).
- ¹¹A. Corma, A. Leyva-Pérez, and M. Á. Rivero-Crespo, “Ligand-free subnanometre gold metal clusters and their applications”, in *Catalysis: volume 30*, Vol. 30 (The Royal Society of Chemistry, 2018), pp. 21–40.
- ¹²D. Bazin, H. Dexpert, P. Lagarde, and J. P. Bournonville, “Pt-Re on alumina reforming catalysts at the reduced step”, *Le Journal de Physique Colloques* **47**, C8–293–C8–296 (1986).
- ¹³F. Solymosi, “The bonding, structure and reactions of CO₂ adsorbed on clean and promoted metal surfaces”, *J. Mol. Catal.* **65**, 337–358 (1991).
- ¹⁴F. Baletto and R. Ferrando, “Structural properties of nanoclusters: energetic, thermodynamic, and kinetic effects”, *Rev. Mod. Phys.* **77**, 371–423 (2005).
- ¹⁵A. Kulkarni, R. J. Lobo-Lapidus, and B. C. Gates, “Metal clusters on supports: synthesis, structure, reactivity, and catalytic properties”, *Chem. Commun.* **46**, 5997–6015 (2010).
- ¹⁶J. A. van Bokhoven and S. Vajda, “Size selected clusters and particles: from physical chemistry and chemical physics to catalysis”, *Phys. Chem. Chem. Phys.* **16**, 26418–26420 (2014).
- ¹⁷E. Jimenez-Izal and A. N. Alexandrova, “Computational design of clusters for catalysis”, *Annu. Rev. Phys. Chem.* **69**, 377–400 (2018).
- ¹⁸L. Liu and A. Corma, “Evolution of isolated atoms and clusters in catalysis”, *Trends Chem.* **2**, 383–400 (2020).
- ¹⁹R. Ferrando, J. Jellinek, and R. L. Johnston, “Nanoalloys: from theory to applications of alloy clusters and nanoparticles”, *Chem. Rev.* **108**, 845–910 (2008).
- ²⁰R. Ferrando, A. Fortunelli, and R. L. Johnston, “Searching for the optimum structures of alloy nanoclusters”, *Phys. Chem. Chem. Phys.* **10**, 640–649 (2008).
- ²¹F. Negreiros, L. Sementa, G. Barcaro, I. Fechete, L. Piccolo, and A. Fortunelli, “Chapter 8 - reactivity and catalysis by nanoalloys”, in *Nanoalloys (second edition)*, edited by F. Calvo (Elsevier, Oxford, 2020), pp. 267–345.
- ²²C. W. Han, P. Majumdar, E. E. Marinero, A. Aguilar-Tapia, R. Zanella, J. Greeley, and V. Ortalan, “Highly stable bimetallic AuIr/TiO₂ catalyst: physical origins of the intrinsic high stability against sintering”, *Nano Lett.* **15**, 8141–8147 (2015).

- ²³L. Luo, Z. Duan, H. Li, J. Kim, G. Henkelman, and R. M. Crooks, “Tunability of the adsorbate binding on bimetallic alloy nanoparticles for the optimization of catalytic hydrogenation”, *J. Am. Chem. Soc.* **139**, 5538–5546 (2017).
- ²⁴A. S. Duke, K. Xie, J. R. Monnier, and D. A. Chen, “Superior long-term activity for a Pt-Re alloy compared to Pt in methanol oxidation reactions”, *Surf. Sci.* **657**, 35–43 (2017).
- ²⁵A. J. Logsdail, L. O. Paz-Borbón, and C. A. Downing, “DFT-computed trends in the properties of bimetallic precious metal nanoparticles with core@shell segregation”, *J. Phys. Chem. C* **122**, 5721–5730 (2018).
- ²⁶C. H. Wu, C. Liu, D. Su, H. L. Xin, H.-T. Fang, B. Eren, S. Zhang, C. B. Murray, and M. B. Salmeron, “Bimetallic synergy in cobalt–palladium nanocatalysts for CO oxidation”, *Nat. Catal.* **2**, 78–85 (2019).
- ²⁷Q. Sun, N. Wang, Q. Fan, L. Zeng, A. Mayoral, S. Miao, R. Yang, Z. Jiang, W. Zhou, J. Zhang, T. Zhang, J. Xu, P. Zhang, J. Cheng, D.-C. Yang, R. Jia, L. Li, Q. Zhang, Y. Wang, O. Terasaki, and J. Yu, “Subnanometer bimetallic platinum-zinc clusters in zeolites for propane dehydrogenation”, *Angew. Chem. Int. Ed.* **59**, 19450–19459 (2020).
- ²⁸Z. Li, S. Ji, Y. Liu, X. Cao, S. Tian, Y. Chen, Z. Niu, and Y. Li, “Well-defined materials for heterogeneous catalysis: from nanoparticles to isolated single-atom sites”, *Chem. Rev.* **120**, 623–682 (2020).
- ²⁹Y. Lu and W. Chen, “Sub-nanometre sized metal clusters: from synthetic challenges to the unique property discoveries”, *Chem. Soc. Rev.* **41**, 3594–3623 (2012).
- ³⁰M. Sankar, N. Dimitratos, P. J. Miedziak, P. P. Wells, C. J. Kiely, and G. J. Hutchings, “Designing bimetallic catalysts for a green and sustainable future”, *Chem. Soc. Rev.* **41**, 8099–8139 (2012).
- ³¹S. Vajda and M. G. White, “Catalysis applications of size-selected cluster deposition”, *ACS Catal.* **5**, 7152–7176 (2015).
- ³²E. C. Tyo and S. Vajda, “Catalysis by clusters with precise numbers of atoms”, *Nat. Nanotechnol.* **10**, 577–588 (2015).
- ³³L. Liu and A. Corma, “Confining isolated atoms and clusters in crystalline porous materials for catalysis”, *Nat. Rev. Mater.* **6**, 244–263 (2021).
- ³⁴R. L. Johnston, *Atomic and molecular clusters* (Taylor & Francis, 2002).

- ³⁵M. Brust, M. Walker, D. Bethell, D. J. Schiffrin, and R. Whyman, “Synthesis of thiol-derivatised gold nanoparticles in a two-phase liquid–liquid system”, *J. Chem. Soc., Chem. Commun.*, 801–802 (1994).
- ³⁶L. E. Gálvez-González, J. O. Juárez-Sánchez, R. Pacheco-Contreras, I. L. Garzón, L. O. Paz-Borbón, and A. Posada-Amarillas, “CO₂ adsorption on gas-phase Cu_{4-x}Pt_x ($x = 0 - 4$) clusters: a DFT study”, *Phys. Chem. Chem. Phys.* **20**, 17071–17080 (2018).
- ³⁷L. E. Gálvez-González, J. A. Alonso, L. O. Paz-Borbón, and A. Posada-Amarillas, “H₂ adsorption on Cu_{4-x}M_x (M = Au, Pt; $x = 0 - 4$) clusters: similarities and differences as predicted by density functional theory”, *J. Phys. Chem. C* **123**, 30768–30780 (2019).
- ³⁸G. G. Asara, L. O. Paz-Borbón, and F. Baletto, “Get in touch and keep in contact: interface effect on the oxygen reduction reaction (ORR) activity for supported PtNi nanoparticles”, *ACS Catal.* **6**, 4388–4393 (2016).
- ³⁹D. Cheng and W. Wang, “Tailoring of Pd-Pt bimetallic clusters with high stability for oxygen reduction reaction”, *Nanoscale* **4**, 2408–2415 (2012).
- ⁴⁰C. Song, Q. Ge, and L. Wang, “DFT studies of Pt/Au bimetallic clusters and their interactions with the CO molecule”, *J. Phys. Chem. B* **109**, 22341–22350 (2005).
- ⁴¹P. Ferrari, G. Libeert, N. M. Tam, and E. Janssens, “Interaction of carbon monoxide with doped metal clusters”, *CrystEngComm* **22**, 4807–4815 (2020).
- ⁴²T. J. Gorey, B. Zandkarimi, G. Li, E. T. Baxter, A. N. Alexandrova, and S. L. Anderson, “Coking-resistant sub-nano dehydrogenation catalysts: Pt_nSn_x/SiO₂ ($n = 4, 7$)”, *ACS Catal.* **10**, 4543–4558 (2020).
- ⁴³V. A. Rigo, C. R. Miranda, and F. Baletto, “Ethanol chemisorption on core–shell Pt-nanoparticles: an ab initio study”, *Eur. Phys. J. B* **92**, 24 (2019).
- ⁴⁴H.-J. Freund, “Clusters and islands on oxides: from catalysis via electronics and magnetism to optics”, *Surf. Sci.* **500**, 271–299 (2002).
- ⁴⁵J. K. Nørskov, F. Abild-Pedersen, F. Studt, and T. Bligaard, “Density functional theory in surface chemistry and catalysis”, *Proceedings of the National Academy of Sciences* **108**, 937–943 (2011).
- ⁴⁶L. Grajciar, C. J. Heard, A. A. Bondarenko, M. V. Polynski, J. Meeprasert, E. A. Pidko, and P. Nachtigall, “Towards operando computational modeling in heterogeneous catalysis”, *Chem. Soc. Rev.* **47**, 8307–8348 (2018).

- ⁴⁷T. R. Henninen, M. Bon, F. Wang, D. Passerone, and R. Erni, “The structure of sub-nm platinum clusters at elevated temperatures”, *Angew. Chem. Int. Ed.* **59**, 839–845 (2020).
- ⁴⁸A. J. Medford, A. Vojvodic, J. S. Hummelshøj, J. Voss, F. Abild-Pedersen, F. Studt, T. Bligaard, A. Nilsson, and J. K. Nørskov, “From the sabatier principle to a predictive theory of transition-metal heterogeneous catalysis”, *J. Catal.* **328**, 36–42 (2015).
- ⁴⁹Y. Zhang, X. Yang, Y. Zhou, G. Li, Z. Li, C. Liu, M. Bao, and W. Shen, “Selective hydrogenation of the C-C bond in α,β -unsaturated aldehydes and ketones over ultra-small Pd-Au clusters”, *Nanoscale* **8**, 18626–18629 (2016).
- ⁵⁰F. Giustino, *Materials modelling using density functional theory* (Oxford University Press, 2014).
- ⁵¹R. O. Jones, “Density functional theory: its origins, rise to prominence, and future”, *Rev. Mod. Phys.* **87**, 897–923 (2015).
- ⁵²L. M. Ghiringhelli, P. Gruene, J. T. Lyon, D. M. Rayner, G. Meijer, A. Fielicke, and M. Scheffler, “Not so loosely bound rare gas atoms: finite-temperature vibrational fingerprints of neutral gold-cluster complexes”, *New. J. Phys.* **15**, 083003 (2013).
- ⁵³O. T. Unke, S. Chmiela, H. E. Saucedo, M. Gastegger, I. Poltavsky, K. T. Schütt, A. Tkatchenko, and K.-R. Müller, “Machine learning force fields”, *Chem. Rev.* **121**, 10142–10186 (2021).
- ⁵⁴S. Chmiela, A. Tkatchenko, H. E. Saucedo, I. Poltavsky, K. T. Schütt, and K.-R. Müller, “Machine learning of accurate energy-conserving molecular force fields”, *Sci. Adv.* **3**, e1603015 (2017).
- ⁵⁵S. Chmiela, H. E. Saucedo, K.-R. Müller, and A. Tkatchenko, “Towards exact molecular dynamics simulations with machine-learned force fields”, *Nat. Commun.* **9**, 3887 (2018).
- ⁵⁶S. Chmiela, H. E. Saucedo, I. Poltavsky, K.-R. Müller, and A. Tkatchenko, “sGDML: constructing accurate and data efficient molecular force fields using machine learning”, *Comput. Phys. Commun.* **240**, 38–45 (2019).
- ⁵⁷H. E. Saucedo, S. Chmiela, I. Poltavsky, K.-R. Müller, and A. Tkatchenko, “Molecular force fields with gradient-domain machine learning: construction and application to dynamics of small molecules with coupled cluster forces”, *J. Chem. Phys.* **150**, 114102 (2019).

- ⁵⁸H. E. Saucedo, S. Chmiela, I. Poltavsky, K.-R. Müller, and A. Tkatchenko, “Construction of machine learned force fields with quantum chemical accuracy: applications and chemical insights”, in *Machine learning meets quantum physics*, edited by K. T. Schütt, S. Chmiela, O. A. von Lilienfeld, A. Tkatchenko, K. Tsuda, and K.-R. Müller (Springer International Publishing, 2020), pp. 277–307.
- ⁵⁹H. E. Saucedo, M. Gastegger, S. Chmiela, K.-R. Müller, and A. Tkatchenko, “Molecular force fields with gradient-domain machine learning (GDML): comparison and synergies with classical force fields”, *J. Chem. Phys.* **153**, 124109 (2020).
- ⁶⁰S. Chmiela, *Towards exact molecular dynamics simulations with invariant machine-learned models* (Technische Universität Berlin (Germany), 2019).
- ⁶¹Z. Li, J. R. Kermode, and A. De Vita, “Molecular dynamics with on-the-fly machine learning of quantum-mechanical forces”, *Phys. Rev. Lett.* **114**, 096405 (2015).
- ⁶²A. Glielmo, P. Sollich, and A. De Vita, “Accurate interatomic force fields via machine learning with covariant kernels”, *Phys. Rev. B* **95**, 214302 (2017).
- ⁶³A. Glielmo, C. Zeni, and A. De Vita, “Efficient nonparametric n -body force fields from machine learning”, *Phys. Rev. B* **97**, 184307 (2018).
- ⁶⁴T. D. Huan, R. Batra, J. Chapman, S. Krishnan, L. Chen, and R. Ramprasad, “A universal strategy for the creation of machine learning-based atomistic force fields”, *Npj Comput. Mater* **3**, 37 (2017).
- ⁶⁵A. Seko, A. Takahashi, and I. Tanaka, “First-principles interatomic potentials for ten elemental metals via compressed sensing”, *Phys. Rev. B* **92**, 054113 (2015).
- ⁶⁶V. Botu and R. Ramprasad, “Adaptive machine learning framework to accelerate ab initio molecular dynamics”, *Int. J. Quantum Chem.* **115**, 1074–1083 (2015).
- ⁶⁷T. Suzuki, R. Tamura, and T. Miyazaki, “Machine learning for atomic forces in a crystalline solid: transferability to various temperatures”, *Int. J. Quantum Chem.* **117**, 33–39 (2017).
- ⁶⁸J. Behler and M. Parrinello, “Generalized neural-network representation of high-dimensional potential-energy surfaces”, *Phys. Rev. Lett.* **98**, 146401 (2007).
- ⁶⁹A. P. Bartók, M. C. Payne, R. Kondor, and G. Csányi, “Gaussian approximation potentials: the accuracy of quantum mechanics, without the electrons”, *Phys. Rev. Lett.* **104**, 136403 (2010).

- ⁷⁰J. Schmidt, M. R. G. Marques, S. Botti, and M. A. L. Marques, “Recent advances and applications of machine learning in solid-state materials science”, *npj Comput. Mater* **5**, 83 (2019).
- ⁷¹J. R. Boes, M. C. Groenenboom, J. A. Keith, and J. R. Kitchin, “Neural network and ReaxFF comparison for Au properties”, *Int. J. Quantum Chem.* **116**, 979–987 (2016).
- ⁷²J. Behler, “First principles neural network potentials for reactive simulations of large molecular and condensed systems”, *Angew. Chem. Int. Ed.* **56**, 12828–12840 (2017).
- ⁷³N. Artrith and J. Behler, “High-dimensional neural network potentials for metal surfaces: a prototype study for copper”, *Phys. Rev. B* **85**, 045439 (2012).
- ⁷⁴J. Weinreich, A. Römer, M. L. Paleico, and J. Behler, “Properties of α -brass nanoparticles. 1. neural network potential energy surface”, *J. Phys. Chem. C* **124**, 12682–12695 (2020).
- ⁷⁵C. Zeni, K. Rossi, A. Glielmo, \tilde{A} . Fekete, N. Gaston, F. Baletto, and A. De Vita, “Building machine learning force fields for nanoclusters”, *J. Chem. Phys.* **148**, 241739 (2018).
- ⁷⁶H. Zhai and A. N. Alexandrova, “Ensemble-average representation of Pt clusters in conditions of catalysis accessed through GPU accelerated deep neural network fitting global optimization”, *J. Chem. Theory Comput.* **12**, 6213–6226 (2016).
- ⁷⁷H. Zhai and A. N. Alexandrova, “Fluxionality of catalytic clusters: when it matters and how to address it”, *ACS Catal.* **7**, 1905–1911 (2017).
- ⁷⁸R. P. Feynman, “Forces in molecules”, *Phys. Rev.* **56**, 340–343 (1939).
- ⁷⁹D. Wales, *Energy landscapes: applications to clusters, biomolecules and glasses*, Cambridge Molecular Science (Cambridge University Press, 2004).
- ⁸⁰R. O. Jones and O. Gunnarsson, “The density functional formalism, its applications and prospects”, *Rev. Mod. Phys.* **61**, 689–746 (1989).
- ⁸¹P. Hohenberg and W. Kohn, “Inhomogeneous electron gas”, *Phys. Rev.* **136**, B864–B871 (1964).
- ⁸²W. Kohn and L. J. Sham, “Self-consistent equations including exchange and correlation effects”, *Phys. Rev.* **140**, A1133–A1138 (1965).
- ⁸³J. P. Perdew and K. Schmidt, “Jacob’s ladder of density functional approximations for the exchange-correlation energy”, *AIP Conf. Proc.* **577**, 1–20 (2001).

- ⁸⁴Y. Zhao and D. G. Truhlar, “A new local density functional for main-group thermochemistry, transition metal bonding, thermochemical kinetics, and noncovalent interactions.”, *J. Chem. Phys.* **125**, 194101 (2006).
- ⁸⁵J. P. Perdew, K. Burke, and M. Ernzerhof, “Generalized gradient approximation made simple”, *Phys. Rev. Lett.* **77**, 3865–3868 (1996).
- ⁸⁶T. M. Soini, A. Genest, A. Nikodem, and N. Rösch, “Hybrid density functionals for clusters of late transition metals: assessing energetic and structural properties”, *J. Chem. Theory Comput.* **10**, 4408–4416 (2014).
- ⁸⁷P. Janthon, S. (Luo, S. M. Kozlov, F. Viñes, J. Limtrakul, D. G. Truhlar, and F. Illas, “Bulk properties of transition metals: a challenge for the design of universal density functionals”, *J. Chem. Theory Comput.* **10**, 3832–3839 (2014).
- ⁸⁸M. J. Piotrowski, P. Piquini, and J. L. F. Da Silva, “Platinum-based nanoalloys $\text{Pt}_n\text{TM}_{55-n}$ (TM = Co, Rh, Au): a density functional theory investigation”, *J. Phys. Chem. C* **116**, 18432–18439 (2012).
- ⁸⁹A. S. Chaves, M. J. Piotrowski, and J. L. F. Da Silva, “Evolution of the structural, energetic, and electronic properties of the 3d, 4d, and 5d transition-metal clusters (30 TM_n systems for $n = 2 - 15$): a density functional theory investigation”, *Phys. Chem. Chem. Phys.* **19**, 15484–15502 (2017).
- ⁹⁰F. Baletto, “Structural properties of sub-nanometer metallic clusters”, *J. Phys. Condens. Matter* **31**, 113001 (2019).
- ⁹¹V. I. Anisimov, J. Zaanen, and O. K. Andersen, “Band theory and mott insulators: HubbardUinstead of StonerI”, *Phys. Rev. B* **44**, 943–954 (1991).
- ⁹²A. I. Liechtenstein, V. I. Anisimov, and J. Zaanen, “Density-functional theory and strong interactions: orbital ordering in Mott-Hubbard insulators”, *Phys. Rev. B* **52**, R5467–R5470 (1995).
- ⁹³N. Daelman, F. S. Hegner, M. Rellán-Piñeiro, M. Capdevila-Cortada, R. Garcia-Muelas, and N. López, “Quasi-degenerate states and their dynamics in oxygen deficient reducible metal oxides”, *J. Chem. Phys.* **152**, 050901 (2020).
- ⁹⁴S. Grimme, “Semiempirical GGA-type density functional constructed with a long-range dispersion correction”, *J. Comput. Chem.* **27**, 1787–1799 (2006).
- ⁹⁵S. Grimme, J. Antony, S. Ehrlich, and H. Krieg, “A consistent and accurate ab initio parametrization of density functional dispersion correction (DFT-D) for the 94 elements H-Pu”, *J. Chem. Phys.* **132**, 154104 (2010).

- ⁹⁶A. Tkatchenko and M. Scheffler, “Accurate molecular van der waals interactions from ground-state electron density and free-atom reference data”, *Phys. Rev. Lett.* **102**, 073005 (2009).
- ⁹⁷D. Sheppard, R. Terrell, and G. Henkelman, “Optimization methods for finding minimum energy paths”, *J. Chem. Phys.* **128**, 134106 (2008).
- ⁹⁸J. Nocedal, “Updating quasi-newton matrices with limited storage”, *Math. Comput.* **35**, 773–773 (1980).
- ⁹⁹E. Bitzek, P. Koskinen, F. Gähler, M. Moseler, and P. Gumbsch, “Structural relaxation made simple”, *Phys. Rev. Lett.* **97**, 170201 (2006).
- ¹⁰⁰M. Hestenes and E. Stiefel, “Methods of conjugate gradients for solving linear systems”, *J. Res. Natl. Inst. Stand.* **49**, 409 (1952).
- ¹⁰¹H. B. Schlegel, “Optimization of equilibrium geometries and transition structures”, *J. Comput. Chem.* **3**, 214–218 (1982).
- ¹⁰²M. J. Frisch, G. W. Trucks, H. B. Schlegel, G. E. Scuseria, M. A. Robb, J. R. Cheeseman, G. Scalmani, V. Barone, G. A. Petersson, H. Nakatsuji, X. Li, M. Caricato, A. V. Marenich, J. Bloino, B. G. Janesko, R. Gomperts, B. Mennucci, H. P. Hratchian, J. V. Ortiz, A. F. Izmaylov, J. L. Sonnenberg, D. Williams-Young, F. Ding, F. Lipparini, F. Egidi, J. Goings, B. Peng, A. Petrone, T. Henderson, D. Ranasinghe, V. G. Zakrzewski, J. Gao, N. Rega, G. Zheng, W. Liang, M. Hada, M. Ehara, K. Toyota, R. Fukuda, J. Hasegawa, M. Ishida, T. Nakajima, Y. Honda, O. Kitao, H. Nakai, T. Vreven, K. Throssell, J. A. Montgomery Jr., J. E. Peralta, F. Ogliaro, M. J. Bearpark, J. J. Heyd, E. N. Brothers, K. N. Kudin, V. N. Staroverov, T. A. Keith, R. Kobayashi, J. Normand, K. Raghavachari, A. P. Rendell, J. C. Burant, S. S. Iyengar, J. Tomasi, M. Cossi, J. M. Millam, M. Klene, C. Adamo, R. Cammi, J. W. Ochterski, R. L. Martin, K. Morokuma, O. Farkas, J. B. Foresman, and D. J. Fox, *Gaussian ~09 Revision B.01*, Gaussian Inc. Wallingford CT, 2009.
- ¹⁰³P. Giannozzi, S. Baroni, N. Bonini, M. Calandra, R. Car, C. Cavazzoni, D. Ceresoli, G. L. Chiarotti, M. Cococcioni, I. Dabo, A. Dal Corso, S. de Gironcoli, S. Fabris, G. Fratesi, R. Gebauer, U. Gerstmann, C. Gougoussis, A. Kokalj, M. Lazzeri, L. Martin-Samos, N. Marzari, F. Mauri, R. Mazzarello, S. Paolini, A. Pasquarello, L. Paulatto, C. Sbraccia, S. Scandolo, G. Sclauzero, A. P. Seitsonen, A. Smogunov, P. Umari, and R. M. Wentzcovitch, “QUANTUM ESPRESSO: a modular and open-source software project for quantum simulations of materials”, *J. Phys. Condens. Matter* **21**, 395502 (19pp) (2009).

- ¹⁰⁴P. Giannozzi, O. Andreussi, T. Brumme, O. Bunau, M. B. Nardelli, M. Calandra, R. Car, C. Cavazzoni, D. Ceresoli, M. Cococcioni, N. Colonna, I. Carnimeo, A. D. Corso, S. de Gironcoli, P. Delugas, R. A. D. Jr, A. Ferretti, A. Floris, G. Fratesi, G. Fugallo, R. Gebauer, U. Gerstmann, F. Giustino, T. Gorni, J. Jia, M. Kawamura, H.-Y. Ko, A. Kokalj, E. Küçükbenli, M. Lazzeri, M. Marsili, N. Marzari, F. Mauri, N. L. Nguyen, H.-V. Nguyen, A. Otero-de-la-Roza, L. Paulatto, S. Poncé, D. Rocca, R. Sabatini, B. Santra, M. Schlipf, A. P. Seitsonen, A. Smogunov, I. Timrov, T. Thonhauser, P. Umari, N. Vast, X. Wu, and S. Baroni, “Advanced capabilities for materials modelling with QUANTUM ESPRESSO”, *J. Phys. Condens. Matter* **29**, 465901 (2017).
- ¹⁰⁵M. Dolg and X. Cao, “Relativistic pseudopotentials: their development and scope of applications”, *Chem. Rev.* **112**, 403–480 (2012).
- ¹⁰⁶J. Wang, L. Ma, J. Zhao, and K. A. Jackson, “Structural growth behavior and polarizability of Cd_nTe_n ($n = 1\sim 14$) clusters”, *J. Chem. Phys.* **130**, 214307 (2009).
- ¹⁰⁷D. J. Wales and J. P. K. Doye, “Global optimization by basin-hopping and the lowest energy structures of Lennard-Jones clusters containing up to 110 atoms”, *J. Phys. Chem. A* **101**, 5111–5116 (1997).
- ¹⁰⁸R. L. Johnston, “Evolving better nanoparticles: genetic algorithms for optimising cluster geometries”, *Datlon Trans.*, 4193–4207 (2003).
- ¹⁰⁹S. T. Call, D. Y. Zubarev, and A. I. Boldyrev, “Global minimum structure searches via particle swarm optimization”, *J. Comput. Chem.* **28**, 1177–1186 (2007).
- ¹¹⁰J. C. Luque-Ceballos, A. Posada-Borbón, R. Herrera-Urbina, R. Aceves, J. O. Juárez-Sánchez, and A. Posada-Amarillas, “A theoretical study on the geometry and spectroscopic properties of ground-state and local minima isomers of $(\text{CuS})_{n=2-6}$ clusters”, *Physica E* **97**, 1–7 (2018).
- ¹¹¹L. O. Paz-Borbón, A. López-Martínez, I. L. Garzón, A. Posada-Amarillas, and H. Grönbeck, “2D–3D structural transition in sub-nanometer Pt_N clusters supported on $\text{CeO}_2(111)$ ”, *Phys. Chem. Chem. Phys.* **19**, 17845–17855 (2017).
- ¹¹²J. I. Martínez and J. A. Alonso, “An improved descriptor of cluster stability: application to small carbon clusters”, *Phys. Chem. Chem. Phys.* **20**, 27368–27374 (2018).
- ¹¹³Y. Wang, B. Xiang, H.-Q. Yang, and C.-W. Hu, “Density functional theory study on the nucleation and growth of Pt_n clusters on $\gamma\text{-Al}_2\text{O}_3(001)$ Surface”, *ACS Omega* **2**, 3250–3259 (2017).

- ¹¹⁴Z. H. Li, A. W. Jasper, and D. G. Truhlar, “Structures, rugged energetic landscapes, and nanothermodynamics of Al_n ($2 \leq n \leq 65$) particles”, *J. Am. Chem. Soc.* **129**, 14899–14910 (2007).
- ¹¹⁵V. G. Grigoryan and M. Springborg, “Temperature and isomeric effects in nanoclusters”, *Phys. Chem. Chem. Phys.* **21**, 5646–5654 (2019).
- ¹¹⁶K. Ding, A. Gulec, A. M. Johnson, N. M. Schweitzer, G. D. Stucky, L. D. Marks, and P. C. Stair, “Identification of active sites in CO oxidation and water-gas shift over supported Pt catalysts”, *Science* **350**, 189–192 (2015).
- ¹¹⁷L. Bai, X. Wang, Q. Chen, Y. Ye, H. Zheng, J. Guo, Y. Yin, and C. Gao, “Explaining the size dependence in platinum-nanoparticle-catalyzed hydrogenation reactions”, *Angew. Chem. Int. Ed.* **55**, 15656–15661 (2016).
- ¹¹⁸A. A. Herzing, C. J. Kiely, A. F. Carley, P. Landon, and G. J. Hutchings, “Identification of active gold nanoclusters on iron oxide supports for CO oxidation”, *Science* **321**, 1331–1335 (2008).
- ¹¹⁹A. Corma, “Chemoselective hydrogenation of nitro compounds with supported gold catalysts”, *Science* **313**, 332–334 (2006).
- ¹²⁰J. K. Norskov and C. H. Christensen, “Toward efficient hydrogen production at surfaces”, *Science* **312**, 1322–1323 (2006).
- ¹²¹W. Wang, S. Wang, X. Ma, and J. Gong, “Recent advances in catalytic hydrogenation of carbon dioxide”, *Chem. Soc. Rev.* **40**, 3703 (2011).
- ¹²²Y. Li, S. H. Chan, and Q. Sun, “Heterogeneous catalytic conversion of CO_2 : a comprehensive theoretical review”, *Nanoscale* **7**, 8663–8683 (2015).
- ¹²³M. Haruta, T. Kobayashi, H. Sano, and N. Yamada, “Novel gold catalysts for the oxidation of carbon monoxide at a temperature far below 0 °C”, *Chem. Lett.* **16**, 405–408 (1987).
- ¹²⁴O. K. Varghese, M. Paulose, T. J. LaTempa, and C. A. Grimes, “High-rate solar photocatalytic conversion of CO_2 and water vapor to hydrocarbon fuels”, *Nano Lett.* **9**, 731–737 (2009).
- ¹²⁵M. Huš, D. Kopač, and B. Likozar, “Catalytic hydrogenation of carbon dioxide to methanol: synergistic effect of bifunctional Cu/perovskite catalysts”, *ACS Catal.* **9**, 105–116 (2018).

- ¹²⁶G. Zhao, X. Huang, X. Wang, and X. Wang, “Progress in catalyst exploration for heterogeneous CO₂ reduction and utilization: a critical review”, *J. Mater. Chem. A* **5**, 21625–21649 (2017).
- ¹²⁷D. Bazin, D. Guillaume, C. Pichon, D. Uzio, and S. Lopez, “Structure and size of bimetallic palladium-platinum clusters in an hydrotreatment”, *Oil Gas Sci. Technol.* **60**, 801–813 (2005).
- ¹²⁸D. Wang, A. Villa, F. Porta, L. Prati, and D. Su, “Bimetallic gold/palladium catalysts: correlation between nanostructure and synergistic effects”, *J. Phys. Chem. C* **112**, 8617–8622 (2008).
- ¹²⁹R. Ferrando, J. Jellinek, and R. L. Johnston, “Nanoalloys: from theory to applications of alloy clusters and nanoparticles”, *Chem. Rev.* **108**, 845–910 (2008).
- ¹³⁰B. Hagman, A. Posada-Borbón, A. Schaefer, M. Shipilin, C. Zhang, L. R. Merte, A. Hellman, E. Lundgren, H. Grönbeck, and J. Gustafson, “Steps control the dissociation of CO₂ on Cu(100)”, *J. Am. Chem. Soc.* **140**, 12974–12979 (2018).
- ¹³¹M. Blanco-Rey, J. I. Juaristi, M. Alducin, M. J. López, and J. A. Alonso, “Is spillover relevant for hydrogen adsorption and storage in porous carbons doped with palladium nanoparticles?”, *J. Phys. Chem. C* **120**, 17357–17364 (2016).
- ¹³²A. Granja-DelRío, J. A. Alonso, and M. J. López, “Competition between palladium clusters and hydrogen to saturate graphene vacancies”, *J. Phys. Chem. C* **121**, 10843–10850 (2017).
- ¹³³A. L. Linsebigler, G. Lu, and J. T. Yates, “Photocatalysis on TiO₂ surfaces: principles, mechanisms, and selected results”, *Chem. Rev.* **95**, 735–758 (1995).
- ¹³⁴Z. W. Seh, J. Kibsgaard, C. F. Dickens, I. Chorkendorff, J. K. Nørskov, and T. F. Jaramillo, “Combining theory and experiment in electrocatalysis: insights into materials design”, *Science* **355**, eaad4998 (2017).
- ¹³⁵S. Zhao, X. Tian, J. Liu, Y. Ren, Y. Ren, and J. Wang, “Density functional study of molecular hydrogen adsorption on small gold-copper binary clusters”, *J. Clust. Sci.* **26**, 491–503 (2015).
- ¹³⁶E. M. Fernández, J. M. Soler, I. L. Garzón, and L. C. Balbás, “Trends in the structure and bonding of noble metal clusters”, *Phys. Rev. B* **70**, 165403 (2004).
- ¹³⁷G. H. Guvelioglu, P. Ma, X. He, R. C. Forrey, and H. Cheng, “Evolution of small copper clusters and dissociative chemisorption of hydrogen”, *Phys. Rev. Lett.* **94**, 026103 (2005).

- ¹³⁸L. M. Ghiringhelli, P. Gruene, J. T. Lyon, D. M. Rayner, G. Meijer, A. Fielicke, and M. Scheffler, “Not so loosely bound rare gas atoms: finite-temperature vibrational fingerprints of neutral gold-cluster complexes”, *New. J. Phys.* **15**, 083003 (2013).
- ¹³⁹A. Trincherro, S. Klacar, L. O. Paz-Borbón, A. Hellman, and H. Grönbeck, “Oxidation at the subnanometer scale”, *J. Phys. Chem. C* **119**, 10797–10803 (2014).
- ¹⁴⁰A. S. Chaves, G. G. Rondina, M. J. Piotrowski, and J. L. D. Silva, “Structural formation of binary PtCu clusters: a density functional theory investigation”, *Comput. Mater. Sci.* **98**, 278–286 (2015).
- ¹⁴¹Z. Fang and X. Kuang, “Hydrogen molecule adsorption on Au_nPt ($n=1-12$) clusters in comparison with corresponding pure Au_n^{+1} ($n=1-12$) clusters”,
- ¹⁴²C. Kerpál, D. J. Harding, D. M. Rayner, and A. Fielicke, “Small platinum cluster hydrides in the gas phase”, *J. Phys. Chem. A* **117**, 8230–8237 (2013).
- ¹⁴³P. S. Petkov, G. P. Petrova, G. N. Vayssilov, and N. Rösch, “Saturation of small supported metal clusters by adsorbed hydrogen. a computational study on tetrahedral models of Rh_4 , Ir_4 , and Pt_4 ”, *J. Phys. Chem. C* **114**, 8500–8506 (2010).
- ¹⁴⁴J. B. A. Davis, F. Baletto, and R. L. Johnston, “The effect of dispersion correction on the adsorption of CO on metallic nanoparticles”, *J. Phys. Chem. A* **119**, 9703–9709 (2015).
- ¹⁴⁵L. Paz-Borbón and F. Baletto, “A DFT study on the O_2 adsorption properties of supported PtNi clusters”, *Inorganics* **5**, 43 (2017).
- ¹⁴⁶D. J. Gorin and F. D. Toste, “Relativistic effects in homogeneous gold catalysis”, *Nature* **446**, 395–403 (2007).
- ¹⁴⁷J. Desclaux and P. Pyykkö, “Dirac-Fock one-centre calculations. the molecules CuH, AgH and AuH including p-type symmetry functions”, *Chem. Phys. Lett.* **39**, 300–303 (1976).
- ¹⁴⁸P. G. Jones and A. J. Kirby, “Simple correlation between bond length and reactivity. combined use of crystallographic and kinetic data to explore a reaction coordinate”, *J. Am. Chem. Soc.* **106**, 6207–6212 (1984).
- ¹⁴⁹E. D. Glendening, C. R. Landis, and F. Weinhold, “Natural bond orbital methods”, *Wiley Interdiscip. Rev. Comput. Mol. Sci.* **2**, 1–42 (2011).
- ¹⁵⁰K. García-Diez, J. Fernández-Fernández, J. A. Alonso, and M. J. López, “Theoretical study of the adsorption of hydrogen on cobalt clusters”, *Phys. Chem. Chem. Phys.* **20**, 21163–21176 (2018).

- ¹⁵¹J.-D. Chai and M. Head-Gordon, “Long-range corrected hybrid density functionals with damped atom-atom dispersion corrections”, *Phys. Chem. Chem. Phys.* **10**, 6615 (2008).
- ¹⁵²W. Gao, T. A. Abtew, T. Cai, Y.-Y. Sun, S. Zhang, and P. Zhang, “On the applicability of hybrid functionals for predicting fundamental properties of metals”, *Solid State Commun.* **234-235**, 10–13 (2016).
- ¹⁵³J. Paier, M. Marsman, and G. Kresse, “Why does the B3LYP hybrid functional fail for metals?”, *J. Chem. Phys.* **127**, 024103 (2007).
- ¹⁵⁴S. Liem and J. Clarke, “Evidence from first principles calculations for a bent CO₂ intermediate in the oxidation of carbon monoxide on the Cu (110) surface”, English, *J. Chem. Phys.* **121**, 4339–4345 (2004).
- ¹⁵⁵H.-J. Freund and M. Roberts, “Surface chemistry of carbon dioxide”, *Surf. Sci. Rep.* **25**, 225–273 (1996).
- ¹⁵⁶Y.-G. Wang, K. B. Wiberg, and N. H. Werstiuk, “Correlation effects in EOM-CCSD for the excited states: evaluated by AIM localization index (LI) and delocalization index (DI)”, *J. Phys. Chem. A* **111**, 3592–3601 (2007).
- ¹⁵⁷Z. W. Wang and R. E. Palmer, “Direct atomic imaging and dynamical fluctuations of the tetrahedral Au₂O cluster”, *Nanoscale* **4**, 4947 (2012).
- ¹⁵⁸J. K. Nørskov, J. Rossmeisl, A. Logadottir, L. Lindqvist, J. R. Kitchin, T. Bligaard, and H. Jónsson, “Origin of the overpotential for oxygen reduction at a fuel-cell cathode”, *J. Phys. Chem. B* **108**, 17886–17892 (2004).
- ¹⁵⁹X. Wang, Z. Li, Y. Qu, T. Yuan, W. Wang, Y. Wu, and Y. Li, “Review of metal catalysts for oxygen reduction reaction: from nanoscale engineering to atomic design”, *Chem* **5**, 1486–1511 (2019).
- ¹⁶⁰P. Caron and T. Khan, “Evolution of Ni-based superalloys for single crystal gas turbine blade applications”, *Aerosp. Sci. Technol.* **3**, 513–523 (1999).
- ¹⁶¹H. Iida, K. Yonezawa, M. Kosaka, and A. Igarashi, “Low-temperature water gas shift reaction over Pt-Re/TiO₂ catalysts prepared by a sub-critical drying method”, *Catal. Commun.* **10**, 627–630 (2009).
- ¹⁶²A. S. Duke, K. Xie, A. J. Brandt, T. D. Maddumapatabandi, S. C. Ammal, A. Heyden, J. R. Monnier, and D. A. Chen, “Understanding active sites in the water-gas shift reaction for Pt-Re catalysts on titania”, *ACS Catal.* **7**, 2597–2606 (2017).

- ¹⁶³C. T. Campbell, “Bimetallic surface chemistry”, *Annu. Rev. Phys. Chem.* **41**, 775–837 (1990).
- ¹⁶⁴T. Gjervan, R. Prestvik, and A. Holmen, “Catalytic reforming”, in *Basic principles in appl. catalysis*, edited by M. Baerns (Springer Berlin Heidelberg, Berlin, Heidelberg, 2004), pp. 125–158.
- ¹⁶⁵M. R. Rahimpour, M. Jafari, and D. Iranshahi, “Progress in catalytic naphtha reforming process: a review”, *Appl. Energy* **109**, 79–93 (2013).
- ¹⁶⁶R. Mieville, “Platinum-rhenium interaction: a temperature-programmed reduction study”, *J. Catal.* **87**, 437–442 (1984).
- ¹⁶⁷E. Drzymala, G. Gruzel, J. Depciuch, M. Pawlyta, M. Donten, and M. Parlinska-Wojtan, “Ternary Pt/Re/SnO₂/C catalyst for EOR: electrocatalytic activity and durability enhancement”, *Nano Res.* **13**, 832–842 (2020).
- ¹⁶⁸J. Barbier, “Deactivation of reforming catalysts by coking - a review”, *Appl. Catal.* **23**, 225–243 (1986).
- ¹⁶⁹D. J. Godbey, F. Garin, and G. A. Somorjai, “The hydrogenolysis of ethane over Re-Pt(111) and Pt-Re(0001) bimetallic crystal surfaces”, *J. Catal.* **117**, 144–154 (1989).
- ¹⁷⁰J. A. Anderson, F. K. Chong, and C. H. Rochester, “IR study of CO adsorption on Pt, Re and Pt-Re/Al₂O₃ catalysts before and after coking”, *J. Mol. Catal. A Chem.* **140**, 65–80 (1999).
- ¹⁷¹X. J. Feng, T. T. Cao, L. X. Zhao, Y. M. Lei, and Y. Luo, “Structural and electronic properties of Re_n ($n \leq 8$) clusters by density functional theory”, *Eur. Phys. J. D* **50**, 285–288 (2008).
- ¹⁷²R.-N. Zhao, R. Chen, Y.-H. Yuan, J.-G. Han, and Y. Duan, “Computational investigation on the structures and electronic properties of the nanosized rhenium clusters”, *Solid State Ion.* **310**, 24–29 (2017).
- ¹⁷³O. Miramontes, F. Bonafé, U. Santiago, E. Larios-Rodriguez, J. J. Velázquez-Salazar, M. M. Mariscal, and M. J. Yacaman, “Ultra-small rhenium clusters supported on graphene”, *Phys. Chem. Chem. Phys.* **17**, 7898–7906 (2015).
- ¹⁷⁴J. Sui, X. Wang, and P. An, “Geometric evolution, stability trend and electronic properties of rhenium-doped gold clusters”, *Comput. Theor. Chem.* **1028**, 98–105 (2014).

- ¹⁷⁵Q. Du, X. Wu, P. Wang, D. Wu, L. Sai, R. B. King, S. J. Park, and J. Zhao, “Structure evolution of transition metal-doped gold clusters $M@Au_{12}$ ($M = 3d - 5d$): across the periodic table”, *J. Phys. Chem. C* **124**, 7449–7457 (2020).
- ¹⁷⁶V. Bakken and O. Swang, “Atomistic and electronic structure of bimetallic cobalt/rhenium clusters from density functional theory calculations”, *J. Chem. Phys.* **128**, 084712 (2008).
- ¹⁷⁷R.-N. Zhao, R. Chen, F. Lin, and Z.-W. Sun, “The stabilities and geometries of Re-encapsulated Si_n ($n=16, 20, 24, 28, 32, 36, \text{ and } 40$) clusters: a computational investigation”, *Main Group Metal Chemistry* **42**, 81–93 (2019).
- ¹⁷⁸J.-G. Han, Z.-Y. Ren, and B.-Z. Lu, “Geometries and stabilities of Re-doped Si_n ($n = 1 - 12$) clusters: a density functional investigation”, *J. Phys. Chem. A* **108**, 5100–5110 (2004).
- ¹⁷⁹R. D. Adams, B. Captain, and M. D. Smith, “A highly unsaturated platinum-rhenium cluster complex activates hydrogen reversibly”, *Angew. Chem. Int. Ed.* **45**, 1109–1112 (2006).
- ¹⁸⁰R. D. Adams, B. Captain, M. D. Smith, C. Beddie, and M. B. Hall, “Unsaturated platinum-rhenium cluster complexes. synthesis, structures and reactivity”, *J. Am. Chem. Soc.* **129**, 5981–5991 (2007).
- ¹⁸¹J. Greeley and M. Mavrikakis, “Alloy catalysts designed from first principles”, *Nat. Mater.* **3**, 810–815 (2004).
- ¹⁸²J. Greeley, T. F. Jaramillo, J. Bonde, I. Chorkendorff, and J. K. Nørskov, “Computational high-throughput screening of electrocatalytic materials for hydrogen evolution”, *Nat. Mater.* **5**, 909–913 (2006).
- ¹⁸³O. Levy, M. Jahneke, R. V. Chepulskii, G. L. W. Hart, and S. Curtarolo, “Ordered structures in rhenium binary alloys from first-principles calculations”, *J. Am. Chem. Soc.* **133**, 158–163 (2011).
- ¹⁸⁴N. Marzari, D. Vanderbilt, A. De Vita, and M. C. Payne, “Thermal contraction and disordering of the Al(110) surface”, *Phys. Rev. Lett.* **82**, 3296–3299 (1999).
- ¹⁸⁵M. Digne, P. Sautet, P. Raybaud, P. Euzen, and H. Toulhoat, “Hydroxyl groups on γ -alumina surfaces: a dft study”, *J. Catal.* **211**, 1–5 (2002).
- ¹⁸⁶M. Digne, P. Sautet, P. Raybaud, P. Euzen, and H. Toulhoat, “Use of DFT to achieve a rational understanding of acid–basic properties of γ -alumina surfaces”, *J. Catal.* **226**, 54–68 (2004).

- ¹⁸⁷H. Zhai and A. N. Alexandrova, “Local fluxionality of surface-deposited cluster catalysts: the case of Pt₇ on Al₂O₃”, *J. Phys. Chem. Letters* **9**, 1696–1702 (2018).
- ¹⁸⁸B. Zandkarimi and A. N. Alexandrova, “Dynamics of subnanometer Pt clusters can break the scaling relationships in catalysis”, *J. Phys. Chem. Letters* **10**, 460–467 (2019).
- ¹⁸⁹A. V. Ruban, H. L. Skriver, and J. K. Nørskov, “Surface segregation energies in transition-metal alloys”, *Phys. Rev. B* **59**, 15990–16000 (1999).
- ¹⁹⁰V. Bakken and O. Swang, “Atomistic and electronic structure of bimetallic cobalt/rhenium clusters from density functional theory calculations”, *J. Chem. Phys.* **128**, 084712 (2008).
- ¹⁹¹V. G. Grigoryan and M. Springborg, “Temperature and isomeric effects in nanoclusters”, *Phys. Chem. Chem. Phys.* **21**, 5646–5654 (2019).
- ¹⁹²T. R. Henninen, M. Bon, F. Wang, D. Passerone, and R. Erni, “The structure of sub-nm platinum clusters at elevated temperatures”, *Angew. Chem. Int. Ed.* **59**, 839–845 (2020).
- ¹⁹³Z. Łodziana, N.-Y. Topsøe, and J. K. Nørskov, “A negative surface energy for alumina”, *Nat. Mater.* **3**, 289–293 (2004).
- ¹⁹⁴X. Krokidis, P. Raybaud, A.-E. Gobichon, B. Rebours, P. Euzen, and H. Toulhoat, “Theoretical study of the dehydration process of boehmite to γ -alumina”, *J. Phys. Chem. B* **105**, 5121–5130 (2001).
- ¹⁹⁵M. C. Valero, P. Raybaud, and P. Sautet, “Influence of the hydroxylation of γ -Al₂O₃ surfaces on the stability and diffusion of single Pd atoms: a DFT study”, *J. Phys. Chem. B* **110**, 1759–1767 (2006).
- ¹⁹⁶H. P. Pinto, R. M. Nieminen, and S. D. Elliott, “Ab initio study of γ -Al₂O₃ surfaces”, *Phys. Rev. B* **70**, 125402 (2004).
- ¹⁹⁷N. A. Deskins, D. Mei, and M. Dupuis, “Adsorption and diffusion of a single Pt atom on γ -Al₂O₃ surfaces”, *Surf. Sci.* **603**, 2793–2807 (2009).
- ¹⁹⁸I. Levin and D. Brandon, “Metastable alumina polymorphs: crystal structures and transition sequences”, *J. Am. Ceram. Soc.* **81**, 1995–2012 (2005).
- ¹⁹⁹R.-S. Zhou and R. L. Snyder, “Structures and transformation mechanisms of the η , γ and θ transition aluminas”, *Acta Cryst. B* **47**, 617–630 (1991).

- ²⁰⁰L. E. Gálvez-González, A. Posada-Amarillas, and L. O. Paz-Borbón, “Structure, energetics, and thermal behavior of bimetallic Re-Pt clusters”, *J. Phys. Chem. A* **125**, 4294–4305 (2021).
- ²⁰¹D. Mei, J. H. Kwak, J. Hu, S. J. Cho, J. Szanyi, L. F. Allard, and C. H. F. Peden, “Unique role of anchoring penta-coordinated Al³⁺ sites in the sintering of γ -Al₂O₃-supported Pt catalysts”, *J. Phys. Chem. Letters* **1**, 2688–2691 (2010).
- ²⁰²C. Mager-Maury, C. Chizallet, P. Sautet, and P. Raybaud, “Platinum nanoclusters stabilized on γ -alumina by chlorine used as a capping surface ligand: A density functional theory study”, *ACS Catal.* **2**, 1346–1357 (2012).
- ²⁰³I. Z. Koleva, H. A. Aleksandrov, and G. N. Vayssilov, “Decomposition behavior of platinum clusters supported on ceria and γ -alumina in the presence of carbon monoxide”, *Catal. Sci. Technol.* **7**, 734–742 (2017).
- ²⁰⁴H. E. Saucedo, L. E. Gálvez-González, S. Chmiela, L. O. Paz-Borbón, K.-R. Müller, and A. Tkatchenko, *BIGDML: towards exact machine learning force fields for materials*, 2021.
- ²⁰⁵F. Doherty, H. Wang, M. Yang, and B. R. Goldsmith, “Nanocluster and single-atom catalysts for thermocatalytic conversion of CO and CO₂”, *Catal. Sci. Technol.* **10**, 5772–5791 (2020).
- ²⁰⁶A. Wang, J. Li, and T. Zhang, “Heterogeneous single-atom catalysis”, *Nat. Rev. Chem.* **2**, 65–81 (2018).
- ²⁰⁷X.-F. Yang, A. Wang, B. Qiao, J. Li, J. Liu, and T. Zhang, “Single-atom catalysts: a new frontier in heterogeneous catalysis”, *Acc. Chem. Res.* **46**, 1740–1748 (2013).
- ²⁰⁸A. Züttel, “Materials for hydrogen storage”, *Mater. Today* **6**, 24–33 (2003).
- ²⁰⁹H. Kimizuka, S. Ogata, and M. Shiga, “Mechanism of fast lattice diffusion of hydrogen in palladium: interplay of quantum fluctuations and lattice strain”, *Phys. Rev. B* **97**, 014102 (2018).
- ²¹⁰D. E. Jiang and E. A. Carter, “Diffusion of interstitial hydrogen into and through BCC Fe from first principles”, *Phys. Rev. B* **70**, 064102 (2004).
- ²¹¹V. Kapil, M. Rossi, O. Marsalek, R. Petraglia, Y. Litman, T. Spura, B. Cheng, A. Cuzzocrea, R. H. Meißner, D. M. Wilkins, B. A. Helfrecht, P. Juda, S. P. Bienvenue, W. Fang, J. Kessler, I. Poltavsky, S. Vandenbrande, J. Wieme, C. Corminboeuf, T. D. Kühne, D. E. Manolopoulos, T. E. Markland, J. O. Richardson, A. Tkatchenko, G. A. Tribello, V. Van Speybroeck, and M. Ceriotti, “i-PI 2.0: a universal force engine for advanced molecular simulations”, *Comput. Phys. Commun.* **236**, 214–223 (2019).

- ²¹²J. Völkl, G. Wollenweber, K.-H. Klatt, and G. Alefeld, “Notizen: reversed isotope dependence for hydrogen diffusion in palladium”, *Z. Naturforsch. A* **26**, 922–923 (1971).
- ²¹³B. J. Heuser, D. R. Trinkle, N. Jalarvo, J. Serio, E. J. Schiavone, E. Mamontov, and M. Tyagi, “Direct measurement of hydrogen dislocation pipe diffusion in deformed polycrystalline Pd using quasielastic neutron scattering”, *Phys. Rev. Lett.* **113**, 025504 (2014).
- ²¹⁴G. L. Powell and J. R. Kirkpatrick, “Surface conductance and the diffusion of H and D in Pd”, *Phys. Rev. B* **43**, 6968–6976 (1991).
- ²¹⁵X. W. Zhou, F. E. Gabaly, V. Stavila, and M. D. Allendorf, “Molecular dynamics simulations of hydrogen diffusion in aluminum”, *J. Phys. Chem. C* **120**, 7500–7509 (2016).